Accurate Numerical relativity simulations of non-vacuum space-times in two dimensions and applications to critical collapse

Promotion

by

Thorsten Kellermann

Max-Planck-Institut für Gravitationsphysik
Albert-Einstein-Institut

Universität Potsdam

June 2011

Published online at the
Institutional Repository of the University of Potsdam:
URL http://opus.kobv.de/ubp/volltexte/2012/5957/
URN urn:nbn:de:kobv:517-opus-59578
http://nbn-resolving.de/urn:nbn:de:kobv:517-opus-59578

To my wife Saskia and to my children Jannik and Laurin

Contents

Published Works

Part of the contents of this thesis has already appeared in the following papers:

Refereed Journals, Author:

- *An improved formulation of the relativistic hydrodynamics equations in 2D Cartesian coordinates* **Kellermann T.**, Baiotti L., Giacomazzo B. and Rezzolla L., 2008, Classical and Quantum Gravity, **25** 225007.

- *Critical Phenomena in Neutron Stars I: Linearly Unstable Non-rotating Models*, Radice D., Rezzolla L. and **Kellermann T.**, 2010, Classical and Quantum, **27** 235015.

- *Critical Phenomena in Neutron Stars II: Head-on Collisions*, **Kellermann T.**, Rezzolla L. and Radice, D., 2010, Classical and Quantum, **27** 235016.

Part I

Introduction

Chapter 1

Overview

In his book about the *Critique of practical Reason*, [1] Kant wrote *"Two entities prepossess the mind with always new and increasing admiration and awe. Ever more often and permanently the cogitation concerns itself with: The starry Sky above me and the morality in myself"*. For sure, morality is one of the most important questions in our life. There is a sheer endless number of discussions and publications about it. At any time and in every society people questioned about the trueness of their morality. Nevertheless this topic stays outside of the kind of empiric science we want to do.
In this work we are only interested in the fascination about the starry sky. Astronomy may be one of the oldest sciences in the history of mankind. Starting with first settlements, people observed the moon phases and used the results of their observations to create first calendars, which helped to improve the agriculture techniques.
Almost three thousand years later, at the beginning of the fifteenth century, the Mongolian King *Ulugh Beg* built in present-days Usbekistan, the first observatory and the university for astronomy. The history of the following centuries is full of dazzling and tragic characters who built the basis of modern astronomy and astrophysics like Nikolaus Kopernikus, Giordano Bruno, Galileo Galilei, Tycho Brahe, Johannes Kepler, Isaac Newton and many others.
Initiating with Isaac Newton's theory of gravity and his laws of motion and Kepler's laws about planetary motion, astronomers were able to make a huge number of important discoveries and predictions.
With Albert Einstein's general theory of gravitation, scientists were able to explain the phenomena like the deflection of light, the anomalous perihelion advance, or the behaviour of very compact stars.

This Thesis puts its focus on the physics of neutron stars and its description with methods of numerical relativity. In the first step, a new numerical framework the `Whisky2D` code will be developed, which solves the relativistic equations of hydrodynamics in axisymmetry. Therefore we consider an improved formulation of the conserved form of these equations. The second part will use the new code to investigate the critical behaviour of two colliding neutron stars. Considering the analogy to phase transitions in statistical physics, we will investigate the evolution of the entropy of the neutron stars during the whole process. A better understanding of the evolution of thermodynamical quantities, like the entropy in critical process, should provide deeper understanding of thermodynamics in relativity.

Numerical simulations assuming and enforcing axisymmetry are particularly useful to study at higher resolution and smaller computational costs those astrophysical scenarios whose evolution

is expected to possess and preserve such a symmetry. On the other hand, the numerical solution of systems of equations expressed in coordinates adapted to the symmetry has often posed serious difficulties, because of the coordinate singularity present on the symmetry axis. The *"cartoon"* method, proposed by Alcubierre *et al.* [2], allows to exploit the advantages of reduced computational resource requirements, while adopting Cartesian coordinates, which are non-singular everywhere.

The *"cartoon"* method proves to be particularly useful in the numerical evolution of smooth functions, like the metric quantities of the Einstein equations. However, because of the interpolations necessary to impose the axisymmetric conditions on a Cartesian grid, the *"cartoon"* approach could become enough accurate to describe the shocks which generically develop when matter is present. As a consequence, general-relativistic codes employing the *"cartoon"* method have adopted cylindrical coordinates for the evolution of the matter (and magnetic field) variables [3–8]. All the cited works adopt the same formulation for the hydrodynamical equations in cylindrical coordinates. In this Thesis, we propose a slightly different formulation, which has proven to reduce the numerical errors, especially in the vicinity of the symmetry axis.

More specifically, we have written the `Whisky2D` [9] code, which solves the general-relativistic hydrodynamics equations in a flux-conservative form and in cylindrical coordinates. This of course brings in $1/r$ singular terms, where r is the radial cylindrical coordinate, which must be dealt with appropriately. In the above-referenced works, the flux operator is expanded and the $1/r$ terms, not containing derivatives, are moved to the right-hand-side of the equation (the source term), so that the left hand side assumes a form identical to the one of the three-dimensional (3D) Cartesian formulation. We call this the *standard formulation*. Another possibility is not to split the flux operator and to redefine the conserved variables, via a multiplication by r. We call this the *new formulation*. The new equations are solved with the same methods as in the Cartesian case. From a mathematical point of view, one would not expect differences between the two ways of writing the differential operator, but, of course, a difference is present at the numerical level. Our tests show that the new formulation yields results with a global truncation error which is one or more orders of magnitude smaller than those of alternative and commonly used formulations.
The second part of the Thesis uses the new code for investigations of critical phenomena in general relativity. In particular, we consider the head-on-collision of two neutron stars in a region of the parameter space where two final states a new stable neutron star or a black hole, lay close to each other. In 1993, Choptuik [10] considered one-parameter families of solutions, $\mathcal{S}[P]$, of the Einstein-Klein-Gordon equations for a massless scalar field in spherical symmetry, such that for every $P > P^\star$, $\mathcal{S}[P]$ contains a black hole and for every $P < P^\star$, $\mathcal{S}[P]$ is a solution not containing singularities. He studied numerically the behavior of $\mathcal{S}[P]$ as $P \to P^\star$ and found that the critical solution, $\mathcal{S}[P^\star]$, is *universal*, in the sense that it is approached by all nearly-critical solutions regardless of the particular family of initial data considered. He also found that $\mathcal{S}[P]$ exhibit discrete self-similarity and that, for supercritical solutions ($P > P^\star$), the mass of the black hole satisfies $M_{\rm BH} = c|P - P^\star|^\gamma$, with γ being an universal constant, *i.e.* not depending on the particular family of initial data.

After Choptuik's seminal work, similar transitions were discovered for a wide range of systems, including massive scalar fields and ultra-relativistic fluids, see [11] for a recent review. All these phenomena have the common property that, as P approaches $P^\star$, $\mathcal{S}[P]$ approaches a universal solution $\mathcal{S}[P^\star]$ and that all the physical quantities of $\mathcal{S}[P]$ depend only on $|P - P^\star|$. In analogy with critical phase transitions in statistical mechanics, these transitions in gravitational collapse were later

classified as "type-I" critical phenomena, with static or periodic critical solutions and discontinuous transitions in the vicinity of the critical point, or "type-II" critical phenomena, with self-similar critical solutions and continuous transitions in the vicinity of the critical solution [11].

The study of critical phenomena in neutron star (NS) collapse started with the work by [12] on radiation fluids and was later extended to more general ultra-relativistic equations of state (EOS) [13, 14] and ideal-gas EOS [15–17]. In all these studies the collapse was triggered using strong perturbations and a type-II critical phenomena was found. Type-I critical phenomena in the collapse of unstable configurations under very small perturbations was instead studied only very recently [18, 19].

The first study of critical phenomena concerning the head-on collision of NSs was carried out by Jin and Suen in 2007 [20]. In particular, they considered a series of families of equal-mass NSs, modeled with an ideal-gas EOS, boosted towards each other and varied the mass of the stars, their separation, velocity and the polytropic index in the EOS. In this way they could observe a critical phenomenon of type I near the threshold of black-hole formation, with the putative solution being a nonlinearly oscillating star. In a successive work [21], they performed similar simulations but considering the head-on collision of Gaussian distributions of matter. Also in this case they found the appearance of type-I critical behaviour, but also performed a perturbative analysis of the initial distributions of matter and of the merged object. Because of the considerable difference found in the eigenfrequencies in the two cases, they concluded that the critical solution does not represent a system near equilibrium and in particular not a perturbed Tolmann-Oppenheimer-Volkoff (TOV) solution [20].

In this Thesis we study the dynamics of the head-on collision of two equal-mass NSs using a setup which is as similar as possible to the one considered in [20]. While we confirm that the merged object exhibits a type-I critical behaviour, we also argue against the conclusion that the critical solution cannot be described in terms of equilibrium solution. Indeed, we show that, in analogy with what is found in [19], the critical solution is effectively a perturbed unstable solution of the TOV equations. Our analysis also considers fine-structure of the scaling relation of type-I critical phenomena and we show that it exhibits oscillations in a similar way to the one studied in the context of scalar-field critical collapse [22, 23].

The Thesis in organised as follows. In Chapter 2, among the main formulations of the Einstein equations, we will describe those which represent the state-of-the-art in general-relativistic numerical simulation and which are used for the code that provides the evolution of the space-time variables in our simulations. We also repeat the essentials of the *"cartoon"* approach for the evolution of the geometrical variables.
In Chapter 3 we show a brief summary of the physical origin of the equations of hydrodynamics, followed by a review of the flux-conservative formulation of relativistic hydrodynamics. We write down the relativistic flux-conservative hydrodynamics equations for axisymmetric formulations and we illustrate the two possible ways to write the singular term. Chapter 4 presents the state-of-the-art numerical schemes of the evolution of hydrodynamical quantities, i.e. the *high-resolution shock capturing* methods. In Chapter 5, we show several tests that compare the two formulations. We begin with the conservation of rest mass and angular momentum in the Cowling approximation -keeping the space-time fixed- and in full space-time evolution. Then the eigenfrequencies of uniformly rotating neutron star models are compared with the results of a perturbative code. The last test examines the differences between the two formulations with respect to an analytic solution

of an extreme shock case, which mimics the reflection of a cold and very fast gas at the symmetry axis.

Chapter 6 gives an overview about the main physical and mathematical topics of critical phenomena. In Chapter 7 we consider the evolution in full general relativity of a family of linearly *unstable* isolated spherical neutron stars under the effects of very small, perturbations as induced by the truncation error. Using a simple ideal-fluid equation of state we find that this system exhibits a type-I critical behaviour, thus confirming the conclusions reached by Liebling et al. [18] for rotating magnetized stars. Exploiting the relative simplicity of our system, we are able carry out a more in-depth study providing solid evidences of the criticality of this phenomenon and also to give a simple interpretation of the putative critical solution as a spherical solution with the unstable mode being the fundamental F-mode. Hence for any choice of the polytropic constant, the critical solution will distinguish the set of subcritical models migrating to the stable branch of the models of equilibrium from the set of subcritical models collapsing to a black hole. Finally, we study how the dynamics changes when the numerically perturbation is replaced by a finite-size, resolution independent velocity perturbation and show that in such cases a nearly-critical solution can be changed into either a sub or supercritical. The work reported here also lays the basis for the analysis carried in a companion paper, where the critical behaviour in the head-on collision of two neutron stars is instead considered [24].

Chapter 8 is devoted the head-on collision of equal-mass neutron stars boosted towards each other and we study the behavior of such systems near the threshold of black-hole formation. In particular, we confirm the previous findings by [20] that a type-I critical phenomenon can be observed by fine-tuning the initial mass of the two neutron stars. At the same time, we argue against the interpretation that the critical solution is not a perturbed spherical star and show instead that the metastable star corresponds to a (perturbed) equilibrium solution on the unstable branch of the equilibrium configurations. As a result, the head-on collision of two neutron stars near the critical threshold can be seen as a transition in the space of configurations from an initial stable solution over to a critical metastable one which can either migrate to a stable solution or collapse to a black hole. The critical exponent for this process shows a fine structure which was already observed in the case of the critical collapse of scalar fields but never before for perfect fluids.

We have used a space-like signature $(-,+,+,+)$, with Greek indices running from 0 to 3, Latin indices from 1 to 3 and the standard convention for the summation over repeated indices. Unless explicitly stated, all the quantities are expressed in the system of dimensionless units in which $c = G = M_\odot = 1$.

Part II

A brief introduction to numerical relativity

Chapter 2

Einstein equations in vacuum

2.1 Introduction

We start with a discussion about basics of numerical relativity in the absence of matter. The extension to non-vacuum space-times will be presented in Chapter 3. The Einstein equations describing the highly non-linear relation between the metric and the energy-matter fields are

$$G_{\mu\nu} \equiv R_{\mu\nu} - \frac{1}{2} g_{\mu\nu} R = 8\pi T_{\mu\nu}, \tag{2.1}$$

where $T_{\mu\nu}$ is the *stress-energy tensor* and $G_{\mu\nu}$ is the *Einstein tensor*. Contracting the *Riemann Tensor*

$$R^{\sigma}_{\mu\rho\nu} \equiv \partial_\rho \Gamma^{\sigma}_{\ \mu\nu} - \partial_\nu \Gamma^{\sigma}_{\ \mu\rho} + \Gamma^{\sigma}_{\ \tau\rho}\Gamma^{\tau}_{\ \mu\nu} - \Gamma^{\sigma}_{\ \tau\nu}\Gamma^{\tau}_{\ \mu\rho}, \tag{2.2}$$

leads to the *Ricci Tensor* $R_{\mu\nu} \equiv R^{\rho}_{\mu\rho\nu}$. A further contraction yields to the *Ricci scalar* $R \equiv R^{\rho}_{\ \rho}$. The *Christoffel symbols*

$$\Gamma^{\sigma}_{\mu\rho} \equiv \frac{1}{2} g^{\sigma\tau} (\partial_\mu g_{\rho\tau} + \partial_\rho g_{\mu\tau} - \partial_\tau g_{\mu\rho}), \tag{2.3}$$

are expressed in terms of the metric $g_{\mu\nu}$. All these objects are 4-dimensional, in that they are defined on the 4-dimensional space-time manifold $\mathcal{M}$. Despite the covariant nature of the equations, the ability to perform long-term numerical simulations of self-gravitating systems in general relativity strongly depends on the formulation adopted for the Einstein equations (2.1) and forces the choice of appropriate coordinate charts in order to have stable accurate simulations. In the course of time, the "3+1" formulation of space-time, introduced by Arnowitt, Deser and Misner (*ADM*) [25], became the standard approach in numerical relativity.
In next section we will give an overview about the most important properties of the *ADM* formalism. In Chapter 2.3 we will show an advancement of the *ADM* method, which enables longer evolutions and is the one implemented in the code we have developed.

2.2 The Arnowitt Deser Misner "3+1" formalism

Following the idea of the *ADM* formalism, the space-time manifold $\mathcal{M}$ is assumed to be globally hyperbolic and this allows for the foliation by 3-dimensional space-like hyper-surfaces Σ_t, parametrised by the parameter $t \in \mathcal{R} : \mathcal{M} = \mathcal{R} \times \Sigma_t$. The future pointing 4-vector $\boldsymbol{n}$ is orthogonal to the hyper-surface Σ_t and proportional to the gradient of *t:* $\boldsymbol{n} = -\alpha \nabla t$, where α follows the normalisation

$\mathbf{n}\cdot\mathbf{n} = -1$. Introducing a coordinate basis $\{\mathbf{e}_{(\mu)}\} = \{\mathbf{e}_{(0)}, e_{(i)}\}$ of 4-vectors and choosing the normalisation of the time-like component of the 4-vector $\mathbf{e}_{(0)}$ to be $\mathbf{e}_{(0)}\cdot\nabla t = 1$, with the other three basis 4-vectors to be space-like components $\mathbf{e}_{(i)}$ (*i.e.* tangent to the hyper-surface $n\cdot\mathbf{e}_{(i)} = 0\ \ \forall i$), the decomposition of $\mathbf{n}$ into the basis $\{\mathbf{e}_{(\mu)}\}$ is

$$\mathbf{n} = \frac{\mathbf{e}_{(0)}}{\alpha} + \frac{\beta}{\alpha}. \tag{2.4}$$

The *shift* vector $\beta = \beta^i\mathbf{e}_{(i)}$ is exclusively spatial. It describes how the spatial coordinates shift when moving from a hyper-surface Σ_t to another $\Sigma_{t'}$. To close the system the *lapse* function α is needed, which describes the progress of time along the time-like unit-vector $\mathbf{n}$ normal to the space-like slice Σ_t. The spatial part of the 4-metric $\gamma_{\mu\nu} \equiv g_{\mu\nu} + n_\mu n_\nu$ is defined, so that γ is a projector orthogonal to $\mathbf{n}$ (*i.e.* $\gamma\cdot\mathbf{n} = 0$) and γ_{ij} is the 3-metric of the hyper-surface. It follows the line element of the 3+1 splitting

$$ds^2 = -(\alpha^2 - \beta^i\beta_i)dt^2 + 2\beta_i dx^i dt + \gamma_{ij}dx^i dx^j. \tag{2.5}$$

Eulerian observers, resting in the slice Σ_t, *i.e.* those having the 4-velocity $\mathbf{u}$ parallel to $\mathbf{n}$, measure the following 3-velocity of the fluid:

$$v^i = \frac{\gamma\cdot\mathbf{u}}{-\mathbf{n}\cdot\mathbf{u}} = \frac{\gamma^i_\delta u^\delta}{\alpha u^0} = \frac{g^i_\delta u^\delta + n^i n_\delta u^\delta}{\alpha u^0} = \frac{u^i}{\alpha u^0} - n^i = \frac{u^i}{W} + \frac{\beta^i}{\alpha}, \tag{2.6}$$

where we have used (2.4) and where $-\mathbf{n}\cdot\mathbf{u} = \alpha\mathbf{u}^0 = W$ is the Lorentz factor. In the upcoming Chapters we will use the covariant expressions of (2.6)

$$v_i = \frac{\gamma^\rho_i u_\rho}{-\mathbf{n}\cdot\mathbf{u}} = \frac{(\delta^\rho_i + n^\rho n_i)u_\rho}{W} = \frac{u_i}{W} \tag{2.7}$$

and

$$\begin{aligned} u_0 = u^\mu g_{\mu 0} = u^0 g_{00} + u^i g_{i0} = u^0(-\alpha^2 + \beta_i\beta^i) + u^i\beta_i = \\ -W\left(\alpha - \frac{\beta^2}{\alpha}\right) + W\left(v^i - \frac{\beta^i}{\alpha}\right)\beta_i = W(v^i\beta_i - \alpha). \end{aligned} \tag{2.8}$$

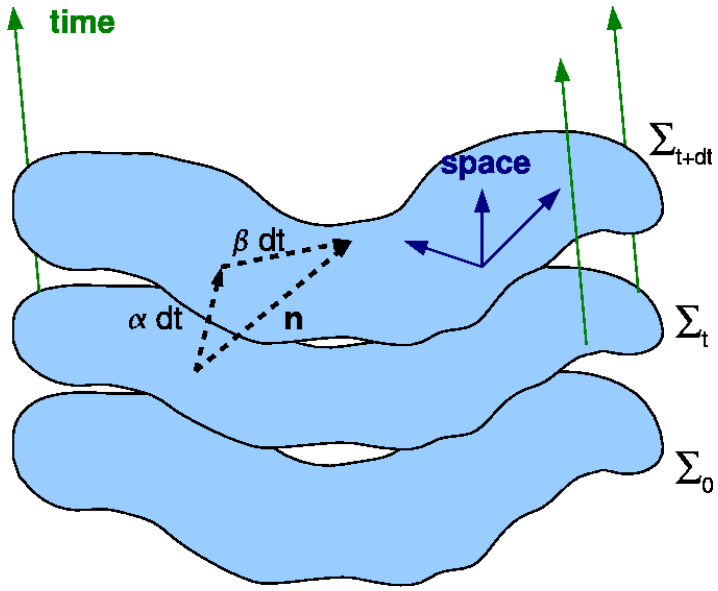

Figure 2.1: shows the foliation of the 3+1 decomposition. The hyper-surfaces Σ_t are spatial hyperbolic Cauchy surfaces, which arise of the *ADM* formalism. Σ_0 is the hyper-surface at $t = 0$ and contains all information about the initial data.

The success of the *ADM* approach is the reformulation of the Einstein equations in a set of first-order-in-time second-order-in-space quasi-linear system [26] and a set of elliptic equation (the *constraint equations*). The time evolution is applied to the dependent variables of the 3-metric γ_{ij} and the extrinsic curvature

$$K_{ij} \equiv -\gamma_i^k \gamma_j^l \nabla_k n_l, \tag{2.9}$$

where ∇_i denotes the covariant derivative with respect to the 3-metric γ_{ij}. By construction the extrinsic curvature is symmetric and only spatial. The extrinsic curvature describes the embedding of the 3-dimensional space-like hyper-surface Σ_t in the 4-dimensional manifold $\mathcal{M}$. At first we consider the first order evolution equations given by

$$\mathcal{D}_t \gamma_{ij} = -2\alpha K_{ij}, \tag{2.10}$$

$$\mathcal{D}_t K_{ij} = -\nabla_i \nabla_j \alpha + \alpha\big[R_{ij} + K K_{ij} - 2K_{im}K_j^m - 8\pi\big(S_{ij} - \frac{1}{2}\gamma_{ij} S\big) - 4\pi\rho\gamma_{ij}\big]. \tag{2.11}$$

$\mathcal{D}_t \equiv \partial_t - \mathcal{L}_\beta$, $\mathcal{L}_\beta$ defines the the Lie derivative [1] with respect to the vector β, R_{ij} is the Ricci tensor of the 3-metric, $K \equiv \gamma^{ij} K_{ij}$ is the trace of the extrinsic curvature, $\rho \equiv n_\mu n_\nu T^{\mu\nu}$ is the total energy density as measured by a normal observer. The projection of the stress-energy tensor on the normal to the spatial hyper-surface $S_{ij} \equiv \gamma_{i\mu}\gamma_{j\nu} T^{\mu\nu}$ and $S \equiv \gamma^{ij} S_{ij}$ the rejuvenation of S_{ij} (a detailed discussion can be found in [27]). Equation (2.10) provides an interpretation of the extrinsic curvature, as the rate of change of the spatial metric. Similarly (2.11) provides an interpretation of the time derivative of the extrinsic curvature of an acceleration of the metric.

[1] For an arbitrary tensor $T^{s_1,\ldots,s_u}_{t_1,\ldots,t_w}$ and an arbitrary vector **v** the Lie derivative is defined as

$$\mathcal{L}_v T^{s_1,\ldots,s_u}_{t_1,\ldots,t_w} \equiv v^r \nabla_r T^{s_1,\ldots,s_u}_{t_1,\ldots,t_w} - \sum_{n=1}^{u} T^{s_1,\ldots,r,\ldots,s_u}_{t_1,\ldots,t_w} \nabla_r v^{s_n} + \sum_{n=1}^{w} T^{s_1,\ldots,s_u}_{t_1,\ldots,r,\ldots,t_w} \nabla_{t_n} v^r.$$

Due to the symmetric character of the Einstein tensor we expect ten partial differential equations. Equations (2.10) and (2.11) cover six. The missing four equations are the elliptic or constraint equations of the *ADM* formalism. Such equations are called constraint equations because they have no time dependence and they have to be satisfied on each space-like hyper-surface Σ_t. Starting with the Hamiltonian constraint equation, which can be seen like an energy conservation equation of the whole space-time

$$H \equiv R + K^2 - K_{ij}K^{ij} - 16\pi\rho \; = \; 0, \tag{2.12}$$

where R is the Ricci scalar of the 3-metric, distinguish it form R^{μ}_{μ}. The last three equations are the momentum constraint equations,

$$M^i \equiv \nabla_j K^{ij} - \gamma^{ij}\nabla_j K - 8\pi S^i \; = \; 0. \tag{2.13}$$

where $S^i \equiv -\gamma^{i\mu}n^{\nu}T_{\mu\nu}$ describes the momentum density, as seen by an observer moving orthogonally to the space-like hyper-surfaces.
The system of equations (2.10)-(2.13) is not closed; there are several degrees of freedom in relation to the coordinate system. We are free to set a specification for the gauge conditions. These are usually imposed as equations on the lapse and the shift. The number of possible gauge condition is infinite, but all of them are gauge invariant and lead to the same physical results. Nevertheless only a few gauge conditions are able to handle the non-invariant quantities in the right way to enable a stable numerical evolution. The choice of good gauge conditions is fundamental for numerical relativity. There are numerous well-tested gauge conditions. Some of them will be discusses in section 2.3.2.
Finally we show the expression of the total mass and the total angular momentum as measured at infinity in an asymptotically-flat space-time. The integral to calculate the mass can be described as a surface integral. But it is numerical more correct to use equivalent expression in terms of of a volume integral.

$$M_{ADM} \; \equiv \; \frac{1}{16\pi} \int\limits_{r=\infty} \sqrt{\gamma}\gamma^{im}\gamma^{jl}(\gamma_{ml,j} - \gamma_{jl,m}) d^2\mathcal{S}_i, \tag{2.14}$$

$$M_{ADM} \; \equiv \; \frac{1}{16\pi} \int\limits_{r=\infty} [\alpha\sqrt{\gamma}\gamma^{im}\gamma^{jl}(\gamma_{ml,j} - \gamma_{jl,m})]_{,l} d^3x_i, \tag{2.15}$$

$$(J_{ADM})_i \; \equiv \; \frac{1}{8\pi}\epsilon_{ij}{}^{k} \int\limits_{r=\infty} x^j K^m_k \; d^2\mathcal{S}_m, \tag{2.16}$$

where $\mathcal{S}$ is a closed surface in an asymptotically-flat region and ϵ^k_{ij} is the flat Levi-Civita tensor.

2.3 The conformal transverse traceless formulation

For many years most numerical codes used the *ADM* formalism to solve Einstein equations. However many different attempts to improve boundary or gauge condition, to achieve long-term stability, failed all. The *ADM* formalism and its numerical application has in fact two fundamental problems. In a mathematical sense, the type of the set of PDEs of the *ADM* system is *weakly-hyperbolic*. A direct consequence of such systems is, that the solution is not necessarily unique. It means any possible solution can split up in two or more branches, which brings a serious problem for any numerical evolution scheme. If there are two or more solutions, whose trajectories stay very close together, the numerical solution could jump between the solutions. The first schemes were based on the unconstrained solution (*i.e.* the solution of the time-evolution equations disregarding the constraint equations, except for

checking the accuracy of the result) of the 3+1 *ADM* formalism of the field equations, which though, despite long-term investigations [28–30] has gradually been shown to lack the stability properties necessary for long-term numerical solutions.
Including at some point the solution of constraint equations on each hyper-surface [31, 32] was one of the most successful efforts to perform long-term stability, which has been invested in the last recent years. In 1987 Nakamura, Oohara and Kojima suggested a conformal traceless reformulation of the *ADM* system [33]. A number of authors [4, 34–40] gradually showed the robustness of the new formulations by robust simulations of sophisticated problems like isolated binary systems.
In the next section we discuss the most popular branch of the family of conformal traceless reformulation, the *NOK*, which formalism was suggested by [34, 35]. In the literature it is usually called *BBSNOK* formalism.

2.3.1 Evolution of the field equations in the BSSNOK formalism

In this section we show the equations of the conformal traceless reformulation of the *ADM* equations. We outline the BSSNOK formalism, which is a combination of NOK equations and the improvements introduced in [34,35]. The numerical scheme is already implemented in the structure of the CCATIE code, a detailed description of the code structure can be found in [41]. The gauge conditions for the lapse and the shift function are discussed in section 2.3.2.
In order to obtain the conformal traceless reformulation of the *ADM* equations (2.10)-(2.13) we consider the conformal decomposition of the 3-metric and the trace-free part of the extrinsic curvature. Taking the work of [42] as basis we get the conformal 3-metric $\tilde{\gamma}_{ij}$:

$$\tilde{\gamma}_{ij} \equiv e^{-4\phi}\gamma_{ij} \tag{2.17}$$

with the conformal factor chosen to be

$$e^{4\phi} = \gamma^{1/3} \equiv det(\gamma_{ij})^{1/3}. \tag{2.18}$$

In this way the determinant of $\tilde{\gamma}_{ij}$ in unity. The trace free part of the extrinsic curvature K_{ij} is defined as followed

$$A_{ij} \equiv K_{ij} - \frac{1}{3}\gamma_{ij}K, \tag{2.19}$$

and its conformal decomposition

$$\tilde{A}_{ij} \equiv e^{-4\phi}A_{ij}. \tag{2.20}$$

The evolution equations of the conformal 3-metric $\tilde{\gamma}_{ij}$ and the related conformal factor ϕ are then written as

$$\mathcal{D}_t\tilde{\gamma}_{ij} = -2\alpha\tilde{A}_{ij}, \tag{2.21}$$

$$\mathcal{D}_t\phi = -\frac{1}{6}\alpha K. \tag{2.22}$$

It follows also the evolution equation of the extrinsic curvature K

$$\mathcal{D}_tK = -\gamma^{ij}\nabla_i\nabla_j\alpha + \alpha\big[\tilde{A}_{ij}\tilde{A}^{ij} + \frac{1}{3}K^2 + \frac{1}{2}(\rho + S)\big]. \tag{2.23}$$

The Ricci scalar is eliminated by the usage of the Hamiltonian constraint. Using a trivial manipulation of equation (2.11) a formulation of the evolution equation of the trace-free extrinsic curvature can be obtained:

$$\mathcal{D}_t\tilde{A}_{ij} \;=\; e^{-4\phi}[\nabla_i\nabla_j\alpha + \alpha(R_{ij} - S_{ij})]^{TF} + \alpha(K\tilde{A}_{ij} - 2\tilde{A}_{ij}\tilde{A}^j_j), \tag{2.24}$$

where $[M_{ij}]^{TF}$ describes the trace-free part of the 3-dimensional tensor second-rank M_{ij}, *i.e.*, $[M_{ij}]^{TF} \equiv M_{ij} - \gamma_{ij}M^k_k/3$. Note that the formulation of (2.24) is not unique. The different ways to write equation (2.24) are listed in [34, 35], especially there are several ways to write the Ricci tensor. A conformal decomposition of the Ricci tensor

$$R_{ij} \;=\; \tilde{R}_{ij} + R^{\phi}_{ij}, \tag{2.25}$$

is the most convenient expression to do numerical simulations. The conformal-factor part R^{ϕ}_{ij} is directly calculated by the spatial derivatives of ϕ:

$$R^{\phi}_{ij} \;=\; -2\tilde{\nabla}_i\tilde{\nabla}_j\phi - 2\tilde{\gamma}_{ij}\tilde{\nabla}^l\tilde{\nabla}_l\phi + 4\tilde{\nabla}_i\phi\tilde{\nabla}_j\phi - 4\tilde{\gamma}_{ij}\tilde{\nabla}^l\phi\tilde{\nabla}_l\phi \tag{2.26}$$

and the conformal part $\tilde{R}_{ij}$ is computed from the 3-metric $\tilde{\gamma}_{ij}$ in the usual way. The conformal connection function of Baumgarte [35]

$$\tilde{\Gamma}^i \;\equiv\; \tilde{\gamma}^{jk}\tilde{\Gamma}^i_{jk} \;=\; -\partial_j\tilde{\gamma}^{ij} \tag{2.27}$$

is a convenient way to simplify the notation, whereby this equation retains the unity of the conformal 3-metric $\tilde{\gamma}$, that is may be not true in numerical simulations. Now the Ricci tensor can be written as

$$\tilde{R}_{ij} \;=\; -\frac{1}{2}\tilde{\gamma}^{lm}\partial_l\partial_m\tilde{\gamma}_{ij} + \tilde{\gamma}_{k(i}\partial_{j)}\tilde{\Gamma}^k + \tilde{\Gamma}^k\tilde{\Gamma}_{(ij)K} + \tilde{\gamma}^{lm}\big(2\tilde{\Gamma}^k_{l(i}\tilde{\Gamma}_{j)km} + \tilde{\Gamma}^k_{im}\tilde{\Gamma}_{klj}\big). \tag{2.28}$$

Also in this case there are different ways to calculate the terms, which are included in the conformal-connection function $\tilde{\Gamma}^i$. The usual way to calculate the Christoffel symbols, like in the standard *ADM* formulation however leads to non elliptic derivatives of the 3-metric. Alcubierre *et al.* [42] could show that a handling of $\tilde{\Gamma}^i$ in independent variables retains the elliptic character of the Ricci tensor and gives the system a more hyperbolic character. However, it costs three extra variables. The numerical advantages will be discussed below.
Using the conformal Christoffel symbols $\tilde{\Gamma}^i$ written in independent variables, the evolution equation can be derived straightforward by,

$$\partial_t\tilde{\Gamma}^i \;=\; -\partial_j\big(2\alpha\tilde{A}^{ij} - 2\tilde{\gamma}^{(j}\partial_m\beta^{i)} + \frac{2}{3}\tilde{\gamma}^{ij}\partial_l\beta^l + \beta^l\partial_l\tilde{\gamma}^{ij}\big). \tag{2.29}$$

Unfortunately, equation (2.29) leads to instabilities, as shown in [35]. Again there are different ways to write the evolution equation of $\tilde{\Gamma}_{ij}$. Alcubierre et al. [42] could eliminate the divergences in $\tilde{A}^{ij}$ by using the momentum constraint equation (2.13)

$$\begin{aligned}\partial_t\tilde{\Gamma}^i \;=\; &-2\tilde{A}^{ij}\partial_j\alpha + 2\alpha\big(\tilde{\Gamma}^i_{jk}\tilde{A}^{jk} - \frac{2}{3}\tilde{\gamma}^{ij}\partial_j K - \tilde{\gamma}^{ij}S_j + 6\tilde{A}^{ij}\partial_j\phi\big)\\ &-\partial_j\big(\beta^l\partial_l\tilde{\gamma}^{ij} - 2\tilde{\gamma}^{m(j}\partial_m\beta^{i)} + \frac{2}{3}\tilde{\gamma}^{ij}\partial_l\beta^l\big).\end{aligned} \tag{2.30}$$

The evolution equations of the conformal 3-metric $\tilde{\gamma}$ (2.21), the components of the conformal traceless extrinsic curvature $\tilde{A}_{ij}$ (2.24) and the reformulated evolution equation of the conformal-connection

function $\tilde{\Gamma}^i$ (2.30) build together with the conformal factor ϕ (2.22) and the trace *K* of the extrinsic curvature (2.23) the set of BSSNOK equations.
The final system to evolve the 17 variables $\left\{\phi, K, \tilde{\gamma}_{ij}, \tilde{A}_{ij}, \tilde{\Gamma}^i\right\}$ with a set of first-order-in-time an second-order-in-space PDEs shows a stability of long-term numerical simulation. In fact, it could be shown that the equations are at least equivalent to a hyperbolic system, but they are not strongly hyperbolic in any case [43–45].
To conclude this section we give the expressions of the gravitational mass and the total angular momentum in variables of conformal flat formulation. The expressions are valued in an asymptotically-flat region of the space-time. By Gauss law the primarily surface integrals are transformed to volume integrals, because it was shown by [46], that the numerical calculation of the volume integral formulation of the quantities achieve more precisely results, than the surface integral. With respect to the context of this work the integrals are written in cylindrical coordinates and axisymmetry:

$$M = 2\pi \int_V \left[e^{5\phi}\left(\rho + \frac{1}{16}\bar{A}_{ij}\bar{A}^{ij} - \frac{1}{24}K^2\right) - \frac{1}{16}\tilde{\Gamma}^{ijk}\tilde{\Gamma}_{jik} + \frac{1-e^{\phi}}{16\pi}\tilde{R}\right] r\, dr\, dz\,, \tag{2.31}$$

$$J_i = 2\pi\, \epsilon_{ij}^{k} \int_V \left(\frac{1}{8\pi}\tilde{A}_k^j + x^j S_k + \frac{1}{12\pi}x^j K_{,k} - \frac{1}{16\pi}x^j \tilde{\gamma}_{,k}^{lm}\tilde{A}_{lm}\right) e^{6\Phi} r\, dr\, dz\,. \tag{2.32}$$

2.3.2 Gauge conditions

Gauge conditions describe the slicing of the space-time of the 3+1 decomposition and the distribution of spatial coordinates on each hypersurface. Generally there is an infinite number of possibilities to describe the structure of a spatial manifold and its modification between the time-steps. However, numerical evolution schemes can not use any arbitrary choice of the lapse and the shift function. The final form depends on the problem which should be solved. E.g. it is extremely difficult to handle spatial slices including singularities and therefore a "singularity avoiding slicing " condition was designed
An overview about possible families of gauge conditions, which have been tested and used in the CCATIE code is presented by [42, 47]:

- *Geodesic slicing* is the most simple choice of a gauge condition. The lapse function is set to a constant value, usually $\alpha = 1$ and $\beta = 0$. From time step to time step the slices retain their shape progress in time is constant. Such gauge conditions are used to calculate initial data for equilibrium star models. [48, 49].

- *Hyperbolic slicing* describes a family of gauge conditions which are "singularity avoiding slicing". This method avoids that a spatial slice ever touches a singularity. In order to realise this requirement the shape of the slices changes from time step to time step. Close to the singularity the progress in time goes to zero. Outside the black hole it follows a constant progress in time (figure 2.2).
  All simulations in this thesis are done with the "hyperbolic K-driver slicing" method:

$$\partial_t \alpha - \beta^i \partial_i \alpha = -f(\alpha)\alpha^2(K - K_0), \tag{2.33}$$

  with $f(\alpha) > 0$ and $K_0 \equiv K(t = 0)$ is the initial value of the trace of the extrinsic curvature. Normally there are two choices of $f(\alpha)$ which are used for simulation runs. The harmonic

slicing condition $f = 1$, which is not used here and the generalized "1+log" slicing [2] condition [51] $f = q/a$, where q is an arbitrary integer. All of the results discussed in this work are calculated with the "1+log" slicing condition, where $f(\alpha) = 2/\alpha$ and (2.33) becomes.

$$\partial_t \alpha - \beta^i \partial_i \alpha = -2\alpha(K - K_0). \tag{2.34}$$

Note that the "1+log" gauge condition is could also lead to problems, like shock-waves of the lapse function during formation of a singularity, or fast growing field variables triggered by non-linear terms of the gauge condition [52, 53]. None of these have been encountered in the simulations performed here.

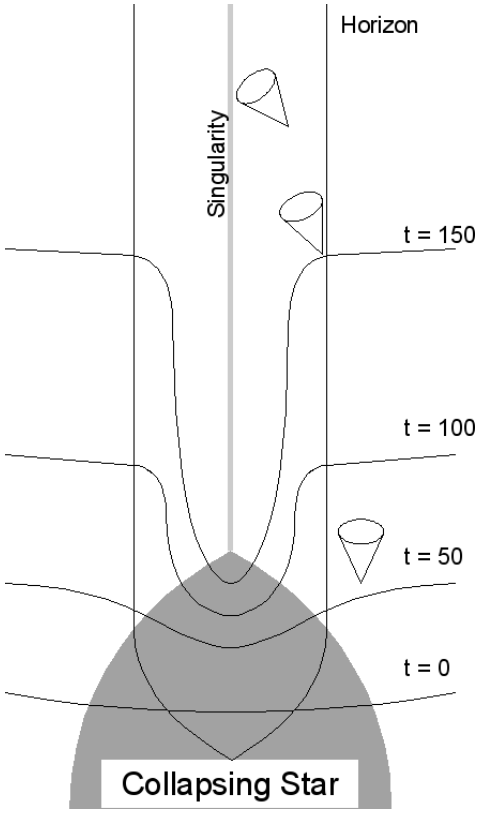

Figure 2.2: demonstrates the evolution of the slices close to a singularity, if a singularity avoiding gauge condition is chosen. The slices approach closer and closer from time to time to the singularity, but they slice will never touch it. Figure taken from [54]

.

Furthermore the determination of the shift condition is related to astrophysical problems. In many cases it is almost impossible to keep a fixed structure of the numerical grid, because the rotation of compact objects or the collapse of stars lead to strong distortions of the grid (e.g. [55]). To put the shift condition to $\beta^i = 0$ would be the easiest, but also worst choice, because this gauge condition is

[2] The origin of the name "1+log" is related to the integrated form of the slicing condition given by $\alpha = h(x^i) + \ln(\gamma)$, where $h(x^i)$ is a time-dependent function and γ is the determinant of the 3-metric γ_{ij} [50]

not able to absorb grid deformations. In many cases ”Gamma-driver“ shift conditions are used, which are proposed in [47] and [56].

- The *Minimal distortion condition* is a geometrically motivated choice of the shift function. The whole formalism [57] leads to a set of coupled elliptic equations, which are numerically expensive to solve.

- The *Gamma-freezing condition*
$$\partial_t \tilde{\Gamma}^k = 0 \tag{2.35}$$
is similar to the minimal distortion condition. It leads also in a set of elliptic equations and it is not able to handle singularities. These two method show a main distinction, while the minimal distortion condition is covariant, the Gamma-freezing method condition is not.

- The *Hyperbolic Gamma-driver-condition* method, which is used for all the simulations in this work.
$$\partial_t \beta^i - \beta^j \partial_j \beta^i = \frac{3}{4} \alpha B^i \,, \tag{2.36}$$
$$\partial_t B^i - \beta^j \partial_j B^i = \partial_t \tilde{\Gamma}^i - \beta^j \partial_j \tilde{\Gamma}^i - \eta B^i \,, \tag{2.37}$$
where $\eta = 0.75$ is a parameter which acts as a damping coefficient [58] to avoid strong oscillations in the shift.

2.3.3 Boundary conditions

GR is a *non-local* theory, whose physical quantities are defined in infinity. However in numerical simulations, only a finite region of the spatial hyper-surface is covered by the computational domain. Therefore the computational code must employ boundary conditions (BCs).
One possibility is a compactification done by coordinate transformation, to realise infinity on a finite numerical grid [59]. This method is not used in this work, but may be interesting for further investigation.
Here, appropriate BCs are applied to the edges of the numerical domain. It is the duty of BCs to continue the values on the numerical grid over its edge as though the grid would be unbounded. BCs are applied to the field variables as well as to the hydrodynamics variables, even if the outer boundaries are usually placed in regions without matter and so their evolution is often trivial. Normally the same boundary conditions are applied to all variables.
While it is comparatively simpler to handle matter when it crosses the outer boundary condition, it is much more difficult to develop BCs that would allow the space-time variables (e.g. GWs) to leave the grid without reflecting.
Moreover not all of the evolved quantities behave like waves.
At the best, BCs can be constructed, that allows wave-like solution to leave the grid at which no large reflections at the boundary should be introduces [60]. The boundary conditions actually implemented in the `CCATIE` code are the following.

- *Static boundary condition (Dirichlet)*, are the easiest BCs, which can be implemented. The evolved variables at the boundary are simply not updated and retain their initial values. However, these conditions are improper to simulate the propagation of waves, because everything is reflected back.

- *Zero-order extrapolation or "flat" boundary conditions (Neumann):* Here the values at the boundary are replaced after every time-step. The values of the last point of the grid are simply copied to the next point of the boundary (along the normal direction to the boundary). Therefore this condition is more dynamical than static BCs and supports the propagation of waves over the boundary. Nevertheless, it is not free from artificial reflections.

- *Radiative boundary conditions (Sommerfeld)* In this case we assume that the dynamical variables behave like a constant plus an outgoing radial wave at the boundaries, that is

$$f(x^i, t) = f_0 + u(r - t)/r, \tag{2.38}$$

where $r = \sqrt{x^2 + y^2 + z^2}$ and where f_0 is set to one of the diagonal components of the metric and zero for everything else. To use radiative BCs it is necessary that the boundaries are inside the wave zone, where the gravitational wave front has a spherical shape. Experience with Sommerfeld BCs in application to gravitational wave leaving the grid cleanly are discussed in [34, 35]. In practice, it is easier to implement a differential form of the radiative boundary condition than to use (2.38) directly. If we consider a boundary, that corresponds to a coordinate plane $x_i =$ constant, the condition (2.39) implies

$$\frac{x_i}{r}\partial_t f + \partial_i f + \frac{x_i}{r^2}(f - f_0) = 0. \tag{2.39}$$

Simulations presented in this work have been performed using the differential Sommerfeld BCs (2.39).

2.3.4 The "`Cartoon`" method

Here we work out the numerical solutions of the relativistic equations of hydrodynamics in axisymmetry. The `CCATIE` code is designed for calculations on a 3D Cartesian grid. In order to merge, both coordinate systems we selected a slice on the cylindrical grid at $\phi = 0$. This section coincides with one slice on the Cartesian grid, which is chosen at $y = 0$, (see figure 2.3). However, variables of space are still evolved in Cartesian coordinates. There are two possible ways to merge the equations of relativistic hydrodynamics and the equations of space-time evolution. In the first one, the space-time evolution code could be rewritten in cylindrical coordinates and asymmetry. While this is possible, it also requires the definition of suitably defined coordinates and the application of regularisation techniques [61] at the cylindrical axis. Both choices are essential for a stable evolution. On the other side, a second method, the `Cartoon` method, can be used to transform variables of the cylindrical grid to variables of the Cartesian grid (see figure 2.4).

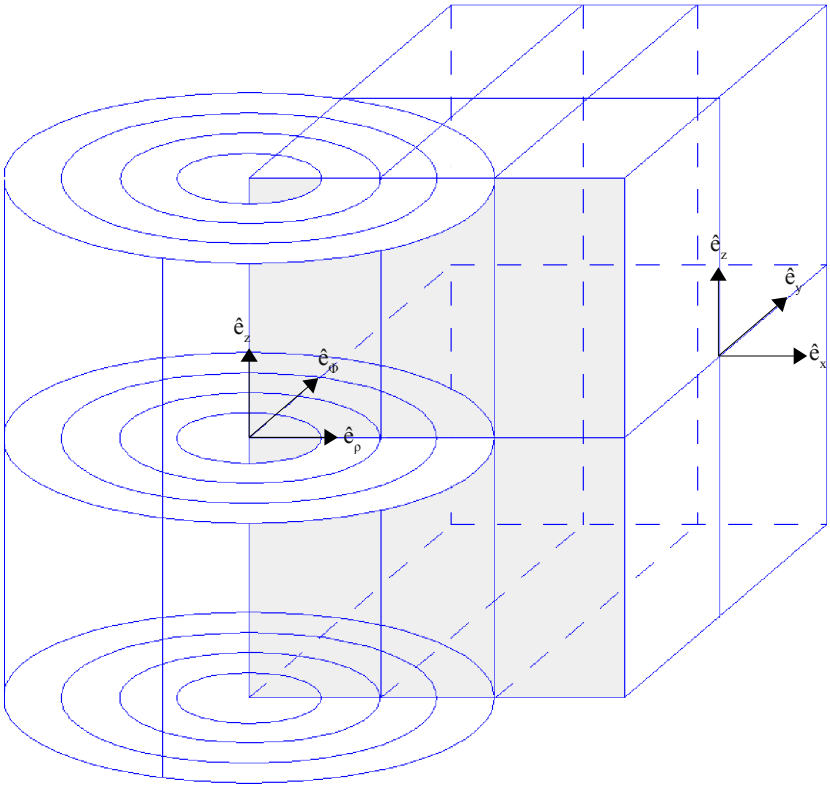

Figure 2.3: shows the overlap of a cylindrical coordinate system with a Cartesian coordinate system. The cross-section of both coordinate systems is the slice, where the Whisky2D works.

The chief advantages of this approach, which is usually referred to as the Cartoon method [2], are the absence of the need of regularization conditions and the easiness of implementation, through a simple dimensional reduction from fully 3D codes in Cartesian coordinates. However, these advantages are counterbalanced by at least two disadvantages. The first one is that the method still essentially requires the use of a 3D domain covered with Cartesian coordinates, although one of the three dimensions, namely the y-direction, has a very small extent. The second one is that, in order to compute the second-order spatial derivatives in the y-direction appearing in the Einstein equations, a number of high-order interpolations onto the x-axis are necessary (see discussion below) and these can amount to a significant portion of the time spent for each evolution to the new time-level. In practice, the spatial derivatives in the y-direction are computed exploiting the fact that all quantities are constant on cylinders and thus the value of a variable Ψ at a generic position (x, y, z) off the (x, z) plane can be computed from the corresponding value $\Psi(\tilde{x}, 0, \tilde{z})$ on the (x, z) plane, where

$$\tilde{x} = (x + y)^{1/2} , \qquad \tilde{z} = z . \tag{2.40}$$

Clearly, since the solution of the evolution equations is computed only on the (x, z) plane, interpolations (with truncation errors smaller than that of the finite-difference operators) are needed at all the positions $(\tilde{x}, y = 0, \tilde{z})$ (see Fig 2.3).
Overall the Cartoon method represents the choice for many codes and it has been implemented with success in many applications, *e.g.*, [2–8, 41, 62] to cite a few.

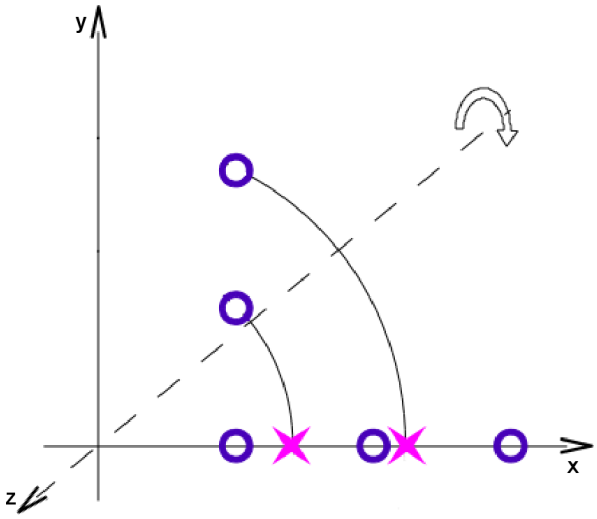

Figure 2.4: illustrates the idea of the `Cartoon` method. The picture shows a projection of figure 2.3 onto the x-y plane. The black dots mark the grid points of the Cartesian grid. This point is needed e.g., in order to calculate a second derivative. To determine the value of a certain point the properties of axisymmetry are used. Any point on a circle around the z axis has the same numerical value. The radius of a circle, which is the distance of a dot to the origin, show the corresponding point on the x axis. The value of the point, where the circle crosses the x axis is calculated by a third-order interpolation.

Chapter 3

Einstein equations non vacuum space-times

3.1 Relativistic hydrodynamics

While the previous chapter discusses the properties of space-time without matter ($T_{\mu\nu} = 0$), this chapter, about relativistic hydrodynamics, explains physics of space-time when matter is included. Since the phenomena considered in relativistic hydrodynamics are macroscopic, the fluid is regarded as a continuous media. In this work we only consider *ideal fluids* [1] , neglecting any kind of non ideal effects such as dissipation or heat fluxes. The properties of fluids in relativistic hydrodynamics are described by its stress- energy tensor (3.40) and a certain EoS.

3.1.1 A thermodynamical consideration of hydrodynamics

Later we will study several properties of neutron stars, which can be only described by thermodynamics or statistical physics. Because of this we will give a brief introduction in thermodynamic aspects of hydrodynamics. The introduction follows the first chapter in [63].
Hydrodynamics is as well as GR a continuous field theory and as mentioned before it describes the dynamics of continuous media. [2] In order to set up an mathematical description of the state of a moving fluid we need functions, which give the distribution of the fluid velocity $\mathbf{v} = \mathbf{v}(x, y, z, t)$ and of any two thermodynamic quantities pertaining to the fluid, for instance the rest mass density $\rho = \rho(x, y, z, t)$ and the pressure $p = p(x, y, z, t)$ [3].
All these quantities are functions of the coordinates x, y, z, t. $\mathbf{v} = \mathbf{v}(x, y, z, t)$ is the velocity of the fluid at a given point (x, y, z, t), i.e. refers to fixed points in space and time and not to specific particles of the fluid. The same remarks apply to ρ and p.
The next pages show a brief deduction of the equations of Newtonian hydrodynamics. We start with

[1] Fluids in which thermal conductivity and viscosity can be neglected are called *ideal*.

[2] This means that any small volume element in the fluid is always supposed so large that it still contains a very great number of molecules. Accordingly, when speaking of infinitely small elements of volume, we shall always mean those which are "physically" infinitely small, i.e. very small compared with the volume of the body under consideration, but large compared with distance between molecules. The expressions fluid particle and point in a fluid are to be understood in a similar sense. If, for example, we speak of the displacement of some fluid particle, we mean not the displacement of an individual molecule, but that of a volume element containing many molecules, though still regarded as a point.

[3] All the thermodynamic quantities are determined by the values of any two of them, together with the equation of state; hence, if we are given five quantities, namely the three components of the velocity $\mathbf{v}$, the density ρ and the pressure p, the state of the moving fluid is completely determined.

the continuity and the Euler equations followed by conservation of entropy for isentropic systems and the equation for conservation of energy.

a) The equation of continuity expresses the conservation of mass in a closed system. We consider a certain amount of fluid in a volume V_e. The mass of the fluid in this volume is expressed by the integral $\int \rho dV$, where ρ is the density of the fluid, integrated over the volume V_e. The mass of fluid flowing in unit time through a surface element $\mathrm{d}\mathbf{f}$ of V_e is $\rho \mathbf{v} d\mathbf{f}$; the vector $\mathrm{d}\mathbf{f}$ is equal to the area of the surface element and its direction is perpendicular to the surface. If $\mathrm{d}\mathbf{f}$ is taken along the outward normal $\rho \mathbf{v} d\mathbf{f}$ is positive if the fluid flowing out of the volume, and negative if the flow is into the volume. The total flux over the whole closed surface surrounding the volume V_e is given by the integral

$$\oint \rho \mathbf{v}\ d\mathbf{f}. \tag{3.1}$$

Corresponding to the flux outwards the decrease per unit time in the mass of the fluid in $\mathbf{V_e}$ can be written

$$-\frac{\partial}{\partial t} \int \rho\ dV \tag{3.2}$$

As long there is no sink or source of fluid the sum of the equation (3.1) and (3.2) is zero

$$\frac{\partial}{\partial t} \int \rho\ dV\ +\ \oint \rho \mathbf{v}\ d\mathbf{f}\ =\ 0. \tag{3.3}$$

Using **Gauss** law to transform the surface integral into a volume integral equation (3.3) becomes

$$\int \left[\frac{\partial}{\partial t} \rho\ +\ \nabla \cdot (\rho \mathbf{v}) \right] dV\ =\ 0. \tag{3.4}$$

The integral equation is true if the integrand vanishes i.e.

$$\frac{\partial}{\partial t} \rho\ +\ \nabla \cdot (\rho \mathbf{v})\ =\ 0, \tag{3.5}$$

This is the *equation of continuity*. The vector

$$\mathbf{j} = \rho \mathbf{v} \tag{3.6}$$

is called the mass *mass flux density*. Its direction is that of the motion of the fluid, while its magnitude equals the mass of fluid flowing in unit time through unit area perpendicular to the velocity.

b) Euler‘s equation which are the equation of motion of a fluid, were first obtained by **L. Euler in 1755** and it is a fundamental equation of fluid dynamics.
Let us consider the total force acting on some volume V_e of the fluid which is equal to the integral

$$\mathbf{F}\ =\ -\oint p\ d\mathbf{f}, \tag{3.7}$$

of the pressure, taken over the surface bounding the volume. Using **Stoke‘s** law to transform it in a volume integral it becomes

$$-\oint p\ d\mathbf{f}\ =\ -\int \nabla p\ dV. \tag{3.8}$$

The pressure influences directly the motion of a fluid element. Equating the force $-\nabla p$ to the product of the mass per unit volume (ρ) and the acceleration $d\mathbf{v}/dt$:

$$\rho\frac{d\mathbf{v}}{dt} = -\nabla p \tag{3.9}$$

The derivative $d\mathbf{v}/dt$ which appears here denotes not the rate of change of the fluid velocity at a fixed point in space, but the rate of change of the velocity of a given fluid element as it moves in space. This derivative has to be expressed in terms of the velocity of the given fluid element during the time dt in the velocity at a point fixed in space. To do so, we notice that the change $d\mathbf{v}$ the velocity is composed of two parts, namely the change during dt at a point fixed in space, and the difference between the velocities (at the same instant) at two points $d\mathbf{r}$ apart, where $d\mathbf{r}$ is the distance moved by the given fluid particle during the time dt. The first part is then $(\partial\mathbf{v}/\partial t)dt$, where the derivative $\partial\mathbf{v}/\partial t$ is taken for constant x, y, z, i.e. at the given point in space. In other words

$$d\mathbf{v} = dt\frac{\partial\mathbf{v}}{\partial t} + dx\frac{\partial\mathbf{v}}{\partial x} + dy\frac{\partial\mathbf{v}}{\partial y} + dz\frac{\partial\mathbf{v}}{\partial z} = dt\frac{\partial\mathbf{v}}{\partial t} + (\mathbf{r}\,\nabla\cdot)\mathbf{v}. \tag{3.10}$$

By dividing both sides by dt equation 3.10 becomes

$$\frac{d\mathbf{v}}{dt} = \frac{\partial\mathbf{v}}{\partial t} + (\mathbf{v}\,\nabla\cdot)\mathbf{v}. \tag{3.11}$$

Put equation (3.11) into equation (3.9) gives

$$\rho\frac{\partial\mathbf{v}}{\partial t} + \rho(\mathbf{v}\,\nabla\cdot)\mathbf{v} + \nabla p = 0. \tag{3.12}$$

c) Conservation of entropy in isentropic systems A lot of numerical studies about relativistic fluids consider *ideal fluids*. Motions of such fluids are adiabatic and do not show any exchange of heat between different parts of the fluid. The entropy of any particle in adiabatic motion through space remains constant. It means that the whole entropy of a closed system does not change in time

$$\frac{ds}{dt} = 0, \tag{3.13}$$

where s is the entropy per mass unit. The total derivative with respect to time denotes the rate of change of entropy for a given fluid particle as it moves about

$$\frac{\partial s}{\partial t} + \mathbf{v}\,\nabla s = 0 \tag{3.14}$$

$$\frac{\partial(\rho s)}{\partial t} + \nabla\cdot(\rho s\mathbf{v}) = 0, \tag{3.15}$$

where $\rho s\mathbf{v}$ is the specific entropy flux.

d) The energy flux of some volume element V_e fixed in space, describes the variation of energy. The energy of a unit volume of fluid is

$$\left(\frac{\rho v^2}{2} + \rho\epsilon\right), \tag{3.16}$$

where the first term is the kinetic energy and the second term the internal energy. The variation of the energy in time is given by

$$\frac{\partial}{\partial t}\left(\frac{\rho v^2}{2} + \rho\epsilon\right), \tag{3.17}$$

In order to calculate this quantity, the term of the kinetic energy can be reformulated by using equations (3.5) and (3.12)

$$\frac{\partial}{\partial t}\left(\frac{\rho \mathbf{v}^2}{2}\right) = \frac{\mathbf{v}^2}{2}\nabla\cdot(\rho\mathbf{v}) - \mathbf{v}\nabla p - \rho\mathbf{v}(\mathbf{v}\nabla)\mathbf{v}. \tag{3.18}$$

Now the last term $\mathbf{v}(\mathbf{v}\nabla\cdot)\mathbf{v}$ is substituted by $\frac{\mathbf{v}}{2}\nabla\cdot\mathbf{v}^2$. Using the first law of thermodynamics the gradient of the pressure ∇p can be replaced by $\rho\nabla w$ or $\rho T\nabla s$, where w is the heat function per unit mass and T the temperature, and obtain for (3.18),

$$\frac{\partial}{\partial t}\left(\frac{\rho v^2}{2}\right) = \frac{v^2}{2}\nabla\cdot(\rho\mathbf{v}) - \rho\mathbf{v}\nabla\cdot\left(\frac{v^2}{2} + w\right) + \rho T\mathbf{v}\nabla s. \tag{3.19}$$

Using the thermodynamic relation

$$d(\rho\epsilon) = \epsilon d\rho + \rho d\epsilon = w d\rho + \rho T ds, \tag{3.20}$$

and the general adiabatic equation (3.14) the new expression of $\frac{\partial}{\partial t}\rho\epsilon$ ends in

$$\frac{\partial(\rho\epsilon)}{\partial t} = w\frac{\partial\rho}{\partial t} + \rho T\frac{\partial s}{\partial t} = -w\,\nabla\cdot(\rho\mathbf{v}) - \rho T\mathbf{v}\nabla s. \tag{3.21}$$

Combining the equation of kinetic and internal energy, the change of the energy is to be

$$\frac{\partial}{\partial t}\left(\frac{\rho v^2}{2} + \rho\epsilon\right) = -\nabla\cdot\left[\rho\mathbf{v}\left(\frac{v^2}{2} + w\right)\right]. \tag{3.22}$$

In order to see the meaning of this equation, it has to be integrated it over some volume and becomes

$$\frac{\partial}{\partial t}\int\left(\frac{\rho v^2}{2} + \rho\epsilon\right)dV = -\oint\rho\mathbf{v}\left(\frac{v^2}{2} + w\right)d\mathbf{f}. \tag{3.23}$$

The left term describes the rate of change of the energy of the fluid in a certain volume. The right term it therefore the amount of energy flowing out of this volume in unit time. Expression

$$\rho\mathbf{v}\left(\frac{v^2}{2} + w\right) \tag{3.24}$$

is called the energy flux density vector [4]. The expression (3.24) shows that any unit mass of fluid carries with it an amount $w + \frac{1}{2}v^2$. The fact that the heat function w appears here, and not the internal energy ϵ, has a simple physical significance. Putting $w = \epsilon + p/\rho$, we can write the flux of energy through a closed surface in form

$$-\oint\rho\mathbf{v}\left(\frac{v^2}{2} + w\right)d\mathbf{f} = -\oint\rho\mathbf{v}\left(\frac{v^2}{2} + \epsilon\right)d\mathbf{f} - \oint p\mathbf{v}d\mathbf{f}. \tag{3.25}$$

The first term in the energy (kinetic and internal) transported through the surface in unit time by the mass of fluid. The second term is the work done by pressure forces on the fluid within the surface.

[4] Its magnitude is the amount of energy in unit time through unit area perpendicular to the direction of the velocity.

3.1.2 Digression about quasi-linear hyperbolic partial differential equations

The homogeneous system of m partial differential equations (PDEs)

$$\partial_t u^c(x,t) + \sum_{b=1}^{m} a^{cb}(x,t)\partial_x u^b(x,t) = 0 \tag{3.26}$$

or, in matrix notation,

$$\partial_t \mathbf{U}(x,t) + \mathbf{A}(x,t)\partial_x \mathbf{U}(x,t) = 0 \tag{3.27}$$

is said to *quasi-linear* if the matrix $\mathbf{A}$ of the coefficients is a function of $\mathbf{U}$ only and is said to be *hyperbolic* if $\mathbf{A}$ is diagonalizable with a set of real eigenvalues $\lambda_1, ..., \lambda_m$ and a corresponding set of *m* linearly-independent right eigenvectors $\mathbf{R}^{(1)}, ...\mathbf{R}^{(m)}$ such that,

$$\mathbf{A}\mathbf{R}^{(a)} = \lambda_a \mathbf{R}^{(a)}. \tag{3.28}$$

Furthermore, if all the eigenvalues λ_a are distinct, the system is said to be *strictly hyperbolic*. When a system PDEs is written in the form.

$$\partial_t \mathbf{U} + \partial_x[\mathbf{F}(\mathbf{U})] = 0, \tag{3.29}$$

it is said to be a *conservative form*. In this case it can also be written in form (3.28) with $\mathbf{A}(\mathbf{U}) \equiv \partial\mathbf{F}(\mathbf{U})$ begin the Jacobian of the flux vector $\mathbf{F}(\mathbf{U})$. In a conservative system, knowledge of the state vector $\mathbf{U}(x,t)$ at one point in spacetime allows to determine the flux for each state variable. It will be shown that this is the case for the hydrodynamics equations. It was shown by Lax and Wendroff [64] in a theorem that, if shocks are present, converging conservative numerical methods, *i.e.* methods relying on a conservative form or the equations, converge to the *weak solution* [5] of the problem, while non conservative methods generally do not. Furthermore, Hou and LeFloch [65] demonstrated that, in general, a non-conservative scheme will converge to the wrong weak solution in the presence of a shock an hence they underlined the importance of flux-conservation formulations.
In order to appreciate the importance of a conservative formulation of the hydrodynamics equation, consider the prototype of a hyperbolic equation in conservative form, that is the scalar linear advection equation in one dimension

$$\partial_t u(x,t) + \lambda\partial_x u(x,t) = 0, \tag{3.30}$$

with initial conditions at $t = 0$

$$u(x,0) = u_0(x). \tag{3.31}$$

The solution of (3.30) is easily calculated and is given by

$$u(x,t) = u(x - \lambda t, 0) \tag{3.32}$$

for $t \geq 0$. As time evolves, the initial data simply propagates unchanged with speed $|\lambda|$ toward the right or the left according to the sign of λ, which is called *characteristic speed*. The *characteristic curves* of the equation are the curve $x - t$ plane satisfying the ordinary differential equation (ODE) with initial data $x'(t) = -lambda\,; x(0) = x_0$. The solution *u(x,t)* is constant along a characteristic curve

$$\frac{du(x(t),t)}{dt} = 0 \quad \text{when} \quad x = x_0 - \lambda t. \tag{3.33}$$

[5] Weak solutions are solutions of the integral form of the conservation system; they are continuous and differentiable of have at most a finite number of discontinuities.

The notation can be extended to a system of *m* hyperbolic PDEs like (3.27). Since, by definition, the hyperbolic condition guarantees that a complete set of right eigenvectors $\mathbf{R}^{(a)}$ exists, if we indicate with $\mathbf{K}$ the matrix whose columns are the $\mathbf{R}^{(a)}$, then

$$\Lambda \,=\, \mathbf{K}^{-1}\mathbf{A}\mathbf{K}, \tag{3.34}$$

where

$$\Lambda \,=\, diag(\lambda_1, \lambda_2, ..., \lambda_m). \tag{3.35}$$

That is true for a linear system, where $\mathbf{A}$ is a matrix of constant coefficients. Introducing now the *characteristic variables*

$$\mathbf{W} \,\equiv\, \mathbf{K}^{-1}\mathbf{U}, \tag{3.36}$$

system (3.27) becomes

$$\partial_t \mathbf{W} \,+\, \Lambda \partial_x \mathbf{W} \,=\, 0. \tag{3.37}$$

This is called *canonical form* of the system and consists of *m* decoupled independent advection equations, each of which has solution

$$w^a(x,t) \,=\, w^a(x - \lambda_a t, 0). \tag{3.38}$$

The solution of the original system is found from the one of the canonical system through inversion of (3.36), that is $\mathbf{U} \,=\, \mathbf{K}\mathbf{W}$ or, in components,

$$\mathbf{U}(x,t) \,=\, \sum_{a=1}^{m} w^a(x,t)\mathbf{K}^{(a)} \,=\, \sum_{a=1}^{m} w^a(x - \lambda_a t, 0)\mathbf{K}^{(a)}. \tag{3.39}$$

From the last relation it is clear that the solution can be written as the superposition of *m* waves, each propagating undistorted with a speed given by the corresponding eigenvalues.

3.1.3 Equations of relativistic hydrodynamics

An important feature of many multidimensional non-vacuum numerical-relativity codes that solve the coupled Einstein–hydrodynamics equations in Cartesian coordinates is the adoption of a *conservative* formulation of the hydrodynamics equations [66, 67]. In such a formulation, the set of conservation equations for the stress-energy tensor

$$T^{\mu\nu} \,=\, \rho h u^\mu u^\nu \,+\, p g^{\mu\nu}. \tag{3.40}$$

and for the matter current density

$$J^\mu \,=\, \rho u^\mu \tag{3.41}$$

that is

$$\nabla_\mu J^\mu = 0\,, \tag{3.42}$$

$$\nabla_\mu T^{\mu\nu} = 0\,, \tag{3.43}$$

is written in a hyperbolic first-order "flux-conservative" form of the type [68]

$$\frac{1}{\sqrt{-g}}\{\partial_t[\sqrt{\gamma}\mathbf{F}^0(\mathbf{U})] \,+\, \partial_i[\sqrt{-g}\mathbf{F}^{(i)}(\mathbf{U})]\} \,=\, \mathbf{s}(\mathbf{U}), \tag{3.44}$$

where $\mathbf{F}^{(i)}(\mathbf{U})$ and $\mathbf{s}(\mathbf{U})$ are the flux vectors and source terms, respectively [69]. Note that the right-hand side (the source terms) depends only on the metric, on its first derivatives and on the stress-energy tensor. Furthermore, while the system (3.44) is not strictly hyperbolic, strong hyperbolicity is recovered in a flat spacetime, where $\mathbf{s}(\mathbf{U}) = 0$. As shown by [67], in order to write the system (3.42)–(3.43) in the form of system (3.44), the *primitive* hydrodynamical variables (*i.e.* the rest-mass density ρ, the pressure p measured in the rest-frame of the fluid, the fluid 3-velocity v^i measured by a local zero-angular momentum observer, the specific internal energy ϵ and the Lorentz factor W) are mapped to the so called *conserved* variables $\mathbf{U} \equiv (D, S^i, \tau)$ via the relations

$$\begin{aligned} D &\equiv \sqrt{\gamma}\rho W\,, \\ S^i &\equiv \sqrt{\gamma}\rho h W^2 v^i\,, \\ \tau &\equiv \sqrt{\gamma}\left(\rho h W^2 - p\right) - D\,, \end{aligned} \tag{3.45}$$

where $h \equiv 1 + \epsilon + p/\rho$ is the specific enthalpy and $W \equiv (1 - \gamma_{ij} v^i v^j)^{-1/2}$.
The advantage of a flux-conservative formulation is that it allows to use high-resolution shock-capturing (HRSC) schemes, which are based on Riemann solvers and which are essential for a correct representation of shocks. This is particularly important in astrophysical simulations, where large shocks are expected. In this approach, all variables $\mathbf{U}$ are represented on the numerical grid by cell-integral averages. The function is then *reconstructed* within each cell, usually through piecewise polynomials, in a way that preserves the conservation of the variables $\mathbf{U}$. This gives two values at each cell boundary, which are then used as initial data for the (approximate) Riemann problem, whose solution gives the flux through the cell boundary.

3.1.4 Equation of state

In whatever coordinate system they are written, the system of hydrodynamics equations can be closed only after specifying an additional equation, the equation of state (EOS), which relates the pressure to the rest-mass density and to the energy density. The code has been written to use any EOS, but all the tests and the results promoted in this thesis have been performed using either an (isentropic) polytropic EOS

$$p = K\rho^{\Gamma}\,, \tag{3.46}$$

$$e = \rho + \frac{p}{\Gamma - 1}\,, \tag{3.47}$$

or an "ideal-fluid" non-isentropic EOS

$$p = (\Gamma - 1)\rho\,\epsilon\,. \tag{3.48}$$

Here, e is the energy density in the rest frame of the fluid, K the polytropic constant (not to be confused with the trace of the extrinsic curvature defined earlier) and Γ the adiabatic exponent. In the case of the polytropic EOS (3.46), $\Gamma = 1 + 1/N$, where N is the polytropic index and the evolution equation for τ does not need to be solved, because it can be computed form the algebraic relation. In the case of the ideal-fluid EOS (3.48), on the other hand, non-isentropic changes can take place in the fluid and the evolution equation for τ needs to be solved. Note that the polytropic EOS (3.46) is isentropic and thus does not allow for the formation of physical shocks, in which entropy (and internal energy) can be increased locally (shock heating).

3.2 Relativistic hydrodynamics in cylindrical coordinates and axisymmetry

In the following section, the general equations of relativistic hydrodynamics are transformed to cylindrical coordinates and reduced to axisymmetry. Coordinates which are adapted to the geometry of the problem are useful for simulations of objects, which impose a certain symmetry. Duez et al. [70] and Zink et al. [71] showed that tori, formed by collapsing rotating stars, fragment in non-axisymmetric clumps possibly because of $m = 4$ modes produced intrinsically by the Cartesian grid. As mentioned before cylindrical grids would reduce this effect and indicate whether this instability is genuine, but suffers form a singularity axis and singular terms in the equations which require a special treatment.

3.2.1 `Flux Conserved` and `Balance Law` formulations of hyperbolic differential equations.

The Newtonian or the special relativistic formulation of the hydrodynamic equations in Cartesian coordinates are classified by certain type of equations

$$\partial_t q(x,t) \, + \, \partial_x (f(q(x,t))) \, = \, 0, \tag{3.49}$$

in which $f(q(x,t))$ is in this case the product of the variable $q(x,t)$ with a velocity $v(x,t)$. Following the description about conservation laws of [68], (3.49) is written in a flux-conserved formulation. A simple coordinate transformation of the hydrodynamic equations or the consideration of cylindrical coordinates adds geometrical terms which can not be written as fluxes. To retain terms properties of flux conservation all terms which can not be written as fluxes are written on to the right hand side and become sources. Equation (3.49) changes to

$$\partial_t q(r,t) \, + \, \partial_r (f(q(r,t))) \, = \, \psi(q(r,t)), \tag{3.50}$$

where $\psi(q(x,t))$ is the sum of all source terms. Equations like (3.50) are written in a "flux-balanced" formulation.

3.2.2 A new formulation of the equations of relativistic hydrodynamics in axisymmetry

As mentioned in the previous Section, following ref. [4], we write the relativistic hydrodynamics equations (3.42)–(3.43) in a first-order form in space and time using cylindrical coordinates (r, ϕ, z). However, as an important difference from the approach suggested in ref. [4], we do not introduce source terms that contain coordinate singularities. Rather, we re-define the conserved quantities in such a way to remove the singular terms, which are the largest source of truncation error, also when evaluated far from the axis.

We illustrate our approach by using as a representative example the continuity equation. This is the simplest of the five hydrodynamical equations but already contains all the basic elements necessary to illustrate the new formulation. We start by using the definitions for the conserved variables (3.45) to write eq. (3.42) generically as

$$\partial_t(\sqrt{\gamma}\rho W) + \partial_i \left[\sqrt{\gamma}\rho W \left(\alpha v^i - \beta^i\right)\right] = 0\,, \tag{3.51}$$

which in cylindrical coordinates takes the form

$$\partial_t(\sqrt{\tilde{\gamma}}\rho W) + \partial_r \left[\sqrt{\tilde{\gamma}}\rho W \left(\alpha v^r - \beta^r\right)\right] + \partial_z \left[\sqrt{\tilde{\gamma}}\rho W \left(\alpha v^z - \beta^z\right)\right] = 0\,, \tag{3.52}$$

where $\sqrt{\tilde{\gamma}}$ is the determinant of the 3-metric in cylindrical coordinates and where we have enforced the condition of axisymmetry $\partial_\phi = 0$. Because any ϕ-constant plane in cylindrical coordinates can be mapped into the (x, z) plane in Cartesian coordinates, we consider equation (3.52) as expressed in Cartesian coordinates and restricted to the $y = 0$ plane, *i.e.*,

$$\partial_t(xD) + \partial_x \left[xD\left(\alpha v^x - \beta^x\right)\right] + \partial_z \left[xD\left(\alpha v^z - \beta^z\right)\right] = 0\,, \tag{3.53}$$

where we have exploited the fact that for any vector of components A^i on this plane $A^r = A^x,\ A^\phi = A^y/x$ and $\tilde{\gamma} = x^2\gamma$, with γ being the determinant of the 3-metric in Cartesian coordinates. Equation (3.53) represents the prototype of the formulation proposed here, which we will refer to hereafter as the *"new"* formulation to contrast it with the formulation adopted so far, *e.g.*, in ref. [4], for the solution of the relativistic hydrodynamics equations in axisymmetry and in Cartesian coordinates. The only, but important, difference with respect to the *"standard"* formulation is that in the latter the derivative in the x-direction is written out explicitly and becomes part of the source term $\mathbf{s}(\mathbf{q})$, *i.e.*,

$$\partial_t(D) + \partial_x \left[D\left(\alpha v^x - \beta^x\right)\right] + \partial_z \left[D\left(\alpha v^z - \beta^z\right)\right] = -\frac{D\left(\alpha v^x - \beta^x\right)}{x}\,. \tag{3.54}$$

Even though the right-hand-side of eq. (3.54) is never evaluated at $x = 0$ (because no grid points are located at $x = 0$), both the numerator and the denominator of the right-hand-side of eq. (3.54) are very small for $x \simeq 0$, so that small round-off errors in the evaluation of the right-hand-side can increase the overall truncation error. Stated differently, the right-hand-side of eq. (3.54) becomes stiff for $x \simeq 0$ and this opens the door to the problems encountered in the numerical solution of hyperbolic equations with stiff source terms [72].

What was done for the continuity equation (3.53) can be extended to the other hydrodynamics equations which, for the conservation of momentum in the x- and z-directions, take the form

$$\begin{aligned}
&\frac{1}{\alpha x\sqrt{\gamma}}\Big\{\partial_t\left(xS_A\right) + \partial_x\left[x\left(S_A\left(\alpha v^x - \beta^x\right) + \alpha\sqrt{\gamma}p\delta^x_A\right)\right] + \\
&\qquad\qquad \partial_z\left[x\left(S_A\left(\alpha v^z - \beta^z\right) + \alpha\sqrt{\gamma}p\delta^z_A\right)\right]\Big\} = \\
&\left[T^{00}\left(\frac{1}{2}\beta^l\beta^m\partial_A\gamma_{lm} - \alpha\partial_A\alpha\right) + T^{0i}\beta^l\partial_A\gamma_{il} + T^0_i\partial_A\beta^i + \frac{1}{2}T^{lm}\partial_A\gamma_{lm}\right]\,,
\end{aligned} \tag{3.55}$$

with $A = x, z$. Similarly, the evolution of the conserved angular momentum $S_\phi = xS_y$ is expressed as

$$\frac{1}{\alpha x\sqrt{\gamma}}\Big\{\partial_t\left(x^2S_y\right) + \partial_x\left[x^2S_y\left(\alpha v^x - \beta^x\right)\right] + \partial_z\left[x^2S_y\left(\alpha v^z - \beta^z\right)\right]\Big\} = 0\,, \tag{3.56}$$

while the equation of the energy conservation is given by

$$\begin{aligned}
&\frac{1}{\alpha x\sqrt{\gamma}}\Big\{\partial_t\left(x\tau\right) + \partial_x\left[x\left(\tau\left(\alpha v^x - \beta^x\right) + pv^x\right)\right] + \partial_z\left[x\left(\tau\left(\alpha v^z - \beta^z\right) + pv^z\right)\right]\Big\} = \\
&\qquad T^{00}\left(\beta^i\beta^jK_{ij} - \beta^i\partial_i\alpha\right) + T^{0i}\left(-\partial_i\alpha + 2\beta^jK_{ij}\right) + T^{ij}K_{ij}\,.
\end{aligned} \tag{3.57}$$

The changes made to the formulation are rather simple but, as we will show in Section 5, these can produce significant improvements on the overall accuracy of the simulations with a truncation error

at least one order of magnitude smaller for all of the tests considered. Because of its simplicity, the changes in the new formulation of the equations can be implemented straightforwardly in codes written using the standard formulation. Finally, we note that both eq. (3.54) and eq. (3.53) are written in a flux-conservative form in the sense that the source term does not contain first-order spatial derivatives of the conserved variables. More precisely, eq. (3.53) is written in a flux-conservative form, while eq. (3.54) is written in a "flux-balanced" form, as it is typical for flux-conservative equations written in curvilinear coordinates [68]. The same is true also for eqs. (3.55)–(3.57) and for the corresponding equations presented in ref. [4], which are incorrectly classified as non flux-conservative.

Part III

The `Whisky2D` code

Chapter 4

Numerical methods to solve the equations of relativistic hydrodynamics

4.1 Ideas and methods behind the `Whisky2D` code

Already in the introduction we discussed the physical motivations of axisymmetric systems. While the previous Chapter gave an overview about the mathematical structure of the axisymmetric relativistic equations, this Chapter deals with the numerical methods to solve the equations and the construction of the `Whisky2D` code.

The work flow of the `Whisky2D` code is shown in figure 4.1. The work flow begins with the calculation of the initial data. The `CCATIE` codes provides a collection of methods to calculate different initial configurations of neutron stars and black holes.

The work flow by itself is include two loops. The outer loop is responsible for calculating the progress in time. The inner loop contains the methods to solve the spatial part - x and z direction - of the equations of hydrodynamics.
At the first step, the outer cycle starts with the calculation of the source terms. The source terms are also part of the spatial calculation of the equations, but unlike the flux terms, they are independent of a spatial direction. Afterwards the code enters the inner loop in order to calculate the fluxes over the cell boundaries. It begins with the reconstruction of the primitive values at the cell boundaries (section 4.2.3). Followed by the conversion of the primitive variables to conserved variables. Different values at bordering cell boundaries causes fluxes between the cells. In the next step the Riemann Solver module (section 4.2.2) calculates the fluxes between all cell boundaries. Finally all values of the fluxes and the source terms are added up in the RHS module. The inner loop is repeated two times once for the z direction and a second one for the x direction. After the inner loop is finished a first check of the atmosphere (section 4.2.6) will be done. The first atmosphere check is used to exclude all atmosphere grid points from time-integration in order to accelerate the code.
The outer cycle continues with the time-integration, followed by the setting of the boundary conditions. The next module converses the conserved variables back to primitive variables (section 4.2.5). After finishing one cycle of the outer-loop, a second atmosphere check will be done.

The work-flow can be extended by a further loop to calculate the progress of space-time variables. Numerical method to do such calculations are provided by tools of the `CCATIE` code which

solves the equations of the BSSNOK formalism. The required values of the stress-energy tensor is calculated by Whisky2D at the end of any time-step.
Finally the data of a time-step n are written in a separate files. The code finishes if a pretended number of iteration or run-time is reached. The final step, before a run stops, an analysis tool determines run time and computing resources of all used computing modules. The informations are written in data files.

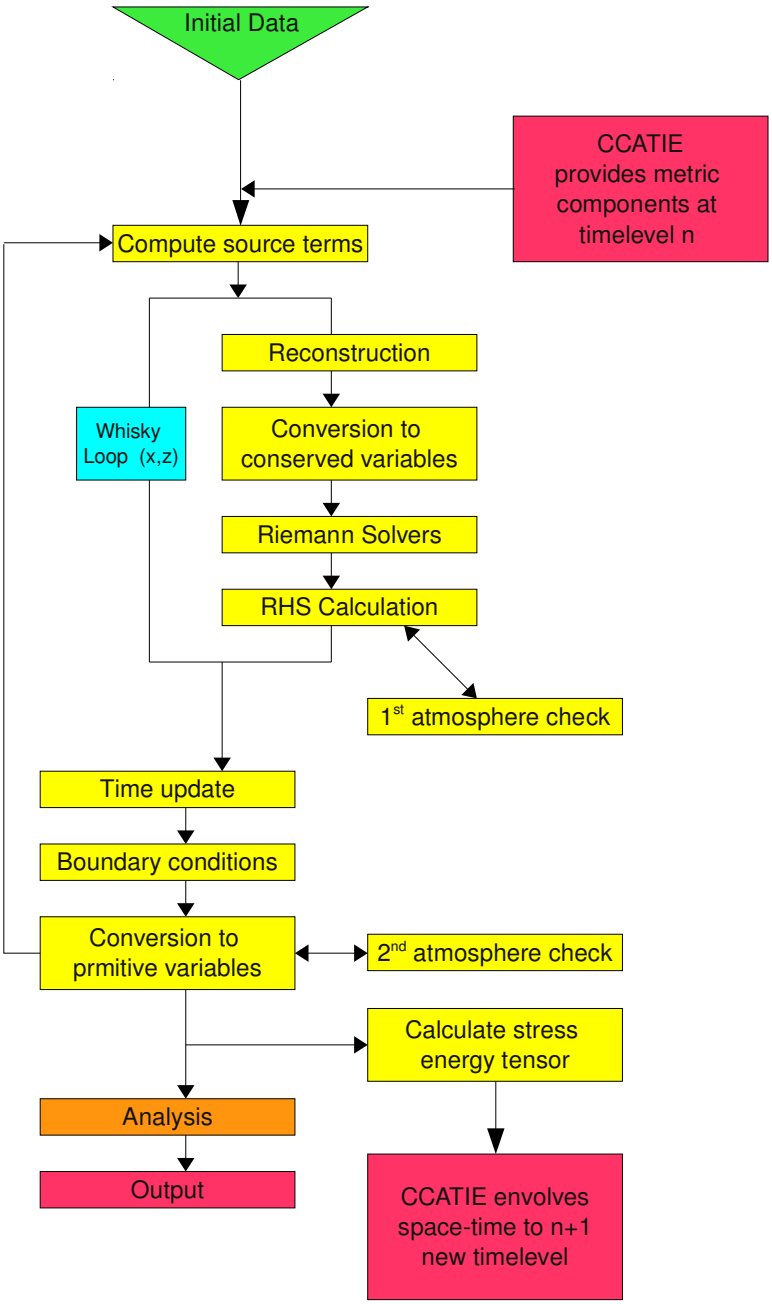

Figure 4.1: Flow chart of the different steps of the Whisky2D code. The green field show the input symbolises the initial data routines. The Whisky2D routines are yellow colored. The loop over the different directions in space are marked with a blue label. Analysis tools to extract additional informations are orange colored. CCATIE routines, including MoL, Cartoon, spacetime evolution could and much more other methods are colored red.

4.2 Numerical methods

4.2.1 Discontinuities and Godunov methods

Any-finite difference method for solving PDEs for initial-value problems will involve the discretization of the physically continuous initial data to be evolved with the differential equations; the numerical initial data and solution are thus discontinuous and piecewise constant (see figure 4.2.1). In addition to this, the non-linear properties of the hydrodynamical equations can generally produce (see e.g. the Burgers equation [73]) in a finite time non-linear waves with discontinuities even from smooth initial data [68, 74]. High-Resolution Shock-Capturing methods - based on a simple and brilliant idea by Godunov [75] not only can treat accurately discontinuities, but indeed they exploit them. In fact, Godunov methods consist in setting and solving at every cell interface of the numerical grid a local Riemann problem, for whose solution there exist several accurate and efficient methods, both exact and approximate. The basic structure of a HRSC scheme [76, 77] consists of the following stages:

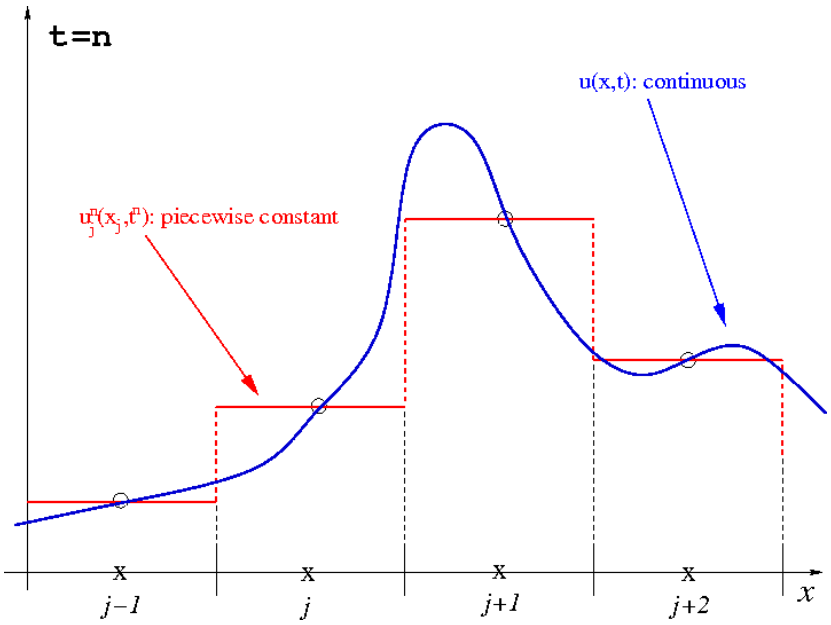

Figure 4.2: Schematic picture of the process of discretization. The continuous function $U(x,t)$ is approximate by a piecewise constant function U_j^n on the numerical grid. As a result, a series of Riemann problems is set up at each interface between the cells. (Figure courtesy of L. Rezzolla)

- converting the primitive variables to conserved variables;
- finding the values of these variables at cell interfaces, *i.e.* at the intermediate locations $x_{p+1/2}$ between all pairs of grid points x_p and x_{p+1}, except for the grid points near the boundaries, which are treated separately; there are two such *extended or reconstructed values* at each cell interface (one being computed from the left stencil, the other from the right stencil) and they are used as initial data for a local Riemann problem;
- solving the local Riemann problem at each cell interface; this gives the fluxes used for the time integration;

- computing the source terms and adding them to the fluxes from the Riemann solver;
- integrating one step in time;
- applying boundary conditions;
- converting back from the evolved conserved variables to obtain the primitive variables at the updated time.

It is computationally convenient to apply the above procedure as a sequence of three 1-dimensional operations, i.e. using what is referred to as dimensional splitting and which is constructed using Taylor series expansions of the 3-dimensional function [68].

4.2.2 Riemann solvers

In what follows, we discuss how Riemann solvers can be used to solve accurately the hydrodynamics equations. For simplicity we consider equations in one spatial dimension only. The Riemann problem is said to be solved when the velocity, pressure and density in the new states $\mathbf{U}_L^*$ and $\mathbf{U}_R^*$ have been computed, as well as the positions of the waves separating the four states. The solution of the 1-dimensional Riemann problem in relativistic hydrodynamics was discussed in the general case by Marti and Müller [78] and the reader is referred to their work for further details (see also [79], for the extension to multi dimensions).
The knowledge on the wave structure is exploited in the procedure to find the exact solution of the Riemann problem: since pressure and velocity are continuous on the contact discontinuity $\mathcal{C}$, the pressure $\mathbf{U}_{L,R}^*$ in the states can be calculated by imposing the continuity of the fluid velocity across $\mathcal{C}$

$$v_L^*(p^*) \, = \, v_r^*(p^*). \tag{4.1}$$

In general, (4.1) is a non-linear algebraic equation in the unknown pressure p^* and requires a numerical solution even for simple EoSs [74]. Depending on the different wave patterns forming after the decay of the discontinuity, a different non-linear equation will need to be solved. This initial ambiguity in the wave pattern produced corresponds to the fact that the interval in pressure bracketing the solution is not known a priori. In practice this lack of information was compensated by the use of efficient numerical algorithms which, via a process of trial and error, determine the correct wave pattern and then proceed to the solution of the corresponding non-linear equation [80]. More recently Rezzolla and Zanotti [81] have shown that this possible to predict were pattern by studying the realistic relative velocity between the two states.

a) HLLE In the Riemann solver proposed by Harten, Lax, van Leer [116] and later improved by Einfeldt [90], the central region delimited by the fastest wave moving toward the left and by the fastest wave moving toward the right [with speed λ_L and λ_R respectively; C.3] is approximated by a single state

$$\mathbf{U}_{HLLE} \, = \, \frac{\lambda_R U_R - \lambda_L U_L + F_L - F_R}{\lambda_R - \lambda_L} \tag{4.2}$$

thus disregarding the central contact wave. The resulting numerical flux to be used in the Godunov scheme is

$$\mathbf{F}_{HLLE} \, = \, \frac{\lambda_R F(U_L) - \lambda_L F(U_R) + \lambda_L \lambda_R (U_R - U_L)}{\lambda_R - \lambda_L}. \tag{4.3}$$

The HLLE solver is the simplest Riemann solver implemented in `Whisky2D`. It performs well at rarefaction waves, but, as one should expect, it produces considerable diffusion at contact discontinuities.

b) Roe solver The Roe Riemann solver consists in approximating the non-linear system with a linearised one and then in solving the latter exactly. In this case linearised Jacobian matrix $\tilde{\mathbf{A}}(\mathbf{U}_L, \mathbf{U}_R)$ has to satisfy the following conditions:

- hyperbolicity of the system: $\tilde{\mathbf{A}}$ must have real eigenvalues $\tilde{\lambda}_a(\mathbf{U}_L, \mathbf{U}_R)$ and a complete set of linearly independent right eigenvectors $\tilde{\mathbf{R}}^{(a)}$;

- consistency with the exact Jacobian:

$$\tilde{\mathbf{A}}(\mathbf{U}_L, \mathbf{U}_R) \;=\; \mathbf{A}(\mathbf{U});$$

- conservation across discontinuities and exact recognition of isolated discontinuities:

$$\tilde{\mathbf{A}}(\mathbf{U}_L, \mathbf{U}_R)\dot{(}\mathbf{U}_L - \mathbf{U}_R) \;=\; \mathbf{F}(\mathbf{U}_R) - \mathbf{F}(\mathbf{U}_L)$$

These requirements determine the intermediate state $\mathbf{U}_{Roe} \;=\; \mathbf{U}_{Roe}(\mathbf{U}_L, \mathbf{U}_R)$ about which to linearize the original Jacobian matrix $\mathbf{A}$. Although it is possible to find such a state [82], it is more convenient to simply approximate it as

$$\mathbf{U}_{Roe} \;=\; \frac{1}{2}(\mathbf{U}_L, \mathbf{U}_R). \tag{4.4}$$

The eigenvalues $\tilde{\lambda}_a$ and eigenvectors $\tilde{\mathbf{R}}^{(a)}$ computed for $\tilde{\mathbf{A}}(\mathbf{U}_{Roe})$ are then used in the formula (3.39) for the flux across each cell interface:

$$\mathbf{F}_{Roe}^{cellinterface} \;=\; \frac{1}{2}\left\{\mathbf{F}(\mathbf{U}_L) + \mathbf{F}(\mathbf{U}_R) - \sum_{a+1}^{5} \|\tilde{\lambda}_a\|[\omega_L^a - \omega_R^a]\tilde{\mathbf{R}}^{(a)}\right\}, \tag{4.5}$$

where here $a \;=\; 1, \ldots, 5$ since we now specialize the treatment to the specific case of the hydrodynamics equations, which have five variables. We also recall that $\omega_{L,R}^a \;=\; \tilde{\mathbf{L}}^{(a)}(\mathbf{U}_{L,R}) \cdot \mathbf{U}_{L,R}$ are the characteristic variables and that $\tilde{\mathbf{L}}^{(a)}$ are the left eigenvectors of the Jacobian, being the columns of the matrix $\tilde{\mathbf{K}}^{-1}$ (3.34), (3.36). The Roe solver gives a very good approximation to the Riemann solution, except at rarefaction waves, since linear systems do not admit such waves as solution.

c) The Marquina solver [83, 84] can be regarded as an improvement to the Roe solver, since it gives its same results everywhere, except at sonic points (i.e. where the fluid velocity equals the speed of sound), where it removes the entropy violation at rarefaction of the Roe solver. We actually use the modified method of [85] instead of the original method. The procedure consists in computing at each cell interface the characteristic variables $\omega_{L,R}^a$ and the numerical fluxes $\Phi_{L,R}^a \;=\; \mathbf{L}^{(a)} \cdot \mathbf{F}(\mathbf{U}_{L,R})$ for both the left and right states. Then the flux formula is given by

$$\mathbf{F}_{i+1/2}^{Marquina} \;=\; \sum_{a=1}^{5}[\phi_+^a \mathbf{R}_L^{(a)} + \phi_-^a \mathbf{R}_R^{(a)}], \tag{4.6}$$

where the $\Phi_{+,-}^a$ are chosen according to the sign of the eigenvalues:

- $\Phi^a_+ = \Phi^a_L$ and $\Phi^a_- = 0$ if both eigenvectors are positive (i.e. both waves move to the right and so the flux has to be computed from the left state);

- $\Phi^a_- = \Phi^a_R$ and $\Phi^a_+ = 0$ if both eigenvectors are negative;

- if the eigenvalues have opposite sign

$$\begin{aligned} \phi^a_+ &= \frac{1}{2}(\phi^a_L + max(|\lambda^a(\mathbf{U}_L)|, |\lambda^a(\mathbf{U}_R)|)w^a_L), \\ \phi^a_- &= \frac{1}{2}(\phi^a_R + max(|\lambda^a(\mathbf{U}_L)|, |\lambda^a(\mathbf{U}_R)|)w^a_R). \end{aligned} \tag{4.7}$$

In our experience, the Marquina solver has proven to be the best choice.

4.2.3 Reconstruction methods

The original Godunov method, as presented so far, is only first-order accurate in space. Indeed, it was shown by Godunov in a theorem [75] that it is not possible to build monotone (*i.e.* that do not produce spurious oscillations in the vicinity of large gradients) linear schemes of second or higher order of accuracy. As a result, one has to turn higher-order schemes. HRSC methods represent the combination of Godunov type methods, which take advantage of the conservation form of the equations, and of numerical techniques aimed at obtaining second-order (or higher-order) accuracy in the smooth parts of the solution, without producing oscillations.
A way of measuring the amount of oscillations in the solution is to monitor the *total variation* of the solution, defined, for a discretised function $|u^n_p - u^n_{p-1}|$ at time level t^n, as

$$TV(u^n) = \sum_{p=-\infty}^{\infty} |u^n_p - u^n_{p-1}|. \tag{4.8}$$

The requirement of non-oscillation of a scheme may then be stated as the requirement that

$$TV(u^{n+1}) \leq TV(u^n) \tag{4.9}$$

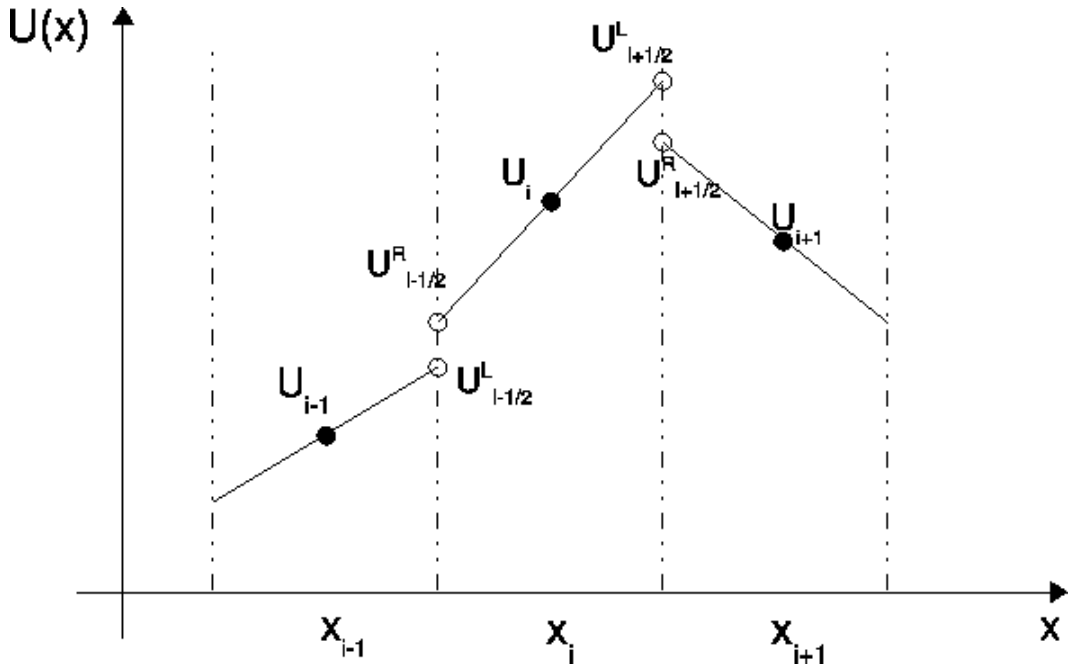

Figure 4.3: shows a systematic picture of the reconstruction procedure. Consider the the cell interface at $U_{i-1/2}$. The values at the left $U^L_{j+1/2}$ and at the right $U^R_{j+1/2}$ of the interface between cells j and $j+1$ define the initial left and right state of a Riemann problem whose solution gives the value of the fluxes a $j+1/2$.

for all variables **U** of the system. A numerical method satisfying this condition is called *total-variation-diminishing* (TVD) method, since the total variation is bounded by its initial value. As shown by Toro [74], TVD methods cannot generally be extended to accuracies higher than second order. In order to construct higher-order methods one has to renounce to the strict TVD condition and allow for an increase of the total variation proportional to some power of the typical size:

$$TV(u^{n+1}) \leq TV(u^n) + \mathcal{O}[(\Delta x)^k]. \tag{4.10}$$

These methods lead to higher-order accuracy also near large-gradients regions, by allowing oscillations (that should be small and bounded) near extrema. The resulting methods are called *Essentially-Non-Ocillatory* (ENO) methods [86].

a) Total-variation-diminishing (TVD) In the original Godunov method, the initial data for the local Riemann problems at each time step are assumed to be piecewise constant on each cell

$$u(x) = u_p, \qquad x_{p-1/2} < x < x_{p+1/2} \qquad \forall p. \tag{4.11}$$

A natural way of increasing the order of accuracy is giving a better approximation of the state at the cell interface. The simplest reconstruction is a piecewise-linear approximation

$$u(x) = u_p + S_p(x - x_p), \qquad x_{p-1/2} < x < x_{p+1/2} \qquad \forall p, \tag{4.12}$$

where S_p is a slope, expressed as either

$$S_p^{upwind} = \frac{u_{p+1} - u_p}{x_{p+1} - x_p}, \quad \text{or} \quad S_p^{downwind} = \frac{u_{p-1} - u_p}{x_{p-1} - x_p} \tag{4.13}$$

or linear combinations of them. The upper superscripts upwind and downwind refer to the stencil used for computing the slope. For grids with uniform spacing, the cell average, computed between $x_{p-1/2}$ and $x_{p+1/2}$, is equal to the value on the mid-grid point for any choice of the slope. All the possible choices of the slope give second-order accurate schemes, but none of them can avoid introducing oscillations in large-variation regions. This problem motivates the technique of *slope limiting*, which consists in choosing a reconstructing slope which is second order in slowly varying regions of the solution and only first order (i.e. piecewise constant) in the vicinity of large-variation regions, in order to avoid numerical oscillations. In practice, the large variation regions are defined as those where S_p^{upwind} and $S_p^{downwind}$ have opposite signs (extrema of the function). The numerous proposed TVD slope limiters differ in the prescription for computing the slope in slowly varying regions. After defining $r \equiv S_p^{upwind} S_p^{downwind}$, the possible slopes can be expressed as a function of r:

$$S = \Phi(r)\frac{S_p^{upwind} + S_p^{downwind}}{2} \tag{4.14}$$

We implemented some of the most commonly used slope limiters, which we list here.

- The *minmod* slope limiter is

$$\Phi(r) = min\left(1, \frac{4}{1+r}\right). \tag{4.15}$$

  Stated differently, minmod consists in choosing the slope with the minimum modulus, when $r > 0$. It is the most diffusive slope limiter.

- The van Leer [87, 88] monotonised centered slope limiter is

$$\Phi(r) = min\left(\frac{2r}{1+r}, \frac{2}{1+3}\right) \tag{4.16}$$

  It consists in limiting the value of the slope in a cell following three rules:
  i) it must not take values beyond the average of the neighbouring slopes;
  ii) it is set to zero if the average of the upwind and downwind slopes relative to the cell is an extremum
  iii) it is set to zero if the average slope and the finite-difference slope have opposite sign, that is if $sign(S_p) = \text{sign}(S_{p+1}) \neq \text{sign}(S_{p+1/2|})$, for any computation of (4.13)

- One more implemented example is the Superbee slope limiter [74]):

$$\Phi(r) = \begin{cases} min(2, r, 2/(1+r)), & \text{if } r \geq 1 \\ 1, & \text{if } 1/2 \leq r < 1 \\ 2r, & \text{if } 0 < r < 1/2. \end{cases} \tag{4.17}$$

TVD reconstruction is simple and computationally the least expensive, but we recall it is at most second-order accurate and drops to first-order at local extrema.

b) The Piecewise Parabolic Method (PPM) The piecewise parabolic method (PPM) of Colella and Woodward is a composite reconstruction method that ensures third-order accuracy [89]. By default we use PPM as this seems to be the best balance between accuracy and computational efficiency, as shown, for example, in [90]. However, there is no standard formulation of this method, so it is useful to compare results with TVD methods as well [91]. All the presented reconstruction methods are stable in the presence of shocks.

4.2.4 Method of lines (MoL)

The reconstruction methods guarantee that a prescribed order of accuracy is retained in space. However, the need to retain a high-order accuracy also in time can complicate considerably the evolution from one time-level to the following one. As a way to handle this efficiently, we have chosen to follow a MoL approach [74, 76]. The MoL is a procedure to separate the space and time discretization processes. First, the continuum equations are considered to be discretised in space only, while leaving the problem continuous in time. This is equivalent to transforming a set of PDEs such into a set of ODEs. Then, the resulting system of ODEs can be solved numerically with any stable solver. This method minimizes the coupling between the spacetime and hydrodynamics solvers and allows for a transparent implementation of different evolution schemes. In practice, this is achieved by integrating equations

$$\partial_t \mathbf{U} + \partial_x \mathbf{F}(\mathbf{U}) \, = \, \mathbf{s}(\mathbf{U}) \tag{4.18}$$

over space in every computational cell defined by its position (x_p, y_q, z_r). Taking, as an example, integration in the x direction, the procedure results in the following ODE

$$\frac{d(\tilde{\mathbf{U}})}{dt} \, = \, \mathbf{L}(\tilde{\mathbf{U}}) \, = \\ \frac{1}{\Delta V}\left[\iiint \mathbf{s}(\mathbf{U}) dx^3 \, + \, \int_{y_{q-1/2}}^{y_{q+1/2}} \int_{z_{r-1/2}}^{z_{r+1/2}} [\mathbf{F}^x(\mathbf{U}(x_{p-1/2}, y, z)) - \mathbf{F}^x(\mathbf{U}(x_{p+1/2}, y, z))] \, dydz \right], \tag{4.19}$$

where $\Delta V \, = \, \Delta x \Delta y \Delta z$ and $\tilde{\mathbf{U}}$ is, in our specific case, the spatially-integrated vector of conserved variables, *i.e.*

$$\tilde{\mathbf{U}} \equiv \frac{1}{\Delta V} \int \mathbf{U} \, dxdydz, \tag{4.20}$$

and $\mathbf{F}^x$ is the x component of the flux five-vector $\mathbf{F}$. Clearly after the space-integration $\tilde{\mathbf{U}}$ does no longer have a space dependence and the PDE is now an ODE.

MoL itself does not have a precise truncation error but, rather, it acquires the truncation order of the time-integration employed, provided that the discrete operator $\mathbf{L}$ is of the same order in space and at least first-order accurate in time. Several integrators are available in our implementation of MoL, including the second-order *Iterative Crank Nicholson* (ICN) solver and *Runge Kutta* (RK) solvers of different orders of accuracy. The second and third-order RK solvers are known to be TVD whilst the fourth-order one is known not to be TVD [92, 93]. As the coupling between the spacetime and the hydrodynamics is only second-order accurate, we typically us the third order RK.

In our implementation of MoL, the right hand side operator $\mathbf{L}(\tilde{\mathbf{U}})$ is simplified by approximating the integrals (4.19) with the midpoint rule

$$\int_a^b g(x)dx \, = \, (b-a) g\big(\frac{a+b}{2}\big) \, + \, \mathcal{O}[(b-a)^2] \tag{4.21}$$

to get, for the flux x-direction.

$$\mathbf{L}(\tilde{\mathbf{U}}) \, = \, \mathbf{s}_{p,q,r} \, + \, \mathbf{F}^{(1)}(\mathbf{U}_{p-1/2,q,r}) \, - \, \mathbf{F}^{(1)}(\mathbf{U}_{p+1/2,q,r}). \tag{4.22}$$

To solve equation (4.19), we use the simplification (4.22) and split the calculation into the following steps:

- calculation of the source terms $\mathbf{s}(\mathbf{U}(x_p, y_q, z_r))$ at all the grid points;
- reconstruction of the data $\mathbf{U}$ to both sides of a cell boundary;
- solution at cell boundaries of the Riemann problem having the values $\mathbf{U}_{L,R}$ as initial data;
- calculation in each coordinate direction of the inter-cell flux $\mathbf{F^x}(\mathbf{U}_{p+1/2,q,r})$, $\mathbf{F^z}(\mathbf{U}_{p,q,r+1/2})$, that is the flux across the boundary between a cell (*e.g.* the p-th) and its closest neighbour [*e.g.* the (p+1)-th];
- check on the location of atmosphere and excised regions.

4.2.5 Calculation of the primitive variables from the conserved ones

An mentioned in Section (3.2), the equations of relativistic hydrodynamics are written in a flux conserved formulation. As a consequence not the usual primitive variables ρ, v^i, p are evolved, but rather the conserved variables D, S_i, τ. In the end the primitive variables are still needed to calculate the stress-energy tensor, the fluxes and the source terms and to evaluate the results of the simulation.
An algebraic transformation from the conserved variables to the primitive variables is not possible, except in certain special circumstances. One possible way is to is to solve the following implicit equation to get the new value of the pressure after a time-step:

$$p - \bar{p}[\rho(\mathbf{U}, p), \epsilon(\mathbf{U}, p)] \; = \; 0 \tag{4.23}$$

where *p* is the value of the pressure to be found and $\bar{p}[\rho(\mathbf{U}, p), \epsilon(\mathbf{U}, p)]$ is the pressure as obtained through the EoS in terms of the updated conserved variable **U** and of *p* itself. The expressions of ρ and ϵ in terms of the conserved variables and of the pressure are calculated by inverting equations (3.45):

$$\rho \; = \; \frac{D}{\tau + p + D}\sqrt{(\tau + p + D)^2 - S^2}, \tag{4.24}$$

$$\epsilon \; = \; D^{-1}\left(\sqrt{(\tau + p + D)^2} - p\frac{\tau + p + D}{\sqrt{(\tau + p + D)^2} - S^2}, -D\right), \tag{4.25}$$

where

$$S^2 \; = \; \gamma^{ij} S_i S_j, \tag{4.26}$$

In `Whisky2D` equation (4.23) is solved numerically by a iterative Newton Raphson root finder method. This method requires the derivatives of the functions of ρ and ϵ with respect to the dependent variable *p*,

$$\frac{d}{dp}\left\{p - \bar{p}[\rho(\mathbf{U}, p), \epsilon(\mathbf{U}, p)]\right\} \; = \; 1 - \frac{\partial \bar{p}(\rho, \epsilon)}{\partial \rho}\frac{\partial \rho}{\partial p} - \frac{\partial \bar{p}(\rho, \epsilon)}{\partial \epsilon}\frac{\partial \epsilon}{\partial p}, \tag{4.27}$$

where

$$\frac{\partial \rho}{\partial p} \; = \; \frac{DS^2}{\sqrt{(\tau + p + D^2)^2 - S^2}(\tau + p + D)^2} \tag{4.28}$$

$$\frac{\partial \epsilon}{\partial p} \; = \; \frac{pS^2}{\bar{\rho}((\tau + p + D^2)^2 - S^2)(\tau + p + D)} \tag{4.29}$$

and where $\partial\bar{p}/\partial\rho$ and $\partial\bar{p}/\partial\epsilon$ given by the EoS. Once the value of the pressure is known, the other values follow by analytic expressions. The polytropic EoS allows for a simpler way of converting

from the conservative to the primitive variables by solving another explicit equation for the rest mass density ρ:

$$\rho\tilde{W} - D \;=\; 0 \tag{4.30}$$

where the pressure, the specific internal energy and the enthalpy are computed from the EoS and the Lorentz factor is computed from the first equation of (3.45) as

$$\tilde{W} \;=\; \sqrt{1 + \frac{S^2}{(Dh)^2}}. \tag{4.31}$$

The only needed derivative of (4.30) is given by

$$\frac{d}{d\rho}(\rho\tilde{W} - D) \;=\; \tilde{W} - \frac{\rho S^2 h'}{\tilde{W} D^2 h^3}, \tag{4.32}$$

where

$$\begin{aligned} h' \;&=\; \frac{\partial h}{\partial \rho} \;=\; \frac{\partial}{\partial \rho}\,(1 + \epsilon + h) \;=\; \frac{\partial}{\partial \rho}\left[1 + \frac{p}{(\Gamma-1)\gamma} + \frac{p}{\rho}\right] \;=\; \frac{\partial}{\partial \rho}\left[1 + \frac{\Gamma p}{(\Gamma-1)p}\right] \\ &=\; \frac{\partial}{\partial \rho}\left[1 + \frac{\Gamma K \rho^{\Gamma}}{(\Gamma-1)\rho}\right] \;=\; \frac{\Gamma K \rho^{\Gamma}}{\rho^2} \;=\frac{\Gamma p}{\rho^2} \;=\; \frac{1}{\rho}\frac{\partial p}{\partial \rho}. \end{aligned} \tag{4.33}$$

4.2.6 Treatment of the atmosphere

Numerical methods for the solution that the hydrodynamics equations in Lagrangian formulation assume that the we computational domain is filled by a fluid, i.e. that all grid points refer to values of ρ, p and v which are non-zero. In most cases, however, we are interested in isolated objects , e.g. stars, disks, tori, so that part of the domain will referred to by vacuum regions. This is made more serious in general relativity, where one has to accommodate at the same time the need to resolve well objects that are intrinsically compact and the need to place the outer boundaries at very large distances from the compact object. As a results, over much of the domain that we evolve, the hydrodynamical variables ρ and p are, at least mathematically, supposed to be zero. However, in the vacuum limit the hydrodynamics equations break down, the speed of sound tends to the speed of light and HRSC schemes, that we recall use the characteristic structure of the equations, fail. So this region must be treated specifically. To avoid this problem we introduce a tenuous *atmosphere*, i.e. a low-density and low-pressure region surrounding the compact objects.

We treat the atmosphere as a perfect fluid having a pre-assigned value of the pressure and the density and a zero coordinate velocity. This approach is indeed used by all groups working on GRHD [38, 94]. The atmosphere is first specified by the initial data routines. Typically, the atmosphere values are set to be more than seven orders of magnitude smaller than the initial maximum ρ_{cent}. Before computing the fluxes, `Whisky 2D` checks whether the conserved variables D or τ are below some minimum value or whether an evolution step might push them below such a value. If this is the case, the relevant cell is not evolved and the hydrodynamical variables at that point are set to *atmosphere values* i.e.. The other stage where `Whisky 2D` checks about the location of the atmosphere is in the routine that converts from conserved variables to primitive variables. This is where the majority of the atmosphere points are usually reset. We call that at this stage in the work-flow. For points in the fluids an attempt is made to convert.
If the EoS is the polytropical and if the iterative algorithm returns a negative value of ρ, then ρ is reset

to the atmosphere value, the velocities are set to zero and p, ϵ, S^i and τ are reset to be consistent with ρ. If, on the other hand, the EoS is more general (such as an ideal-fluid one), then we check whether the specific internal energy ϵ is less than a specified minimum. If this is the case then we assume we are in the atmosphere and we apply the procedure that changes from the conserved to the primitive variables for the polytropic EoS, instead.

Note that the atmosphere values used for the calculation of the initial data and the ones used during the simulations need not be the same. Indeed, we typically set the initial atmosphere values to be two orders of magnitude smaller than the evolved ones to minimize initial truncation error problems leading to spurious low-density-matter waves across the atmosphere. With appropriate choices of the parameters regulating the atmosphere implementation, the evolution of the compact objects in our simulations is not affected by the atmosphere .

The treatment of the atmosphere of the `Whisky 2D` is very to the one above and which is used in the as described for the `Whisky` code. In addition we use a threshold value such that if the new envolved value of the density $\tilde{\rho}$ is $\rho_{thresh.}\tilde{\rho}\rho_{Cactus}$, then $\tilde{\rho} = \rho_{Cactus}$. This technique allows to resume small density numbers that could be guaranteed by the gravitational field of the star.
The simulations in this thesis using a threshold of $\rho_{jump} = \rho_{cent} \times 10^{-7}$ and for minimum density $\rho_{min} = \rho_{cent} \times 10^{-10}$.

Part IV

Isolated neutron stars

Chapter 5

Numerical evolution of neutron stars

A number of astrophysical scenarios possess and preserve an overall cylindrical symmetry also when undergoing a catastrophic and nonlinear evolution. Exploiting such a symmetry, these processes can be studied through numerical-relativity simulations at smaller computational costs and at considerably larger spatial resolutions. We here present first applications of the a new flux-conservative formulation of the relativistic hydrodynamics equations in cylindrical coordinates. By rearranging those terms in the equations which are the sources of the largest numerical errors, the new formulation yields a global truncation error which is one or more orders of magnitude smaller than those of alternative and commonly used formulations. We illustrate this through a series of numerical tests involving the evolution of oscillating spherical and rotating stars, as well as shock-tube tests.

In order to test the stability properties of the new formulation and compare its accuracy with the one of the formulation first presented in ref. [4] and then used, among others, in refs. [5, 8, 95, 96], we have implemented both of them in `Whisky2D`. In the following Sections we test them against well-known smooth solutions in curved but static space-times, or in curved and fully dynamical space-times, and, finally, against discontinuous solutions in flat space-times.
The initial data, in particular, have been produced as solution of the Einstein equations for axisymmetric and stationary stellar configurations [97], using the EOS (3.46) with $\Gamma = 2$ and polytropic constant $K = 100$, in order to produce stellar models that are, at least qualitatively, representative of what is expected from observations of neutron stars. Our attention has been restricted to two illustrative models representing a non-rotating star and a rapidly rotating star having equatorial and polar (coordinate) radii in a ratio $r_p/r_e = 0.67$. The relevant properties of these stellar models are reported in Table 5. All the numerical results presented hereafter have been obtained with the following fiducial numerical set-up: the reconstruction of the values at the boundaries of the computational cells is made using the PPM method [89], while the HLLE algorithm is used as an approximate Riemann solver [98]. The lapse function is evolved with the "$1 + \log$" slicing condition given by eq. (2.34), while the shift is evolved using a version of the hyperbolic $\tilde{\Gamma}$-driver condition (2.36) in which the advection terms for the variables β^i, B^i and $\tilde{\Gamma}^i$ are set to zero. The time evolution is made with a method-of-line approach [74] and a third-order Runge-Kutta integration scheme (our CFL factor is usually chosen between 0.3 and 0.5). A third-order Lagrangian interpolation is adopted to implement the *"cartoon"* method. For the matter variables we use "Dirichlet"boundary conditions (*i.e.,* the solution at the outer boundary is always kept to be the initial one), while for the field variables we adopt outgoing Sommerfeld boundary conditions.
We typically present results at four different resolutions: $\bar{h} = 0.4M$, $\bar{h}/2$, $\bar{h}/4$, $3\bar{h}/16$ and $\bar{h}/8$,

Table 5.1: Equilibrium properties of the initial stellar models. The different columns refer respectively to: the ratio of the polar to equatorial coordinate radii r_p/r_e, the central rest-mass density ρ_c, the gravitational mass M, the rest mass M_0, the circumferential equatorial radius R_e, the angular velocity Ω, the maximum angular velocity for a star of the same rest mass $\Omega_{\rm K}$, the ratio J/M^2 where J is the angular momentum, the ratio of rotational kinetic energy to gravitational binding energy $T/|W|$. All models have been computed with a polytropic EOS with $K = 100$ and $\Gamma = 2$.

	r_p/r_e	ρ_c $(\times 10^{-3})$	M $(M_\odot)$	M_0 $(M_\odot)$	R_e	Ω	Ω_K $(\times 10^{-2})$	J/M^2	$T/\|W\|$
A	1.00	1.28	1.400	1.506	9.586	0.000	3.987	0.000	0.000
B	0.67	1.28	1.651	1.786	12.042	0.253	3.108	0.594	0.081

which correspond to about 25, 50, 100, 133 and 200 points across the stellar radius, respectively. The computational domain extends to $20\,M$ both in the x and z directions, and a reflection symmetry is applied across the equatorial (*i.e.*, $z = 0$) plane. Finally, we remark that in contrast with the interesting analysis of [99], we could not find signs of numerical instabilities when using the above numerical prescriptions for either of the two formulations considered.

5.1 Oscillating Neutron stars: fixed space-time

The first set of tests we discuss has been carried out by simulating relativistic polytropic stars in equilibrium and in a fixed space-time (*i.e.* in the Cowling approximation). In this case the Einstein equations are not evolved and the truncation error is in general smaller because it is produced uniquely from the evolution of the hydrodynamics equations.

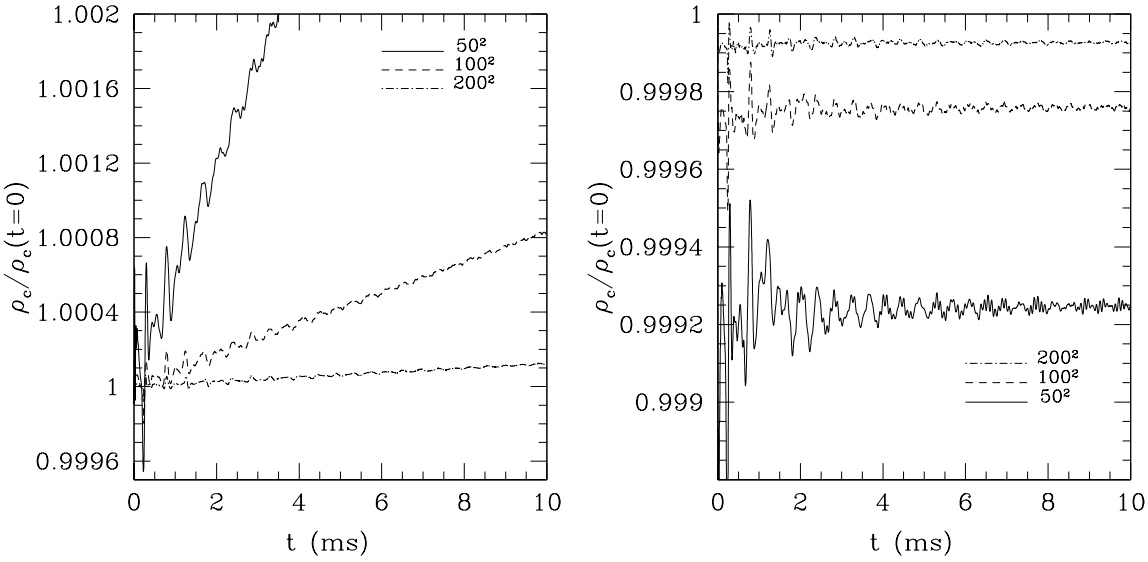

Figure 5.1: Evolution of the central rest-mass density for rapidly rotating stars (model B in Table 5) evolved within the Cowling approximation. The left panel refers to the use of the standard formulation, while the right one to the new formulation. Note the different scales in the two panels and note that in both cases the amplitude of the oscillations decreases with increasing resolution, while keeping the same phase.

Although the stars are in equilibrium, oscillations are triggered by the first-order truncation error at the center and the surface of the star (our hydrodynamical evolution schemes are only first order at local extrema). Both the amplitude of the oscillations and the rate of the secular change in their amplitude converge to zero at nearly second order with increasing grid resolution [38,90]. The genuine dynamics produced by the truncation error can then be studied either when the space-time is held fixed (*i.e.,* in the Cowling approximation) or when the space-time is evolved through the solution of the Einstein equations. This is shown in figure 5.1, which reports the evolution of the central rest-mass density for rapidly rotating stars (model B in Table 5) evolved within the Cowling approximation. The left panel refers to the standard formulation, while the right one to the new formulation. Note that in both cases the amplitude of the oscillations decreases at roughly second order with increasing resolution, while keeping the same phase. This is a clear signature that the oscillations corresponds to proper eigenmodes of the simulated star. However, the difference of the secular evolution between the standard formulation and the new one is rather remarkable. The latter, in fact, is much more accurate and the well-known secular increase in the central density is essentially absent in the new formulation. Quantities that are particularly useful to assess the accuracy of the two formulations are the rest mass and the angular momentum which we compute as [46]

$$M_0 = 2\pi \int_{V_*} \sqrt{\gamma}\rho W x \, dx \, dz \,, \tag{5.1}$$

$$J_z \;=\; 2\pi \, \epsilon^k_{zj} \int_V \left(\frac{1}{8\pi} \tilde{A}^j_k + x^j S_k + \frac{1}{12\pi} x^j K_{,k} - \frac{1}{16\pi} x^j \tilde{\gamma}^{lm}_{,k} \tilde{A}_{lm} \right) e^{6\Phi} x \, dx \, dz \,, \tag{5.2}$$

where V_* is the coordinate volume occupied by the star and V is coordinate volume of the computational domain.

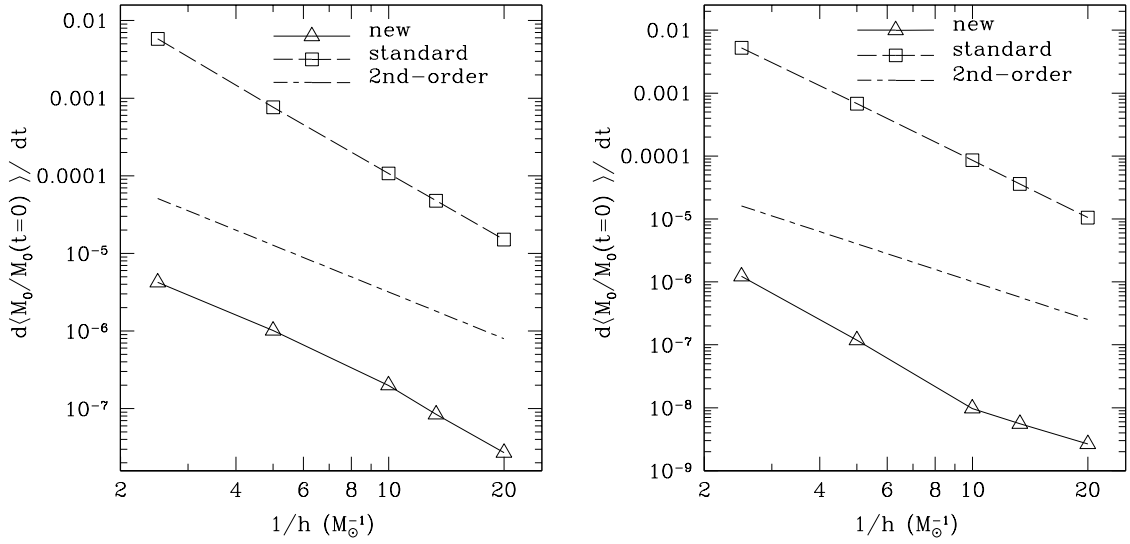

Figure 5.2: Time derivative of the average of the rest mass M_0, normalized to the initial value $M_0(t=0)$, for evolutions in a fixed space-time (Cowling approximation). The average $\mathrm{d}\langle M_0/M_0(t=0)\rangle/\mathrm{d}t$ is computed between the initial value and a time $t = 25\,\mathrm{ms}$, corresponding to about 30 oscillations. The left panel refers to a non-rotating star (model A in Table 5), while the right panel to a rapidly rotating star (model B in Table 5). Indicated with squares are the numerical values obtained with the standard formulation of the hydrodynamics equations, while triangles are used for the new one. Also indicated with a dot-dashed line is the slope for a second-order convergence rate.

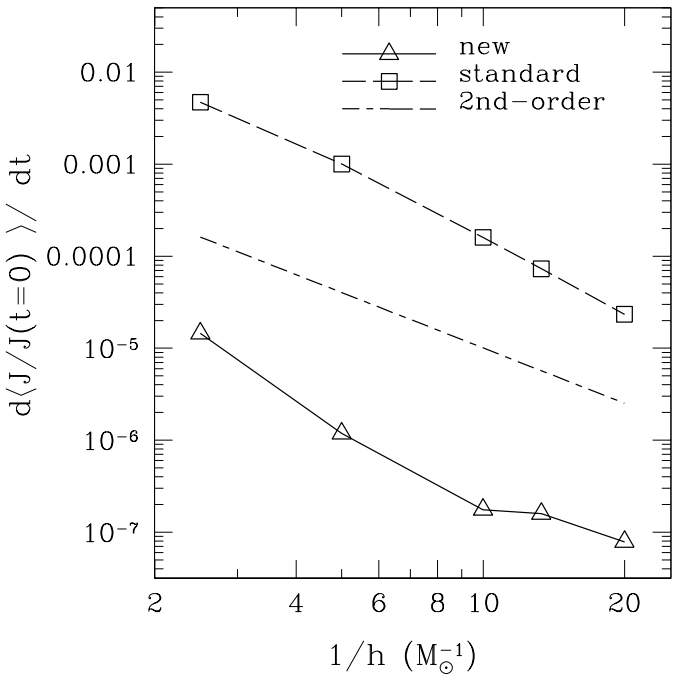

Figure 5.3: Time derivative of average of the angular momentum normalized to the initial value $\mathrm{d}\langle J/J(t=0)\rangle/\mathrm{d}t$ (*cf.*, figure 5.2) for a rapidly rotating star (model B of Table 5). Indicated with squares are the numerical values obtained with the standard formulation of the hydrodynamics equations, while triangles are used for the new one; a dot-dashed line is the slope for a second-order convergence rate.

Figure 5.2 shows the dependence on the inverse of the resolution of the error in the conservation of the rest mass for a non-rotating model as computed in the Cowling approximation (left panel) or in a fully dynamical simulation (right panel). Since the evolution of the rest mass shows, in addition to a secular evolution, small oscillations (*i.e.*, of $\sim 3\times 10^{-9}$ for the highest resolution and of $\sim 3\times 10^{-6}$ for the lowest resolution) the calculation of the rest mass at a given time can be somewhat ambiguous. To tackle this problem and to avoid the measurement to be spoiled by the oscillations, we perform a linear fit of the evolution of M_0, normalized to the initial value $M_0(t=0)$, between the initial value and a time $t = 25\,\mathrm{ms}$ (corresponding to about 30 oscillations) and we take as the time derivative of the mass the coefficient of the linear fit: $\mathrm{d}\langle M_0/M_0(t=0)\rangle/\mathrm{d}t$. Figure 5.2, in particular, reports in a logarithmic scale $\mathrm{d}\langle M_0/M_0(t=0)\rangle/\mathrm{d}t$ as a function of the inverse of the resolution h. Indicated with squares are the numerical values obtained with the standard formulation of the hydrodynamics equations, while triangles are used for the new one. Also indicated with a long-short-dashed line is the slope for a second-order convergence rate.

Note that although we use a third-order method for the reconstruction (namely, PPM), we do not expect third-order convergence. This is also due to the fact that the reconstruction schemes are only first-order accurate at local extrema (*i.e.* at the centre and at the surface of the star), thus increasing the overall truncation error. Similar estimates were obtained also using the `Whisky` code in 3D Cartesian coordinates [91, 100].

Clearly both the new and the standard methods provide a convergence rate which is close to two. However, and this is the most important result of this work, the new method yields a truncation error which is several orders of magnitude smaller than the old one. More specifically, in the case of the

rest mass, the conservation is more accurate of about four orders of magnitude. We believe that this is essentially due to the rewriting of the source terms in the flux-conservative formulation which in the new formulation does not have any coordinate-singular term (*i.e.* $\propto 1/x$).
Note also that, because the new formulation is intrinsically more accurate, it also suffers more easily from the contamination of errors which are not directly related to the finite-difference operators. [The one made in the calculation of the integral (5.2) is a relevant example but it is not the only one]. This may be the reason why, in general, at lower resolutions the new formulation has convergence rate which is not exactly two and appears over-convergent (see right panel of figure 5.2). However, as the resolution is increased and the finite-difference errors become the dominant ones, a clearer trend in the convergence rate is recovered.
Another way of measuring the accuracy of the two formulations is via the comparison of the evolution of the angular momentum. While this quantity is conserved to machine precision in the case of a non-rotating star, this does not happen for rotating stars and the error can be of a few percent in the case of very low resolution and of a very rapidly rotating star. This is shown in figure 5.3 for the stellar model B of Table 5 and it reports in a logarithmic scale the time derivative of the average of the angular momentum J normalized to the initial value $J(t=0)$. In analogy with figure 5.2, in order to remove the small-scale oscillations we first perform a linear fit of the evolution of J between the initial value and a time $t = 25\,\mathrm{ms}$ and take the coefficient of the fit as the time derivative of the angular momentum: $\mathrm{d}\langle J/J(t=0)\rangle/\mathrm{d}t$. Indicated with squares are the numerical values obtained with the standard formulation of the hydrodynamics equations, while triangles are used for the new one; a dot-dashed line shows the slope for a second-order convergence rate.
It is simple to recognize from figure 5.3 that also for the angular momentum conservation the new formulation yields a truncation error which is two or more orders of magnitude smaller, with a clear second-order convergence being recovered at sufficiently high resolution.

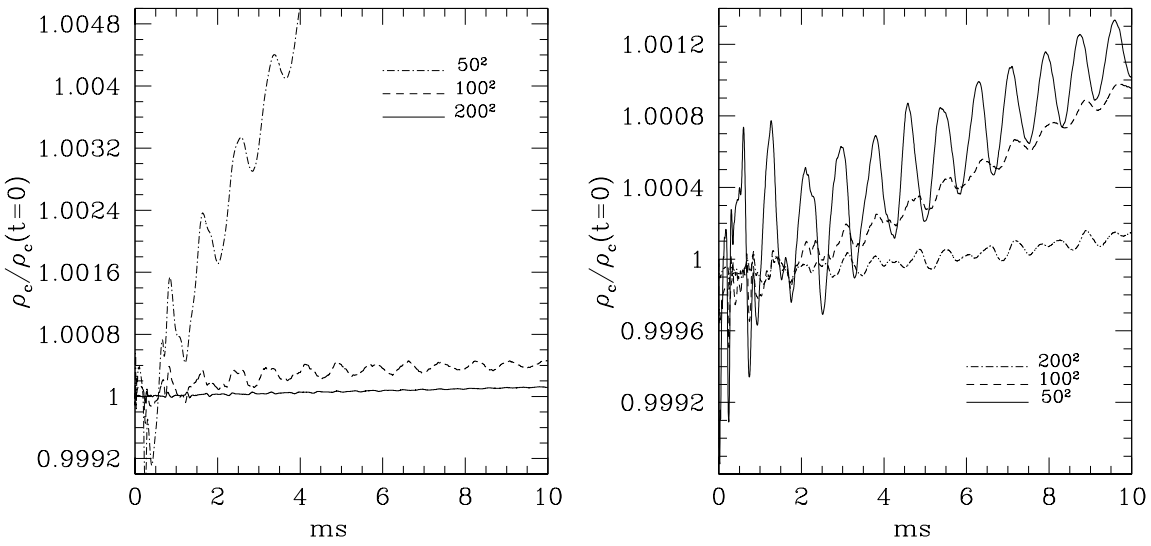

Figure 5.4: The same as in figure 5.1 but for a full-space-time evolution. The left panel refers to the standard formulation, while the right one to the new formulation. Note the different scale between the two panels.

5.2 Oscillating Neutron stars: dynamical space-time

Also the second set of tests we discuss is based on the evolution of relativistic polytropic stars in equilibrium, but now the evolution is performed in a dynamical space-time, thus with the coupling of Einstein and hydrodynamics equations. The truncation error in this case is given by the truncation error coming from the solution of both the field equations and the hydrodynamics equations. The results of our calculations are summarised in figures 5.4–5.6, which represent the equivalents of figures 5.1–5.3 for full-space-time evolutions. Because the results are self-explanatory and qualitatively similar to the ones discussed for the evolutions with fixed space-times, we will comment on them only briefly.

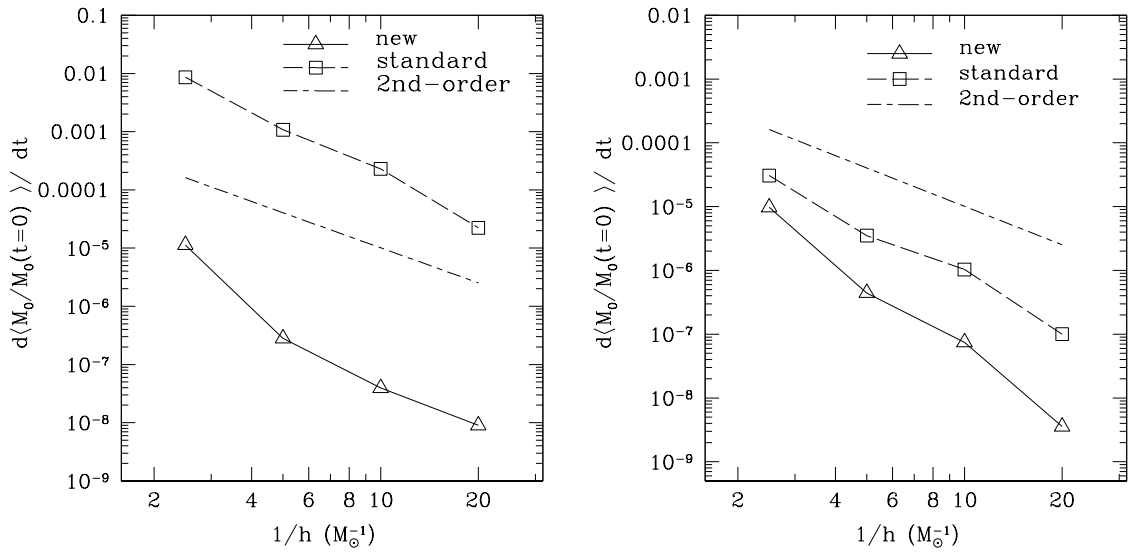

Figure 5.5: The same as in figure 5.2, but for full-space-time evolutions. The left panel refers to a non-rotating star (model A in Table 5), while the right panel to a rapidly rotating star (model B in Table 5).

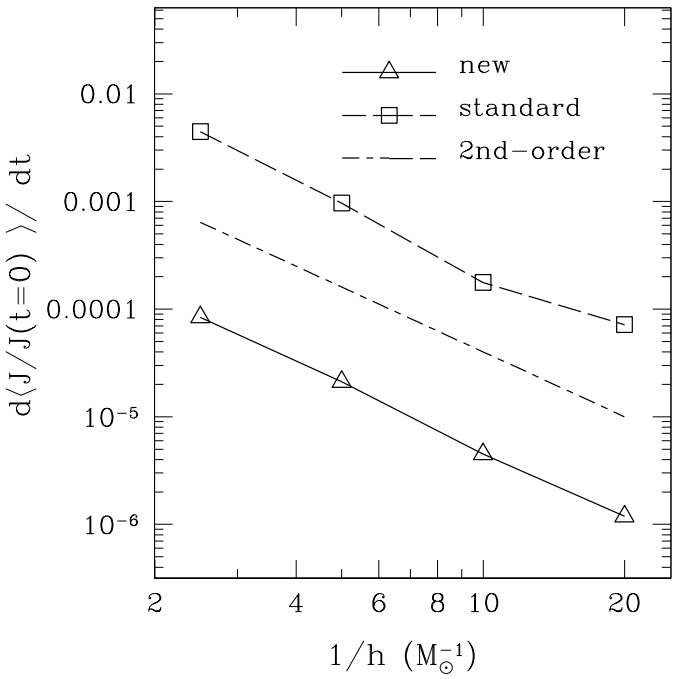

Figure 5.6: The same as figure 5.3 but for a rapidly rotating star evolved in a dynamical space-time.

In particular, figures 5.5–5.6 highlight that while the overall truncation error in dynamical space-times is essentially unchanged for the standard formulation, it has increased in the case of the new formulation. This is particularly evident at very low resolutions, where the new formulation seems to be hyper-convergent. However, despite a truncation error which is larger than the one for fixed space-times, the figures also indicate that the new formulation does represent a considerable improvement over the standard one and that its truncation error is at least two orders of magnitude smaller. Most importantly, the conservation properties of the numerical scheme have greatly improved and the secular increase in the rest mass, is also considerably suppressed. This is clearly shown in figures 5.4, where the secular increase is suppressed almost quadratically with resolution. More precisely, for both approaches the growth rate of the central rest-mass density for the coarse resolution is ~ 12 times larger than the corresponding one for the high resolution. However, at the highest resolution, the growth rate for the standard formulation is ~ 10 times larger than the one of the new formulation.

5.3 Calculation of the eigenfrequencies

As mentioned in the previous Section, although in equilibrium, the simulated stars undergo oscillations which are triggered by the nonzero truncation error. It is possible to consider these oscillations not as a numerical nuisance, on the contrary it is possible to exploit them to perform a check on the consistency of a full nonlinear evolution with a small perturbation (the truncation error) with the predictions of perturbation theory [38, 90]. Furthermore, when used in conjunction with highly accurate codes, these oscillations can provide important information on the stellar oscillations within regimes, such as those of very rapid or differential rotation, which are not yet accessible via perturbative calculations [101].

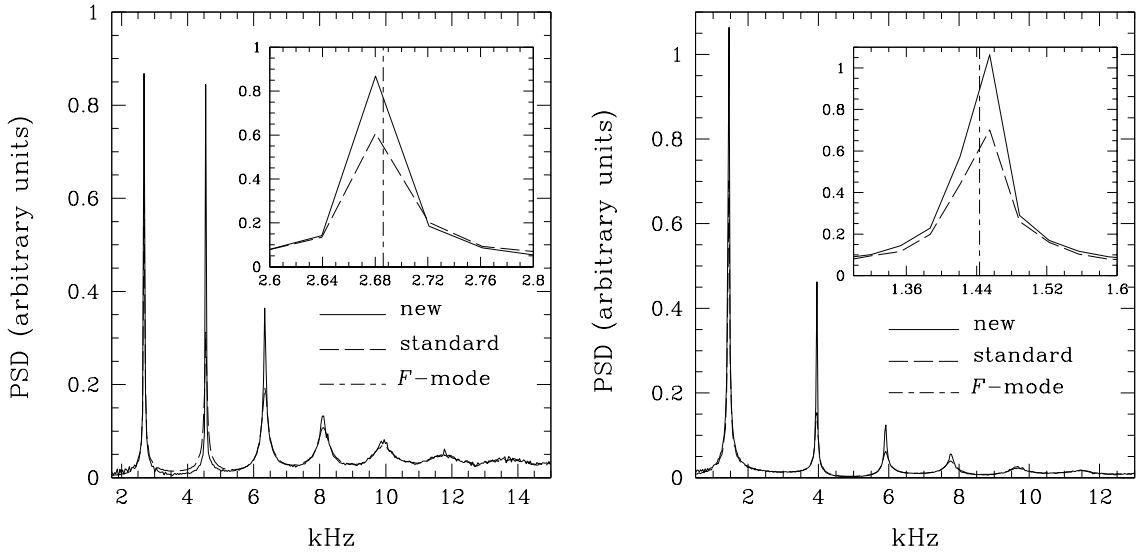

Figure 5.7: Power spectral density (in arbitrary units) of the maximum rest-mass density evolution in the new and standard formulation (solid and dashed lines, respectively). The simulations are relative to a non-rotating star (model A in Table 5) with left left panel referring to an evolution with a fixed space-time and the right one to an evolution with a dynamical space-time. The spectra are calculated from the simulations at the highest resolution and cover $25\,\mathrm{ms}$ of evolution. For both panels the insets show a magnification of the spectra near the F-mode and the comparison with the perturbative estimate as calculated with the numerical code described in ref. [102].

In this Section we use such oscillations, and in particular the fundamental $\ell = 0$ quasi-radial F-mode, to compare the accuracy of the two formulations against the perturbative predictions. This is summarised in figure 5.7 which reports the power spectral density (in arbitrary units) of the maximum rest-mass density evolution (*cf.*, figures 5.1 and 5.3) in the new and standard formulation (solid and dashed lines, respectively). The simulations are relative to a non-rotating star (model A in Table 5) with the left panel referring to an evolution with a fixed space-time, while the right one to an evolution with a dynamical space-time. The specific spectra shown are calculated from the simulations at the highest resolution and cover an interval of $25\,\mathrm{ms}$. It is quite apparent that the two formulations yield spectra which are extremely similar, with a prominent F-mode at about $2.7\,\mathrm{kHz}$ and $1.4\,\mathrm{kHz}$ for the fixed and dynamical space-time evolutions, respectively. The spectra also show the expected quasi-radial overtones at roughly multiple integers of the F-mode, the first of which has a comparable power in the case of Cowling evolution, while it is reduced of about 50% in the full space-time evolution. Indeed, the spectra in the two formulations are so similar that it is necessary to concentrate on the features of the F-mode to appreciate the small differences. These are shown in the insets of the two panels which report, besides a magnification of the spectra near the F-mode, also the perturbative estimate F_{pert}, as calculated with the perturbative code described in ref. [102].

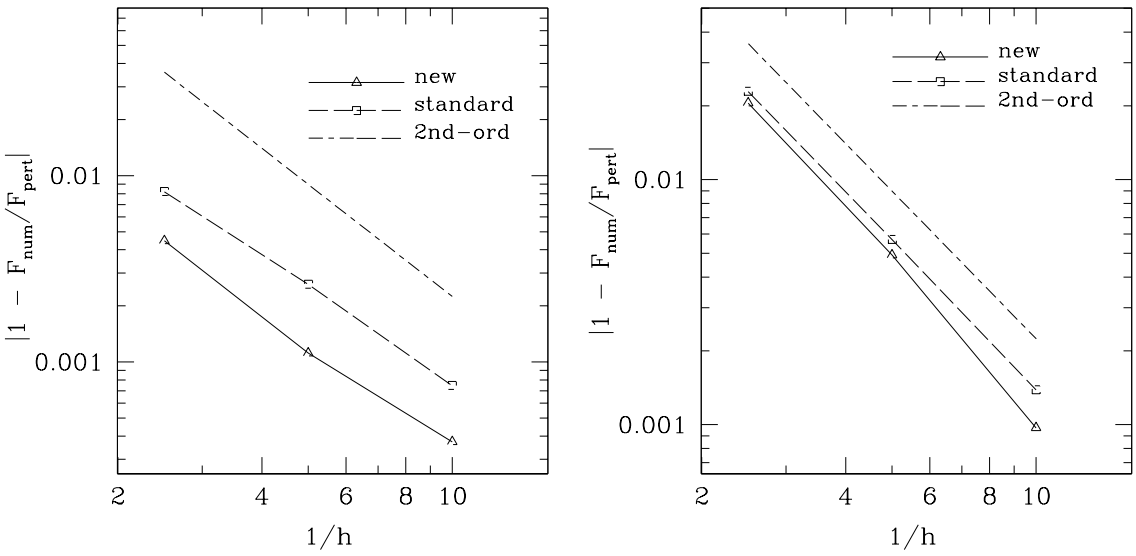

Figure 5.8: Relative difference between the numerical and perturbative eigenfrequencies of the F-mode for the two formulations (solid lines for the new one and dashed lines for the standard one). The differences are computed for different resolutions and refer to the non-rotating model A of Table 5 when evolved in a fixed space-time (left panel) and in a dynamical one (right panel). Indicated with a dot-dashed line is the slope for a second-order convergence rate.

To provide a more quantitative assessment of the accuracy with which the two formulations reproduce the perturbative result we have computed the eigenfrequency of the F-mode, which we indicate as $F_{\rm num}$, by performing a Lorentzian fit to the power spectrum with a window of 0.2 kHz. We remark that it is essential to make use of a Lorentzian function for the fit as this reflects the expected functional behaviour and increases the accuracy of the fit significantly. Shown in figure 5.8 is the absolute value of the relative difference between the numerical and perturbative eigenfrequencies of the F-mode, $|1-F_{\rm num}/F_{\rm pert}|$ for the two formulations (solid lines for the new one and dashed lines for the standard one). The differences are computed for different resolutions with $\bar{h} = 0.4M$, $\bar{h}/2$ and $\bar{h}/4$ and refer to the non-rotating mode A of Table 5 when evolved in a fixed space-time (left panel) and in a dynamical one (right panel). Indicated with a dot-dashed line is the slope for a second-order convergence rate. This helps to see that both formulations yield an almost second-order convergent measure of the eigenfrequencies of the F-mode, with the new formulation having a truncation error which is always smaller than the one coming from the standard formulation. Given the importance of an accurate measurement of the eigenfrequencies to study the mode properties of compact stars, we believe that figures 5.7 and 5.8 provide an additional evidence of the advantages of the new formulation.
Finally, we note that a behaviour similar to the one shown in figures 5.7– 5.8 has been found also for rotating stars although in this case the comparison is possible only for evolutions within the Cowling approximation since we lack a precise perturbative estimate of the eigenfrequency for model B of Table 5 for a dynamical space-time.

5.4 Cylindrical Shock Reflection

One of the most important properties of HRSC schemes is their capability of handling the formation of discontinuities, such as shocks, which are often present and play an important role in many astrophysical scenarios. Tests involving shocks formation are usually quite demanding and codes that are not flux-conservative can also show numerical instabilities or difficulties in converging to the exact solution of the problem. Since both the new and the standard formulation solve the relativistic hydrodynamics equations as written in a flux-conservative form, they are both expected to be able to correctly resolve the formation of shocks, although each with its own truncation error. In the following test we consider one of such discontinuous flows and show that the new formulation provides a higher accuracy with respect to the standard one, stressing once again the importance of the definition of the conserved variables.

More specifically, we consider a one-dimensional test, first proposed by [103], describing the reflection of a shock wave in cylindrical coordinates. The initial data consist of a pressureless gas with uniform density $\rho_0 = 1.0$, radial velocity $v_0^x = -0.999898$, corresponding to an initial Lorentz factor $W_0 = 70.0$ and an internal energy which is taken to be small and proportional to the initial Lorentz factor, *i.e.*, $\epsilon = 10^{-5}(W_0)$. During the evolution an ideal-fluid EOS (3.48) is used with a fixed adiabatic index $\Gamma = 4/3$. The symmetry condition at $x = 0$ produces a compression and generates an outgoing shock in the radial direction. The analytic solution for the values of pressure, density, gas and shock velocities are given in [103]. From them one can determine the position $x_{\rm s}$ of the shock front at any time $\bar{t}$

$$x_{\rm s} \;=\; \frac{(\Gamma-1)W_0|v_0^x|}{W_0+1}\bar{t}\,. \tag{5.3}$$

This can then be used to compare the accuracy of the two formulations.

In the left panel of figures 5.9 we show the value of the radial component of the velocity v_x as a function of x at a time $\bar{t} = 0.002262\,\mathrm{ms}$ and for a resolution of $h/M_\odot = 6.25 \times 10^{-5}$. The solid line represent the analytic solution, the short-dashed line the numerical solution computed with the new formulation and the long-dashed line the one obtained with the standard formulation. As it is evident from the inset, the position of the shock is very well captured by both formulations, but the new one is closer to the exact one at this time.

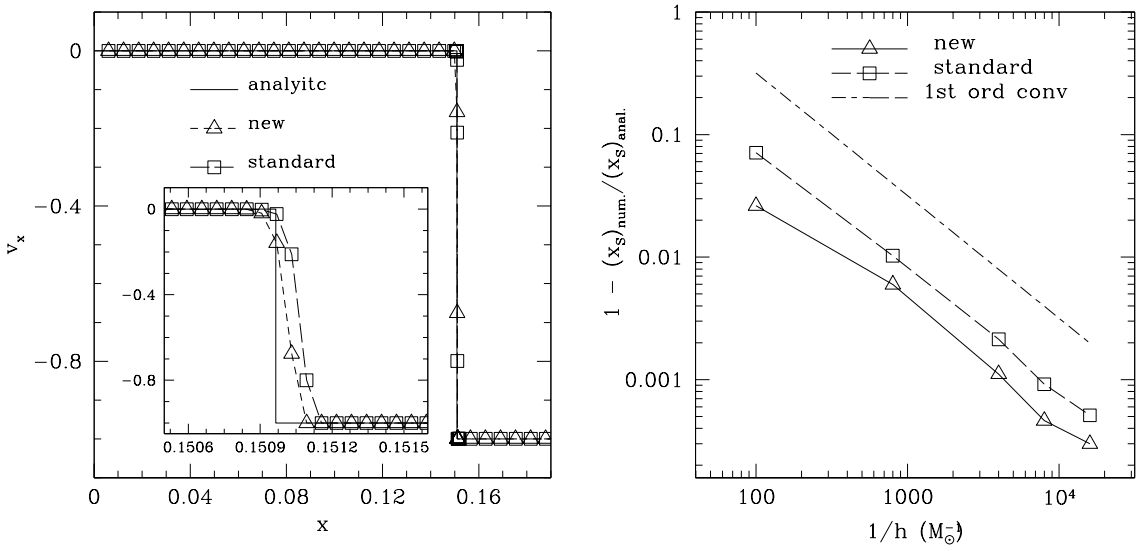

Figure 5.9: *Left panel:* Comparison of the velocity profiles for the two formulations in the solution of the axisymmetric shock-tube test with a resolution of $h = 6.25 \times 10^{-5}\, M_\odot$ The solid line shows the exact position after a time $\bar{t} = 0.002262\,\mathrm{ms}$, while the short-dashed and the long-dashed lines represent the solutions with the new and the standard formulations, respectively. *Right panel:* Comparison of the error in the determination of the position of the shock in the two formulations. Note the first-order convergence rate as expected for discontinuous flows.

To compare with the exact prediction given by expression (5.3), we compute the numerical position of the shock as the middle of the region where the value of the velocity moves from the pre-shock value v_x^+ to the post-shock one v_x^- (in practice, we fit a straight line between the last point of the constant post-shock state and the first point of the constant pre-shock state and evaluate the position at which this function has value $(v_x^+ + v_x^-)/2$.). The right panel of figure 5.9, shows the relative error $1 - (x_\mathrm{S})_\mathrm{num}/(x_\mathrm{S})_\mathrm{anal}$ in the position of the shock at time $\bar{t} = 0.002622\,\mathrm{ms}$ and for five different resolutions: $\bar{h} = 0.01\, M_\odot$, $\bar{h}/8$, $\bar{h}/40$, $\bar{h}/80$ and $\bar{h}/160$. Indicated with a dashed line is the error computed when using the standard formulation, while indicated with a solid line is the error coming from the new formulation. Note that both formulations show a first-order convergence, as expected for HRSC schemes in the presence of a discontinuous flow, but, as for the other tests, also in this case the new formulation has a smaller truncation error. A similar behaviour is shown also by other quantities in this test but these are not reported here.

It is useful to note that the difference between the two formulations in this test is smaller than in the previous ones, being of a factor of a few only and not of orders of magnitude. We believe this is due in great part to the fact that, in contrast with what happens for stars, the solution in the most troublesome part of the numerical domain (*i.e.* near $x \sim 0$, $z \sim 0$) is not characterized by particularly large values of the fields or of the fluid variables. In support of this conjecture is the evidence that at earlier times, when the shock is closer to the axis, both the absolute errors and the difference between the two formulations are larger.

Part V

Critical phenomena and gravitational collapse

Chapter 6

Critical phenomena and gravitational collapse

6.1 Critical phenomena in gravitational collapse

In what follows we give a brief overview of critical phenomena in gravitational collapse and which will be useful to cast our results in the more general context of critical phenomena in general relativity. We refer the interested reader to [11] for a more systematic presentation.

6.1.1 Self-similarity

Before dwelling on critical phenomena and because self-similarity plays a central role in this context, it is useful to recall briefly the definitions of "continuous" self-similarity and "discrete" self-similarity. We refer the interested reader to [104] for a more detailed discussion. We recall that a spacetime is said to be continuously self-similar if there exist a vector field, ξ^μ such that $\nabla_{(\mu}\xi_{\nu)} = g_{\mu\nu}$. Vector fields satisfying this condition are said to be "homothetic" as we can easily construct a one-parameter group of transformations, $\phi_s \colon x^\mu \mapsto y^\mu(s)$, where $y^\mu(s)$ is the integral curve associated with ξ^μ passing through x^μ. It is then easy to see that ϕ_s is an homothetic transformation as the associated push-forward, acts as a rescaling on the metric

$$\phi_s^* g_{\mu\nu} = e^{2s} g_{\mu\nu} \,. \tag{6.1}$$

For this reason in a system of coordinates adapted to the self-similarity

$$\xi^\mu = -\left(\frac{\partial}{\partial\tau}\right)^\mu , \tag{6.2}$$

the metric coefficients read

$$g_{\mu\nu}(\tau, x^i) = e^{-2\tau}\tilde{g}_{\mu\nu}(x^i) \,, \tag{6.3}$$

and the new metric $\tilde{g}_{\mu\nu}$ appears explicitly self-similar, *i.e.* independent of the τ.
Similarly, a spacetime is said to be "discretely self-similar" (DSS) if a discrete version of (6.1) holds. In particular, in ref. [22] Gundlach defines a spacetime to be DSS if there exist a diffeomorphism ϕ and a real constant Δ such that for any positive integer n

$$(\phi^*)^n g_{\mu\nu} = e^{2n\Delta} g_{\mu\nu} \,. \tag{6.4}$$

In coordinates adapted to the self-similarity a point P with coordinates (τ, x^i) is mapped by ϕ into $(\tau - \Delta, x^i)$ and the metric can be written as

$$g_{\mu\nu}(\tau, x^i) = e^{-2\tau} \tilde{g}_{\mu\nu}(\tau, x^i)\,, \tag{6.5}$$

where

$$\tilde{g}_{\mu\nu}(\tau + \Delta, x^i) = \tilde{g}_{\mu\nu}(\tau, x^i)\,. \tag{6.6}$$

Thus, if $\nabla^\mu \tau$ is time-like and induces a Cauchy foliation of the spacetime, we can give a physical interpretation of the dynamics of DSS solutions as a combined effect of a rescaling and a periodic "echoing" of the geometry.

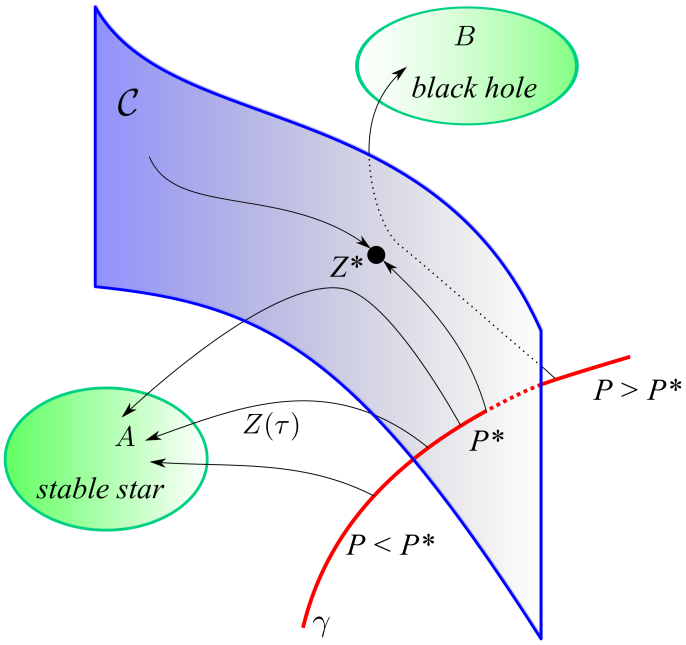

Figure 6.1: Phase space picture of type-II critical phenomena. The surface $\mathcal{C}$ represents the critical manifold, separating the basins of attraction of A and B. The line γ represents a generic one-parameter family of initial data intersecting the critical manifold in $P^\star$. Generic initial data starting at $Z(0)$ will evolve towards A or B following the arrows $Z(\tau)$, data near the threshold will be marginally attracted towards the critical solution $Z^\star$. Points exactly on the critical manifold will be attracted to the critical solution.

6.1.2 The basic concepts

Let us consider a group of one-parameter families of solutions, $\mathcal{S}[P]$, of the Einstein equations such that for every $P > P^\star$, $\mathcal{S}[P]$ contains a black hole and for every $P < P^\star$, $\mathcal{S}[P]$ is a solution not containing singularities. We say that these families exhibit a critical phenomenon if they have the common property that, as P approaches $P^\star$, $\mathcal{S}[P]$ approaches a universal solution $\mathcal{S}[P^\star]$, *i.e.* not depending on the particular family of initial data, and that all the physical quantities of $\mathcal{S}[P]$ depend only on $|P - P^\star|$. In analogy with critical phase transitions in statistical mechanics, these phenomena

are then classified as type-II or type-I critical phenomena [11]. In what follows we briefly recall the differences between the two classes.

a) Type-II critical phenomena. Type-II critical phenomena involve the existence of a CSS or DSS solutions sitting at the threshold of black-hole formation. They are characterized by the mass-scaling relation:

$$M_{\rm BH} = c|P - P^\star|^\gamma \,, \tag{6.7}$$

where γ is independent upon the particular choice of the initial data. The nomenclature "type-II" comes from the analogous type-II phase transitions in statistical mechanics, which are characterized by scale invariance of the thermodynamical quantities [11].
These phenomena are usually interpreted in terms of attractors in an infinite-dimensional phase space, but we will here present a qualitative picture which can be useful to fix the ideas (see also the review in [11]). A more rigorous study employing the renormalization group formalism can be found instead in [13].
Let us consider general relativity as an infinite dimensional dynamical system in an abstract phase space in which extra gauge freedoms have been eliminated so that each point, Z, can be thought as an initial data-set for the Einstein equations and the associated time development as a line in this space: $t \mapsto Z(t)$. We suppose to have chosen a slicing adapted to the self-similarity of the critical solution so that it appears as a fixed point, $Z^\star$, in the CSS case or a closed orbit for the DSS case (see [11] for a more in-depth discussion of the consequences of these assumptions).
In the case of CSS solutions, the main features of this phase space are the presence of two attractive sets: A and B representing regular solutions without singularities and black-hole solutions. Their basins of attractions are separated by a manifold, $\mathcal{C}$, called *critical manifold* on which there is an attractor of Co-dimension one: the critical solution, $Z^\star$; this is shown schematically in figure 6.1. Any generic one-parameter family of initial data can then be thought as a 1-dimensional line intersecting the critical manifold in one point. Initial data with $P < P^\star$, will develop as regular solutions not containing singularities and will therefore fall in the basin of attraction containing the so called *subcritical solutions* (*cf.*set A in figure 6.1). Conversely, solutions with $P > P^\star$ will undergo gravitational collapse with the formation of a black hole, thus falling in the basin of attraction containing the so called *supercritical solutions* (*cf.*set B in figure 6.1).
The key point here is that the critical solution is attractive on the critical manifold. Stated differently, nearly-critical solutions will experience "funneling" effects as all but one mode converge towards $Z^\star$. If $P \approx P^\star$, then the unstable mode, *i.e.* the mode "perpendicular" to $\mathcal{C}$, will be small until later in the evolution, thus allowing for the observation of nearly-critical solutions. In this case, all but one mode of the solution are "washed out" by the interaction with the critical solution, thus explaining both the universality of the solution and the mass-scaling relation.

b) Type-I critical phenomena. Type-I critical phenomena are the ones in which the black hole formation turns on at finite mass and the critical solution presents a non-self-similar stationary or periodic solution configuration. The scaling quantity here is the lifetime of the metastable solution

$$t_p = -\frac{1}{\lambda} \ln |P - P^\star| + \text{const} \,, \tag{6.8}$$

where λ does not depend on the initial data. This scaling can be justified using simple arguments similar to the ones presented in [11] for the mass scaling in the type-II case.

6.2 Thermodynamics of the critical solution

As mentioned in the introduction of this chapter, there is a relation between the nature of the critical phenomena in GR and the phase-transitions in statistical physic. This paragraph will come up with a qualitative relation between both phenomena.

6.2.1 Entropy of the critical solution

A convenient way to study the properties of the critical solution is to characterize its thermodynamical properties and in particular its entropy. The basic idea is that the metastable (critical) solution is simply an equilibrium solution on the unstable branch of TOV configurations and thus that by measuring its entropy it is possible to relate it to the corresponding equilibrium polytropic model. Following [105], we express the second law of thermodynamics as

$$S \,=\, S_0 \,+\, C_{\rm V}\ \ln(T) \,-\, R\ \ln(\rho), \tag{6.9}$$

where S_0 is an integration constant that we set to zero and where

$$C_{\rm V} \,=\, \left(\frac{d\epsilon}{dT}\right)_{\rm v} \tag{6.10}$$

is the specific heat capacity at constant pressure. and R the gas constant. In the case of an ideal gas R is related to the specific heat capacities through the relation

$$R \,=\, C_{\rm p} \,-\, C_{\rm V} \,=\, \left(\frac{dh}{dT}\right)_{\rm p} - \left(\frac{d\epsilon}{dT}\right)_{\rm v}, \tag{6.11}$$

where $h = 1 + \epsilon + p/\rho$ is the specific enthalpy. Recalling that $\epsilon = C_{\rm V} T$ and $\Gamma = C_{\rm p}/C_{\rm V}$, the second law of thermodynamics (6.9) for a polytropic EOS is simply given by

$$S \,=\, C_{\rm V}\ \ln\left(\frac{K}{C_{\rm V}(\Gamma-1)}\right), \tag{6.12}$$

or equivalently

$$K \,=\, R\ \exp\left(\frac{S}{C_{\rm V}}\right). \tag{6.13}$$

Stated differently, the polytropic constant reflects all of the changes in the entropy of the system, so that expression (6.13) allows a simple connection between the entropy of the critical solution, which we measure as proportional to $K = p/\rho^{\Gamma}$, and the properties of a corresponding equilibrium TOV model.
In practice the polytropic constant can change enormously across the star especially after the collision and since we are interested only in global quantities we use a volume-averaged polytropic constant

$$\langle K \rangle \,=\, \frac{\int_\Omega p/\rho^\Gamma dV}{\int_\Omega dV}, \tag{6.14}$$

and perform the volume integration not across the whole star but over a volume Ω where the rest-mass density is larger than 10% of the initial central one. This choice removes the difficulties with possible divergences near the stellar surface and we have verified that is robust against different values of the threshold density.

Chapter 7

Critical phenomena in neutron stars: Linearly unstable non-rotating models

7.1 Numerical setup

In what follows we briefly describe the numerical setup used in the simulations and the procedure followed in the construction of the initial data. In essence, we use the `Whisky2D` code described in detail in [9] and based on the 3-dimensional code `Whisky` [100, 106, 107], to solve numerically and in 2 spatial dimensions the full set of Einstein equations

$$G_{\mu\nu} = 8\pi T_{\mu\nu}\,, \tag{7.1}$$

where $G_{\mu\nu}$ is the Einstein tensor and $T_{\mu\nu}$ is the stress-energy tensor. More specifically, we evolve a conformal-traceless "$3+1$" formulation of the Einstein equations as presented in [41], in which the spacetime is decomposed into 3D space-like slices, described by a metric γ_{ij}, its embedding in the full spacetime, specified by the extrinsic curvature K_{ij}, and the gauge functions α (lapse) and β^i (shift), which specify a coordinate frame. Axisymmetry is imposed using the "cartoon" technique [108] and the equation are solved using finite differencing of order three. The chosen slicing condition is the popular "$1+\log$" while the chosen spatial-gauge is the Gamma-freezing one. The field equations for the three-metric γ_{ij} and the second fundamental form K_{ij} are coupled with the equations of motion of general relativistic hydrodynamics

$$\nabla_\mu(\rho u^\mu) = 0\,, \qquad \nabla_\nu T^{\mu\nu} = 0\,, \tag{7.2}$$

where ρ is the (rest) baryonic mass density, u^μ is the four-velocity of the fluid and $T^{\mu\nu}$ is the stress-energy tensor of a perfect fluid

$$T^\mu{}_\nu = \rho H u^\mu u_\nu + p\delta^\mu{}_\nu\,. \tag{7.3}$$

Here, $H \equiv 1+\epsilon+p/\rho$ is the specific enthalpy, p is the pressure, $\delta^\mu{}_\nu$ is the Kronecker delta and ϵ is the specific internal energy so that $e = \rho(1+\epsilon)$ is the energy density in the rest-frame of the fluid. These equations are closed using an ideal-gas equation of state $p = (\Gamma-1)\rho\epsilon$, with adiabatic exponent $\Gamma = 2$. The solution of relativistic hydrodynamics equations is obtained via a conservative formulation of (7.2) as discussed in [9] and the use of high-resolution shock-capturing (HRSC) schemes with a piecewise parabolic method (PPM) for the reconstruction of the primitive variables. The time-stepping is done with a third-order total-variation diminishing Runge-Kutta algorithm. Finally, the spatial discretization is done on a uniform grid having resolution of either $h = 0.1$ (medium resolution) or

Table 7.1: Properties of some of the representative models considered and shown either in figure 7.1 or in figures 7.5 and 7.6. More specifically, N_1 and S_1 are the extremes of the range of central densities considered, P_1 is a largely subcritical model which expands to models P_2–P_4 as the resolution is increased, while Q_1 and R_1 represent the closest super and subcritical approximation of the critical solution, respectively.

Point	ρ_c	K	$M_{\rm ADM}$	M_b	subcritical	supercritical
N_1	0.00395000	71.77	1.3879	1.5194	$\surd$	$-$
P_1	0.00459316	71.39	1.3832	1.5194	$\surd$	$-$
P_2	0.00341517	72.23	1.3754	1.5077	$\surd$	$-$
P_3	0.00378525	71.58	1.3788	1.5134	$\surd$	$-$
P_4	0.00387685	71.61	1.3809	1.5161	$\surd$	$-$
Q_1	0.00459322	71.39	1.3832	1.5194	$-$	$\surd$
R_1	0.00459322	71.39	1.3832	1.5194	$\surd$	$-$
S_1	0.00508840	71.95	1.3842	1.5194	$-$	$\surd$

$h = 0.08$ (high resolution). The outer boundary of the computational domain is set at $R = 15$ and we have verified that the proximity of the outer boundary does not influence significantly the critical solution.
The equilibrium configuration curves in the $(\rho, M_{\rm ADM})$ plane and the perturbative oscillations frequencies quoted in the text have been computed using two codes kindly provided to us by S'i. Yoshida [102] and C. Chirenti [109].

7.1.1 Initial Data

The initial data consists of a family of spherical stars having fixed baryonic mass

$$M_b = 1.5194 \equiv \bar{M}_b \,, \tag{7.4}$$

constructed using a polytropic equation of state $p = K\rho^\Gamma$, with $\Gamma = 2$. Each model is computed by fixing its central rest-mass density, ρ_c, while the value of K is fixed after imposing the condition (7.4). The reason for this choice is that we want to guarantee that all the models considered have, at least initially, the same baryonic mass to the precision in expression (7.4). Solutions with different baryonic mass, in fact, are effectively in different phase spaces and thus not useful when looking at a critical behaviour. Of course different models will also be slightly different because the perturbations will slightly alter their mass-energy or because although M_b is conserved to high precision by employing a conservative formulation of the equations, it is nevertheless not conserved to machine precision. All of these latter errors, however, are entirely resolution dependent and can, therefore, be singled out by considering simulations at different resolutions.
These initial models have been evolved under the sole effects of the perturbations induced by the truncation error. Besides depending on resolution (and converging away), the amplitude of these perturbations is difficult to measure as it depends on a number of different sources of error, such as the interpolation error of the one-dimensional initial data on the three-dimensional Cartesian grid, or the treatment of low density "atmosphere" regions, which are not measurable directly. However, an indirect measure can be obtained by looking at a short evolution of a stable spherical star which, in absence of any numerical error, would not exhibit any dynamics but which, in practice, oscillates under the effects of these perturbations [6, 9, 18, 38, 100, 106, 110]. The amplitude of the observed

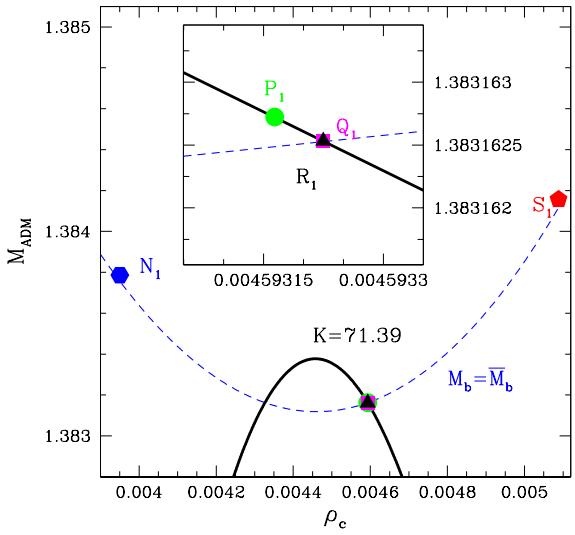

Figure 7.1: Position of some of the most important models in the $(\rho_c, M_{\rm ADM})$ plane, where the solid (black) line refers to a sequence with $K = 71.39$, while the dashed (blue) line refers to a sequence of models having baryonic.mass $M_b = 1.5194 = \bar{M}_b$. The points N_1 and S_1 are the extremes of the range of central densities considered [*cf.*eq. (7.5)], P_1 is a largely subcritical model, while Q_1 and R_1 represent the closest super and subcritical approximation of the critical solution, respectively. The inset shows a magnification of the region near the critical solution; the properties of the model are reported in table 7.1.

oscillations can be then interpreted as an indirect measure of the numerical perturbation. In particular, we can consider the value of the average velocity in the radial direction during the first iterations as an estimate of the amplitude of an equivalent velocity perturbation. In this case, for a spherical star with $\rho_c = 0.00128$ and $K = 100$ evolved for 100 time-steps on a $h = 0.1$ grid, we measure an average velocity, $v^r \simeq 1.1 \times 10^{-5}$. Further insight can also be gained by the average of the momentum constraint violation in the radial direction and the Hamiltonian constraint violation, which we measure to be $\simeq 2.3 \times 10^{-7}$ and $\simeq 6.1 \times 10^{-6}$, respectively.

The determination of the critical value of the central density $\rho_c^\star$ is obtained rather straightforwardly via a bisection-like strategy within the initial interval

$$0.00395 < \rho_c < 0.0050884\,, \tag{7.5}$$

where the extrema correspond to a stable oscillating star or to one collapsing promptly to a black hole, respectively.

The main properties of the initial data are collected in table 7.1 and summarized in figure 7.1, which reports the position of some of the most important models discussed in this paper in the $(\rho_c, M_{\rm ADM})$ plane. More specifically, N_1 and S_1 are the extremes of the range of central densities considered [*cf.*eq. (7.5)], P_1 is a largely subcritical model which expands to models P_2–P_4 as the resolution is increased (*cf.*figure 7.5), while Q_1 and R_1 represent the closest super and subcritical approximation of the critical solution, respectively. Note that R_1 and Q_1 differ only by the 4.6×10^{-8} % in the central density and thus they appear identical in the figure. Note also that P_1, Q_1 and R_1 are all on the unstable branch of the models of equilibrium and are therefore linearly unstable.

As a final remark we note that although the use of an axisymmetric system of equations is not strictly necessary for the spherically-symmetric initial data considered here, their numerical solutions in 2 spatial dimensions via the `Whisky2D` code has been useful in view of the connections between the critical behaviour discussed here and the one presented in the companion paper [24], where the head-on collision of equal-mass neutron stars is considered. The possibility of using the same numerical infrastructure and comparable truncation errors has been in fact very important in determining the connections between the two critical behaviours.

7.2 Results

In what follows we discuss the nonlinear dynamics of the spherical stars as these evolve away from their initial state on the unstable branch and exhibit a critical behaviour.

7.2.1 Critical solution

We first consider the evolution of models in the window (7.5) under the sole effect of the numerically-induced perturbations. Some of these models, namely the supercritical ones, collapse to black hole, while others, namely the subcritical ones, undergo a sudden expansion followed by a relaxation towards the corresponding model on the stable branch of the spherical star solutions. This is clearly shown in figure 7.2, which reports the evolution of the central rest-mass density and where different lines refer to different initial data in the interval

$$0.0045931640625 \leq \rho_c \leq 0.00459371875\,. \tag{7.6}$$

By looking at left panel figure 7.2 it is quite apparent how the survival time of the metastable solution increases as the initial models approach the critical threshold and both the subcritical and the supercritical solutions overlap for a long part of the evolution, before departing exponentially. It is also worth remarking that the linear stability analyses of theses models indicates that they are linearly unstable with a characteristic collapse time (*i.e.* the inverse of the imaginary part of the complex eigenfrequency of the fundamental mode) $\tau \simeq 440$. Yet, as shown in figure 7.2, the metastable models survive for much longer times and for almost $\tau \simeq 850$ for the models closest to the critical threshold. A similar behaviour in the evolution of the central rest-mass density has been observed also in the simulations reported in [18], although those refer to magnetized and rotating stellar models and thus, being them result of three-dimensional simulations, are restricted to a much smaller interval of significant figures. In addition, and as mentioned in the Introduction, evidence for a type-I critical behaviour for the evolution of the central rest-mass density has been shown also in the head-on collision of two equal-mass spherical stars [20] and will be further discussed in the companion paper [24].
As the secular evolution in the central density is a well-known "feature" of the numerical solution of relativistic multidimensional stellar models and has been observed in codes implementing very different numerical methods and formulations of the Einstein equations [6, 9, 18, 38, 100, 106, 110], we have isolated this secular behaviour by computing a least-square fit of the common part of the evolution in order to isolate the true dynamics from the low-frequencies numerical components. More specifically, we have modeled the evolution of the central rest-mass density of the metastable equilibrium via the *Ansatz*

$$\phi(t) = \rho_0 + \rho_1 t + \rho_2 \cos(2\pi h_1 t + \varphi_1) + \rho_3 \cos(2\pi h_2 t + \varphi_2)\,, \tag{7.7}$$

where $\rho_0 - \rho_2$ are just coefficients in the interpolation and do not have a particular physical meaning. On the other hand, the frequencies h_1 and h_2 are chosen as the two smallest frequencies appearing

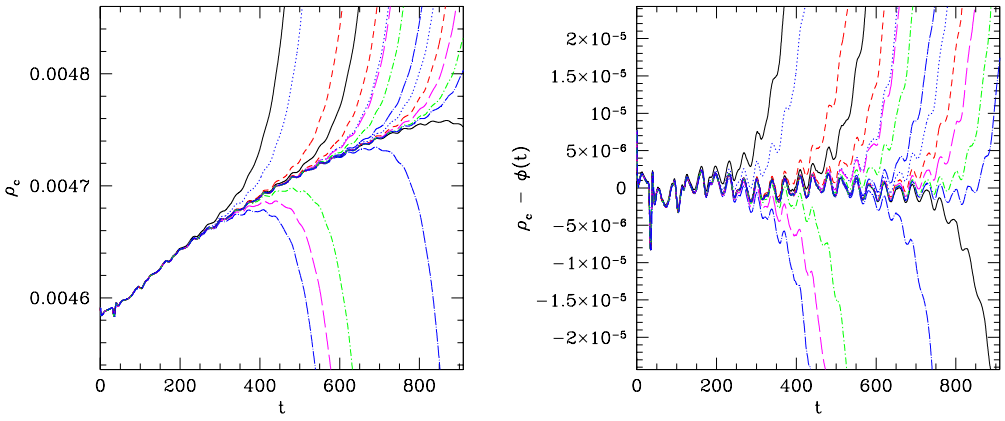

Figure 7.2: Left panel: evolution of the central rest-mass density near the critical threshold with different lines referring to different initial models. Right panel: the same as in the left panel but corrected for the secular evolution given by eq. (7.7).

in the Fourier spectrum of the central density during the metastable phase (*cf.*figure 7.3 and see also discussion below on the spectral power density of the putative critical solution). The residuals after the fit are shown in the right panel of figure 7.2 and help considerably in appreciating the dynamics of the unstable models near the critical value.
Using a large set of simulations with resolution of $h = 0.1$ and a straightforward bisection strategy we have located the critical threshold to black-hole formation at a central density

$$\rho_c^\star = 0.004593224802 \pm 2.1 \times 10^{-12}\,. \tag{7.8}$$

Clearly, we expect this value to depend on the initial perturbation and thus on the resolution used, as well as on the numerical method employed. On the other hand, we also expect that the associated solution and the critical exponent to be "universal", in the sense that they should not depend depend sensitively on the perturbation or on the particular family of initial data as far as this family is characterized by a single parameter and thus intersects the critical manifold $\mathcal{C}$ in a single point which is near enough to this solution. In this case, in fact, the associated critical solution is supposed to be at least locally attractive on a sub-manifold of the phase space of co-dimension one.
To validate that the behaviour discussed so far and shown in figure 7.2 does represent a type-I critical behaviour we compute the survival time of the metastable solution τ, *i.e.* the *"escape time"*, and study how this varies as the critical solution is approached. We recall that we expect that the escape time near the critical for a type-I critical phenomena should behave as

$$\tau = -\frac{1}{\lambda}\ln|\rho_c - \rho_c^\star| + \text{const}\,, \tag{7.9}$$

and such expected solution is indeed shown as a dashed line in figure 7.4. Also shown with squares and triangles are the computed escape times for different initial data and different resolutions (blue squares for $h = 0.1$ and red triangles for $h = 0.08$). The latter are calculated in terms of the time τ_ϵ at which the relative difference between the observed central baryonic density and the best approximation of the critical solution $\phi(t)$ (7.7) becomes larger than ϵ. We find that, for a large enough ϵ, such that $1 \gg \epsilon > \epsilon^\star > 0$, these times depend only weakly on ϵ and thus give a good measure of the departure time from the critical solution. A value of $\epsilon = 0.5\%$ provides a sufficiently accurate measure and this is the one employed for the data points shown in figure 7.4. We finally estimate the critical exponent

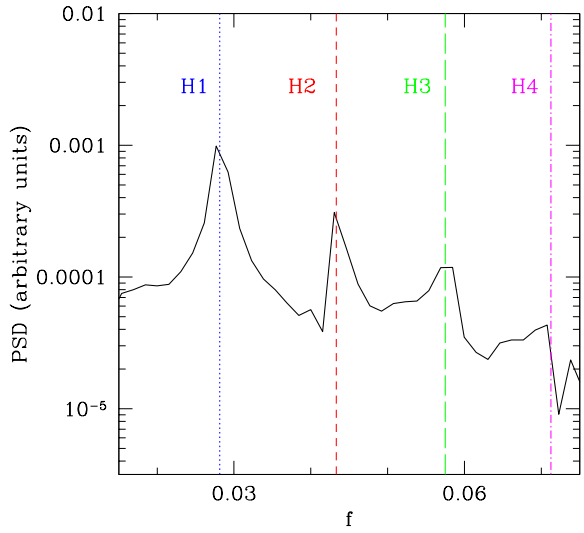

Figure 7.3: Power spectral density of the evolution of the central rest-mass density for the model closest to the putative critical solution (*i.e.* with $\rho_c = 0.0045932248034$) when the secular drift part (7.7) has been removed from the data. The eigenfrequencies associated with the corresponding spherical star model are also shown as vertical lines.

λ by making a linear least-square regression of the data points of sub- and supercritical solutions and then by taking the average of the two values. Using the medium-resolution $h = 0.1$ simulations we therefore obtain for the critical exponent

$$\lambda = 0.02149665\,, \tag{7.10}$$

with a coefficient of determination R^2 relative to the linear regression (7.9) and computed on the full dataset containing both sub and supercritical solutions, of 0.960517. The critical exponent (7.10) is found also in the case of the $h = 0.08$ simulations, although in this case the scattering is somewhat larger and the data agrees within 7%. We note that these high-resolution simulations are computationally very expensive and this is why we have restricted them to a smaller set of initial data. Clearly, the match between the computed escape times and the one expected from the critical behaviour is very good over the 6 orders of magnitude in $|\rho_c - \rho_c^\star|$ spanned by our data-set and thus provide convincing evidence that indeed critical behaviour can be found in the dynamics of linearly unstable spherical stars.

As a final remark we note that while the evidence for a critical behaviour is clear, much less clear is the physics of the critical solution which is, after all, a perturbed spherical star. Recent studies of nonlinear perturbations of relativistic spherical stars have shown that linearly unstable stars can be stabilized via nonlinear couplings among higher-order modes [111]. It is possible that such a nonlinear coupling is present also here and we conjecture therefore that the stability of the metastable solution is due to mode coupling of the first overtones of the fundamental mode. Support to this conjecture comes from the power spectral density in figure 7.3, which shows that, apart from the F-mode which is obviously missing as it has only imaginary eigenfrequency, the spectrum of the metastable solution is essentially identical to the one of an excited spherical star with $(\rho_c, K) = (\rho^\star, K^\star)$ and $M_b = \bar{M}_b$. Interestingly, most of the energy is in the first overtone, $H1$, even though the numerical perturbation can be thought

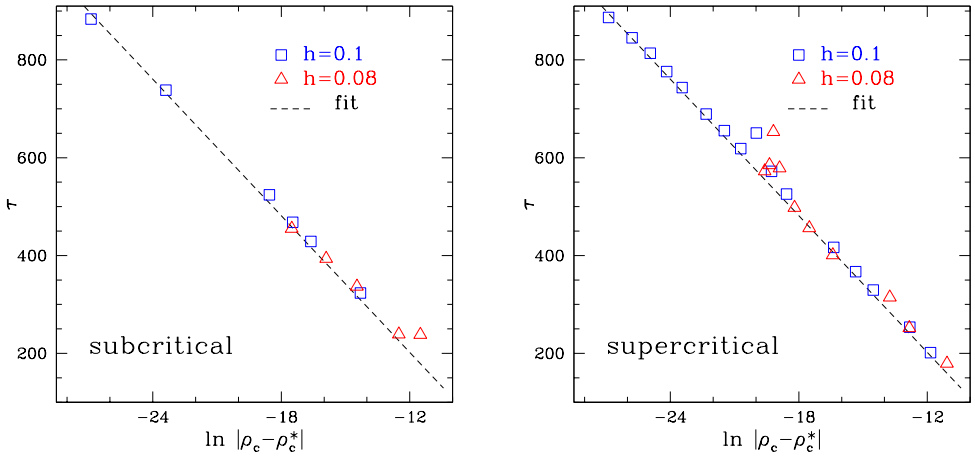

Figure 7.4: Escape time τ as a function of $\ln|\rho - \rho^\star|$ for subcritical (left panel) and supercritical solutions (right panel), respectively. The blue squares corresponds to the results obtained with the $h = 0.1$ resolution, while the red triangles to the results obtained with the $h = 0.08$ resolution. The dashed lines represent the fit obtained using (7.9) with the λ obtained from the $h = 0.1$ solutions.

as "white noise" exciting all the modes of the star with almost equal energy. The behaviour discussed above persists also when considering models with higher spatial resolutions.

7.2.2 Subcritical solutions

While the final fate of supercritical solutions is clearly that of leading to a collapse and to the formation of a black hole, the one of subcritical solutions deserves a more detailed explanation. As one would expect, given that the initial data represent linearly unstable stars, the subcritical solutions show a first expansion as the star migrates to the stable branch of the equilibrium configurations, which is then followed by a slow relaxation where the central rest-mass density exhibits strong oscillations around smaller and smaller values, that would eventually reach in the continuum limit, the value corresponding to the model on the stable branch having the same gravitational mass of the initial one. In practice, however, the migration to the stable branch is accompanied small losses both in the gravitational mass and in the rest-mass which, although smaller than $\simeq 0.7\%$, need to be taken properly into account.

More specifically, we have analyzed in detail the evolution of the largely subcritical model P_1, (*cf.*table 7.1), which is an unstable spherical star with an F-mode whose imaginary part of the eigenfrequency is $\nu_i = 0.461\,\mathrm{kHz}$. We evolve therefore evolved such a model it with three different spatial resolutions of $h = 0.1$, $h = 0.09$ and $h = 0.08$, and studied its migration to the stable branch. The asymptotic state of the solution and in particular to the final central rest-mass density ρ_f is estimated by modeling the time evolution of the oscillating star on the stable branch with a simple *Ansatz* of the type $\rho(t) = \rho_f + \rho_1/t$ and by performing a nonlinear least square fit on an appropriate window including the final part of the dynamics. For any given resolution we have then computed the total baryonic-mass losses due to the numerical dissipation $\Delta M_b = M_b - M_{b,f}$, and determined the polytropic coefficient K_f yielding a spherical stellar model with central rest-mass density ρ_f and baryon mass $M_{b,f}$. Clearly, for such a model it is then also possible to compute the gravitational mass and thus track the migration on a $(\rho_c\,, M_{\rm ADM})$ plane.

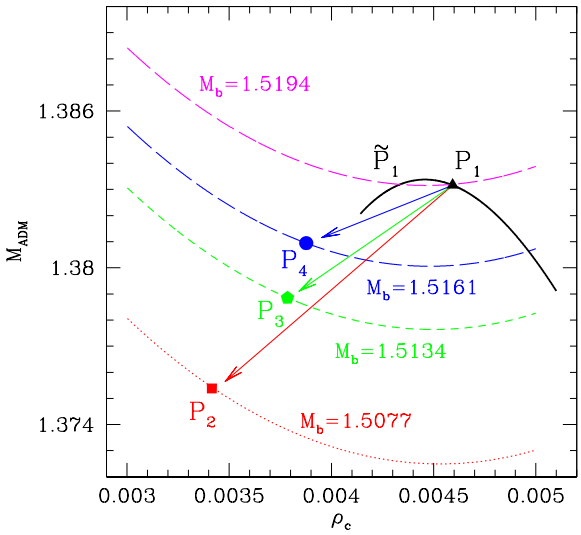

Figure 7.5: Dynamics of the migration on a $(\rho_c\,, M_{\rm ADM})$ plane. The linearly unstable and largely subcritical model P_1 migrates to a new solution on the stable branch of equilibrium configurations. Indicated with $P_2 - P_4$ are the new asymptotic states for resolutions $h = 0.1 - 0.08$, respectively. Indicated with a thick solid line is the sequence of initial models having the same polytropic index of P_1, while indicated with dotted and dashed lines are sequences of models having the same rest-mass as the asymptotic models $P_2 - P_4$. Finally, shown as $\tilde{P}_1$ is the asymptotic state of P_1 in the continuum limit; note that even for the coarse-resolution case the changes in baryonic and rest-mass are only of $\simeq 0.7\%$.

The overall results of these migrations are shown in figure 7.5, where we report the stellar configurations on $M_b = \text{const.}$ curves. The minimum of each curve corresponds to the maximum in the usual $(\rho, M_{\rm ADM})$, $K = \text{const.}$, plots and separates the stable and unstable branches of solutions. When a resolution of $h = 0.1$ is used the model P_1 migrates to the new asymptotic model P_2, while it will migrate to models P_3 and P_4 as higher resolutions of $h = 0.09$ and $h = 0.08$ are used, respectively. Note that already with the coarsest resolution of $h = 0.1$ the losses in gravitational masses are $\simeq 0.65\%$ and that these decrease to $\simeq 0.16\%$ when a resolution of $h = 0.08$ is used. Finally, indicated with $\tilde{P}_1$ is the expected asymptotic model when the numerical losses are extrapolated to the continuum limit[1]; clearly, in the limit $h \to 0$, the migration of model P_1 takes place to a new state having the same gravitational and baryonic mass as the initial one.

7.2.3 Perturbation of nearly-critical solutions

As discussed in Sect. 7.2.1, the central rest-mass density of the linearly unstable models can be used as a critical parameter for the gravitational collapse of a linearly unstable spherical star, in contrast to what has been observed for example by Novak in [15] or by Noble in [17]. We believe this is due to the very different set of initial data selected here and in [15, 17]. Indeed, the reason why this behaviour has not been observed in many previous studies is that we consider initial stellar models that are

[1]Note that we do not mark this point with a symbol as it does not correspond to a numerically computed value, as it instead for P_2, P_3 and P_4

already linearly *unstable*, in contrast with what done in [15, 17], where the initial models are instead linearly *stable* and then subject to a perturbation (either by introducing a radial velocity [15,17], or by considering employing the interaction with a scalar field [16]). For our set of initial data, therefore, the critical solution is essentially a spherical star with an unstable F-mode, and any finite perturbation exciting this mode will change the solution in a dramatic way (A discussion of this change within a phase-space description will be made later on when presenting figure 7.7)[2].

To confirm this hypothesis, we follow [15] and [17], and construct a new family of spherical initial data obtained by perturbing the slightly supercritical model Q_1 (*cf.*table 7.1) via the addition of a radial velocity perturbation in the form of the 3-velocity component

$$v^r(x) = \frac{U}{2}(3x - x^3), \qquad x \equiv \frac{r}{R_\star}\,, \tag{7.11}$$

where U is the amplitude of the perturbation at the surface of the star, $R_\star$ and can be either positive (outgoing radial velocity) or negative (ingoing radial velocity). Because the perturbation (7.11) matches the eigenfunction of an idealized F-mode perturbation, it should excite the only unstable mode of the critical solution.

Performing simulations for different values of U and a resolution $h = 0.1$ we find, not surprisingly, that for negative values of U the perturbed models of Q_1 collapse to a black hole. Furthermore, because in this case the radial velocity accelerates the development of the unstable mode, the larger the values of U the shorter the time to collapse, *i.e.* $\tau \sim -c_1 \log(U) + c_2$, where c_1 and c_2 are positive constant coefficients. On the other hand, for positive values of U, the perturbed models of Q_1, which we recall is supercritical for $U = 0$, becomes subcritical and shows the same qualitative behaviour as that of model R_1. Hence, a suitably perturbed supercritical model can behave as a subcritical one.

The dynamics of these perturbed, nearly-critical models is shown in figure 7.6, where the solid (black) line represents the supercritical solution Q_1, while the dotted (blue) line represents the subcritical solution R_1. The dashed lines show again the evolution of Q_1, but when subject to a positive (red short-dashed line) or negative (green long-dashed line) velocity perturbation. The dynamics shown in figure 7.6 underlines an important characteristic of critical phenomena: the precise value of the critical parameter at the intersection between the one-parameter family of solutions and the critical manifold depends on the family itself. In particular this means that if we fix a value of the perturbation amplitude, $U \neq 0$, we have to expect to find the critical solution at a value of $\rho_c^\star(U)$ different from the one quoted in (7.8) which is attained in the case $U = 0$. For this reason the application of a non infinitesimal perturbation to a nearly-critical solution results in a dramatic change in the dynamics of the system.

The phase-space representation of this concept is summarized in figure 7.7, where we show two one-parameter families of perturbed TOV initial data, whose critical parameter, ρ_c, is the central rest-mass density. The perturbation is given by the composition of truncation errors and of a radial velocity perturbation U in the form (7.11), where $U = 0$ or $U = U_0 > 0$. As these families represent different initial configurations, they will intersect the critical manifold $\mathcal{C}$ at two different points, with correspondingly different values of the critical parameter $\{0, \rho_c^*(0)\}$ and $\{U_0, \rho_c^*(U_0)\}$ (these points are marked as filled circles)[3]. In particular, when U runs between 0 and U_0, the set of critical configurations $\{U, \rho_c^*(U)\}$ will represent a curve on the critical manifold $\mathcal{C}$ and this is shown with a violet

[2]With "perturbation" we are here referring to a globally coherent, resolution independent perturbation such as the one given in eq. (7.11). This has to be contrasted with the random, truncation-error induced and resolution-dependent perturbations we have considered in Sect. 7.2.1

[3]In our notation, the point $\{U_0, \rho_c^*(U_0)\}$ is the critical solution with initial velocity perturbation given by (7.11) with $U = U_0$. Similarly, a configuration $\{U_0, \rho_c^*(0)\}$ will be a member of the family with initial velocity perturbation U_0, but with a central density which is the critical one for a model with $U = 0$

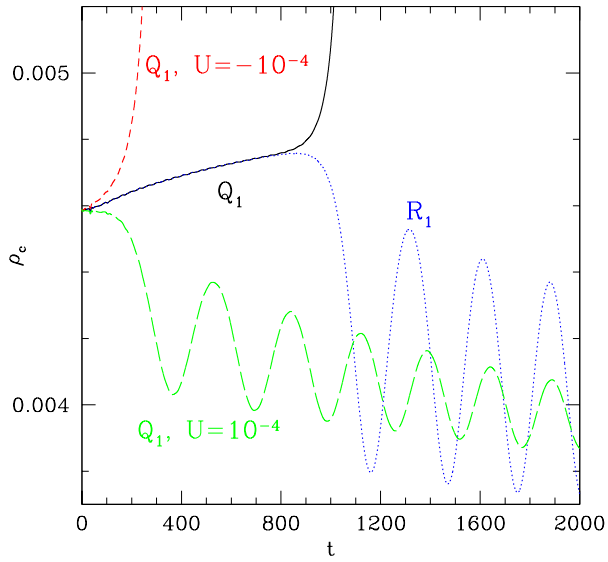

Figure 7.6: Perturbation of nearly-critical solutions. The solid (black) line represents the supercritical solution Q_1, while the dotted (blue) line represents the subcritical solution R_1. The dashed lines show again the evolution of Q_1, but when subject to a negative (red short-dashed line) or positive (green long-dashed line) velocity perturbation. Clearly, in the latter case the supercritical solution Q_1 becomes subcritical and shows the same behaviour as the solution R_1.

solid line in figure 7.7. Considering now a configuration near $\{0, \rho_c^*(0)\}$ and applying to it a velocity perturbation in the form (7.11) with $U = U_0$, will produce a new configuration $\{U_0, \rho_c^*(0)\}$ which is not necessarily on the critical manifold (this is marked with a filled square). Indeed, the whole family $\{U, \rho_c^*(0)\}$, that is the set of configurations with a nonzero initial velocity perturbation but central density which is the critical one for the zero-velocity case, are in general expected to be outside the critical domain. The family $\{U, \rho_c^*(0)\}$ is shown with a black dot-dashed line in figure 7.7.
As a final remark we note that another important difference between the work presented here and that in [15,17] is that the we find evidence of a type-I critical behaviour with a periodic solution, in contrast to what found in [15, 17], which is instead of type-II and with DSS solutions. We believe the origin of this important difference and of the presence of a periodic solution is in our use of an ideal-fluid EOS and hence in the presence of an overall scale in the problem. Conversely, the spherical stars considered in the above mentioned works were evolved using either an ultra-relativistic EOS [13] (which, as commented in the Introduction, are intrinsically scale-free) or with very strong perturbations [15, 17], thus in a regime of the EOS which is approximatively ultra-relativistic [11].

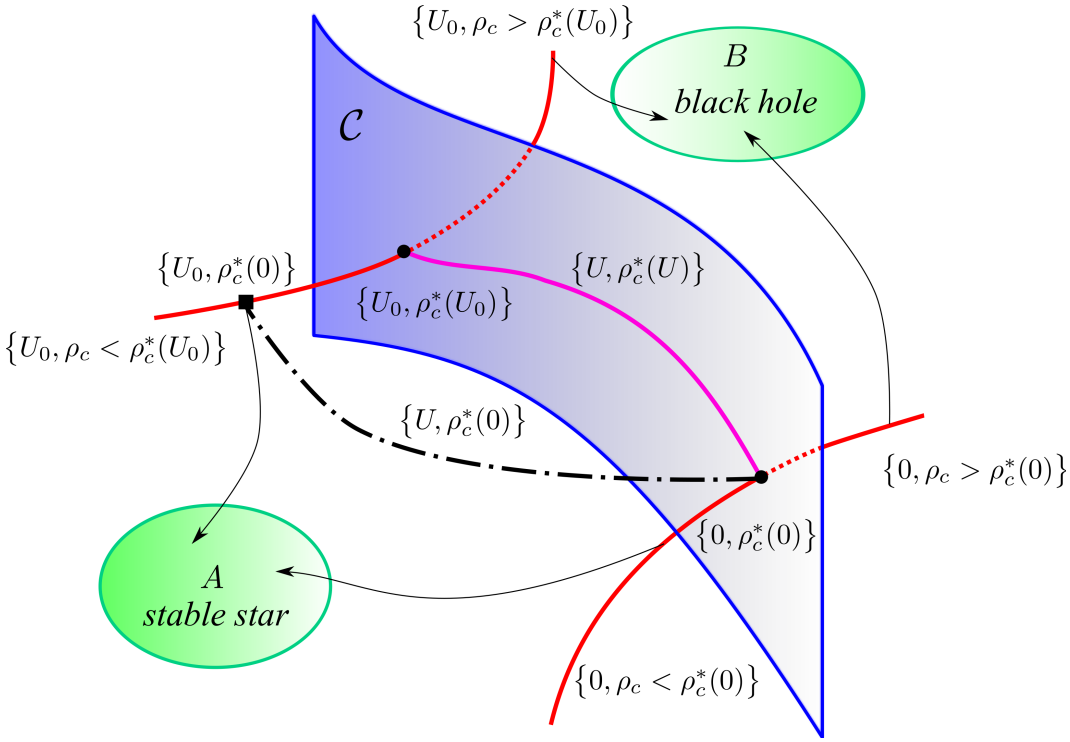

Figure 7.7: Phase-space diagram representation of nearly-critical solutions. In particular, we show with red solid curves two one-parameter families of initial data, perturbed by the addition of a radial velocity profile in the form (7.11) with $U = 0$ or $U = U_0 > 0$. The locus of the critical points, $\{U, \rho_c^*(U)\}$, is shown with a violet solid line, while the family of initial-data $\{U, \rho_c^*(0)\}$ is shown with a black dot-dashed line and the point $\{U_0, \rho_c^*(0)\}$ is marked with a filled square. The latter represents therefore the family of initial data obtained by adding a velocity perturbation with amplitude U to the model with central density would when $U = 0$. Also highlighted with filled circles are the critical points for the families with $U = 0$ and $U = U_0$, *i.e.* $\{0, \rho_c^*(0)\}$ and $\{U_0, \rho_c^*(U_0)\}$.

Chapter 8

Critical phenomena in neutron stars: Head-on collisions

8.1 Numerical Setup

All the simulations presented here have been performed using an ideal-gas EOS, $p = (\Gamma - 1)\rho\epsilon$, where ρ is the baryonic density and ϵ the specific internal energy in the rest frame of the fluid. The discretization of the spacetime evolution equations is done using fourth-order finite-differencing schemes, while we HRSC methods with PPM reconstruction for the hydrodynamics equations. The time-stepping is done with a third-order TVD Runge-Kutta scheme and despite the use of higher-order methods, the convergence order drops to about 1 after the two NSs have merged and large shocks develop (see [112] for a discussion on the convergence order in relativistic-hydrodynamics simulations).
The spatial discretization is done via a grid with uniform resolution, which we have taken to be either $h = 0.1\ M_\odot$ or $h = 0.08\ M_\odot$. Furthermore, as long as non-spinning NSs are considered, the head-on collision also possesses a symmetry across the plane midway between the two stars and orthogonal to the colliding direction. As a result, the problem needs to be solved only for one star and suitable boundary conditions be applied across the symmetry plane. The outer boundary of the computational domain is set at $60\ M_\odot$ and thus rather close to the two stars. However, this is adequate since we are not interested here in extracting gravitational waveforms and since we have verified that the violation of the constraints at the outer boundaries are not larger than elsewhere in the computational domain.
As a final remark we note that we use the same gauges as those employed in [113] and thus the slicing is sufficiently "singularity-avoiding" that it is not necessary to perform an excision of the field variables when following the evolution of a supercritical solution. However, because of the very high-resolution used, the rapid growth of the rest-mass density is not compensated by the intrinsic numerical dissipation as instead happens in [113] or in [107]. As result we excise the solution of the hydrodynamical quantities only as discussed in [106, 114] in order to obtain a stable, long-term solution.

8.2 Initial data

Our initial data consists of two equal-mass non-rotating NSs having initial coordinate separation, computed as the coordinate distance between the two stellar centers, of $20\ M_\odot$. Following [20], we construct these stars using a polytropic EOS, $p = K\rho^\Gamma$, with adiabatic exponent $\Gamma = 2$ and polytropic constant $K = 80$, which is equivalent to $K = 0.00298\ c^2/\rho_{\rm n}$, and where $\rho_{\rm n} = 2.3 \times 10^{14}\ {\rm g/cm}^3$

is approximately the nuclear density. The stars at the critical point have a radius of $R = 14.7$ km, a baryon/gravitational (ADM) mass of $0.760/0.732\,M_\odot$. The main properties of the critical solution are reported in table 8.1, where they are indicated as model "A".
Note that the maximum baryon/gravitational mass for the chosen value of the polytropic constant is $1.609/1.464\,M_\odot$ and thus the object produced by the collision will have a baryon/gravitational mass which is above such maximum mass. However, as we will discuss below and in contrast with the claim made in [20], this can still lead to equilibrium solution for a TOV star.

Table 8.1: Equilibrium models used for the collision (model A) or that are discussed in figure 8.5 (models B and C). Listed are: the value of the gravitational (ADM) mass, the total rest-mass, the radius of the star, the central rest-mass density and the polytropic constant K. For each model we also report the maximum allowed ADM and rest-masses for a TOV having the same polytropic constant.

Model	$M_{\rm ADM}$	M_b	R (km)	ρ_c	K	$M_{\rm ADM,max}$	$M_{b,\rm max}$
A	0.732	0.760	14.761	0.00058	80	1.464	1.609
B	1.505	1.514	9.135	0.00963	145	1.972	2.166
C	1.460	1.547	19.003	0.00055	155	2.038	2.240

The stars constructed in this way are then boosted towards each other along the z-axis with a velocity $v_0 = 0.15$, which is similar to the free-fall velocity as computed from the Newtonian expression for a point-particle. With these choices the only remaining free parameter needed to characterize the initial data is the central rest-mass density of the two NSs, ρ_c, which we use as our critical parameter (We note that the value chosen for the initial velocity does influence qualitatively the results obtained and indeed it can act as a critical parameter in a sequence at constant ρ_c [20]).

8.3 Results

We next discuss the dynamics of the collision and the properties of the critical solution as they appear from our numerical simulations.

8.3.1 Dynamics of the collision

The basic dynamics of the process is rather simple to describe. As the two NSs are accelerated towards each other by the initial boost and the mutual gravitational attraction, they collide, leading to a merged object which is wildly oscillating and with a mass which is above the maximum mass of the initial configuration. Depending on whether the initial central density is larger or smaller than the critical one, the metastable solution either collapses to a black hole (supercritical solutions) or it expands to a new stable stellar solution (subcritical solutions).
Before entering the details of the discussion it may be useful to remark that the simulation of the head-on collision of two NSs in the neighborhood of the critical solution is a very demanding calculation, even for modern general-relativistic hydrodynamical codes. This is because adaptive mesh refinements do not provide any significant speed up and, at the same time, rather high level of resolutions are needed to capture the dynamics faithfully. In spite of these computational difficulties mentioned above, using the `Whisky2D` code we are able to identify the critical value for ρ_c with an accuracy of 11 significant digits, a level of precision never achieved before in the study of NS head-on collisions.

More specifically, we have measured the critical central density

$$\rho_c^\star = (5.790998966725 \pm 0.00000000003) \times 10^{-4}. \tag{8.1}$$

as the midpoint between the largest central rest-mass density among the subcritical models and the smallest central rest-mass density among the supercritical ones. In other words, binaries with $\rho_c > \rho_c^\star$ have been simulated to collapse to a black hole, while binaries with $\rho_c < \rho_c^\star$ have been computed to expand to a stable star.
As pointed out by [20], this value will ultimately depend on the numerical resolution used and the other discretization parameters. Nevertheless, given a set of initial data and numerical setup, (8.1) gives a precise measure of how close we are able to get to the critical solution.

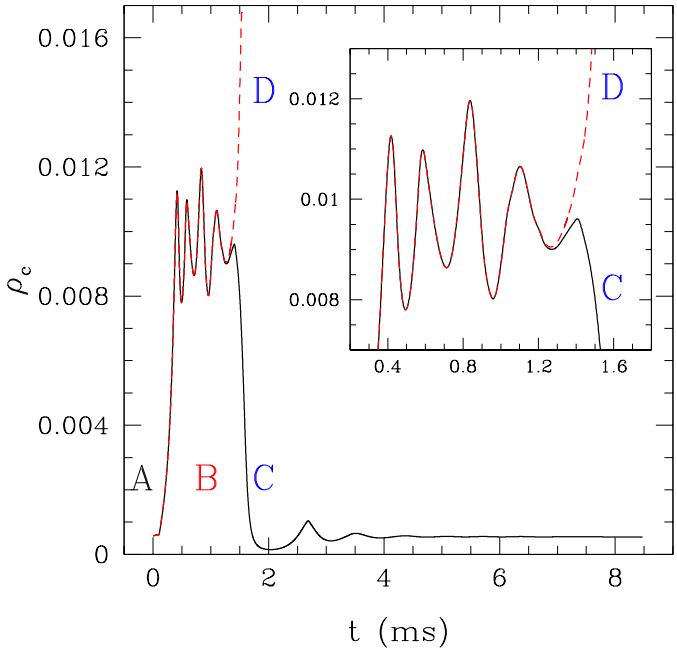

Figure 8.1: Evolution of the maximum rest-mass density of the most massive subcritical model with initial value $\rho_c = 0.000579099896670$ (black solid line) the least massive supercritical model with initial value $\rho_c = 0.000579099896675$ (red dashed line). Also highlighted are the four different phases of the dynamics. The first one corresponds to the initial configuration of the system (labeled as "A"). After the collision, a new metastable solution is created during which the central density exhibits violent oscillations (labeled as "B"); the subcritical and supercritical solutions are essentially indistinguishable during this stage. Finally the subcritical and supercritical solutions separate, with the first one relaxing to a stable expanded configuration (labeled as "C"), while the second collapses to a black hole (labeled as "D").

Compressed in figure 8.1 is a considerable amount of information about the criticality of the head-on collision. More specifically, we show the time evolution of the central rest-mass density of the heaviest subcritical model (black solid line) and lightest supercritical model (red dashed line) computed. Overall, we can distinguish three different phases of the dynamics. In the first one (marked with "A"

in the figure) the central density increases from its initial value to a maximum one reached, which is attained when the stellar cores merge.

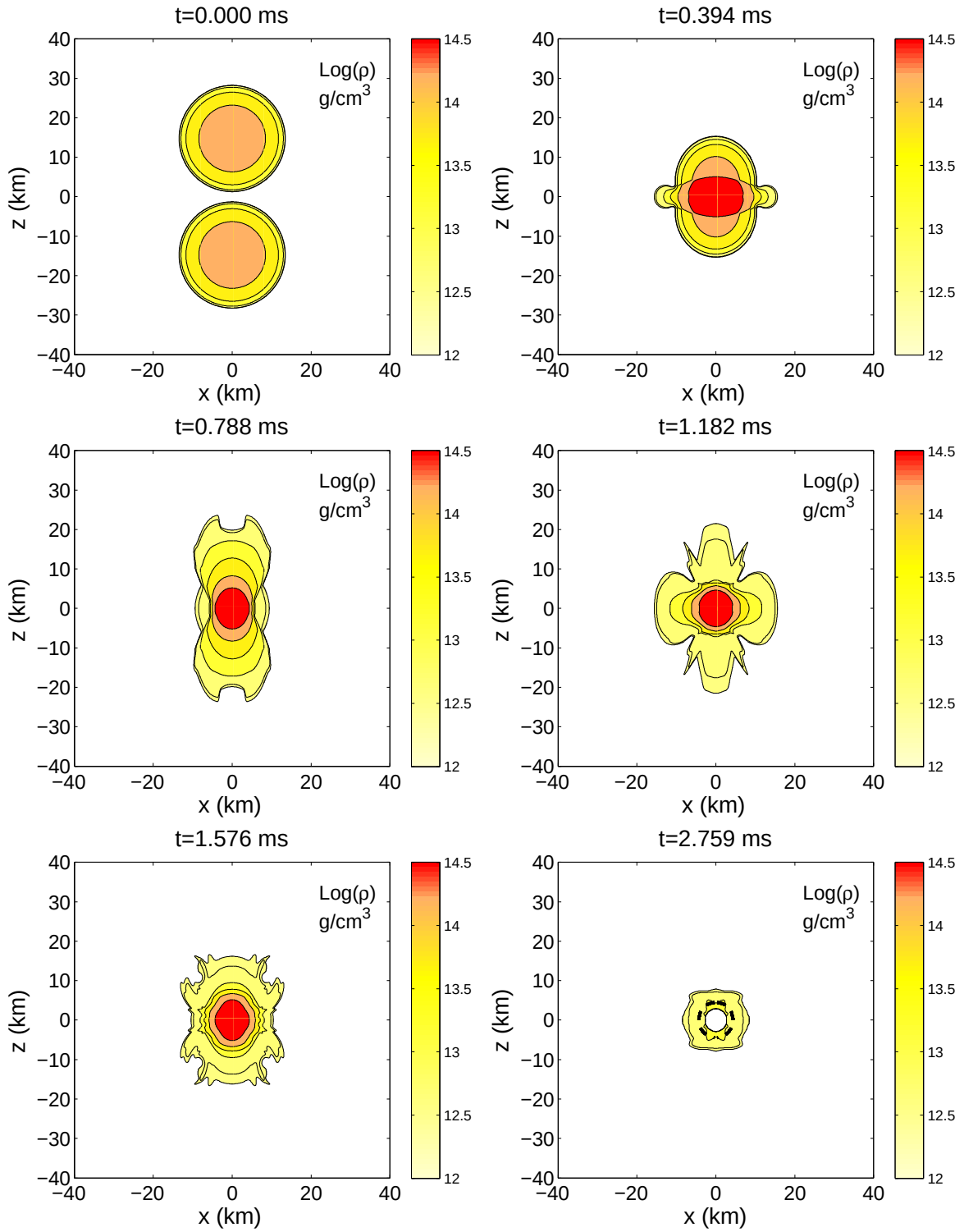

Figure 8.2: Iso-density contours in the (x, z) plane of the least massive supercritical solution ($\rho_c = 0.000579099896675$). The corresponding times are shown at of each panel, while the color-code for the rest-mass density is indicated to the right. The isolines are shown for the values of $\rho = 10^{12.6}, 10^{12.7}, 10^{13.2}, 10^{13.7}, 10^{14.2}$ and $10^{14.7}$ g/cm^3. The second frame ($t = 0.394$ ms) is taken during the merge process. The next five frames illustrate the star during the metastable equilibrium. Finally the last frame ($t = 2.759$ ms) shows the solution after the formation of a black hole, whose apparent horizon is shown with a thick black dashed line.

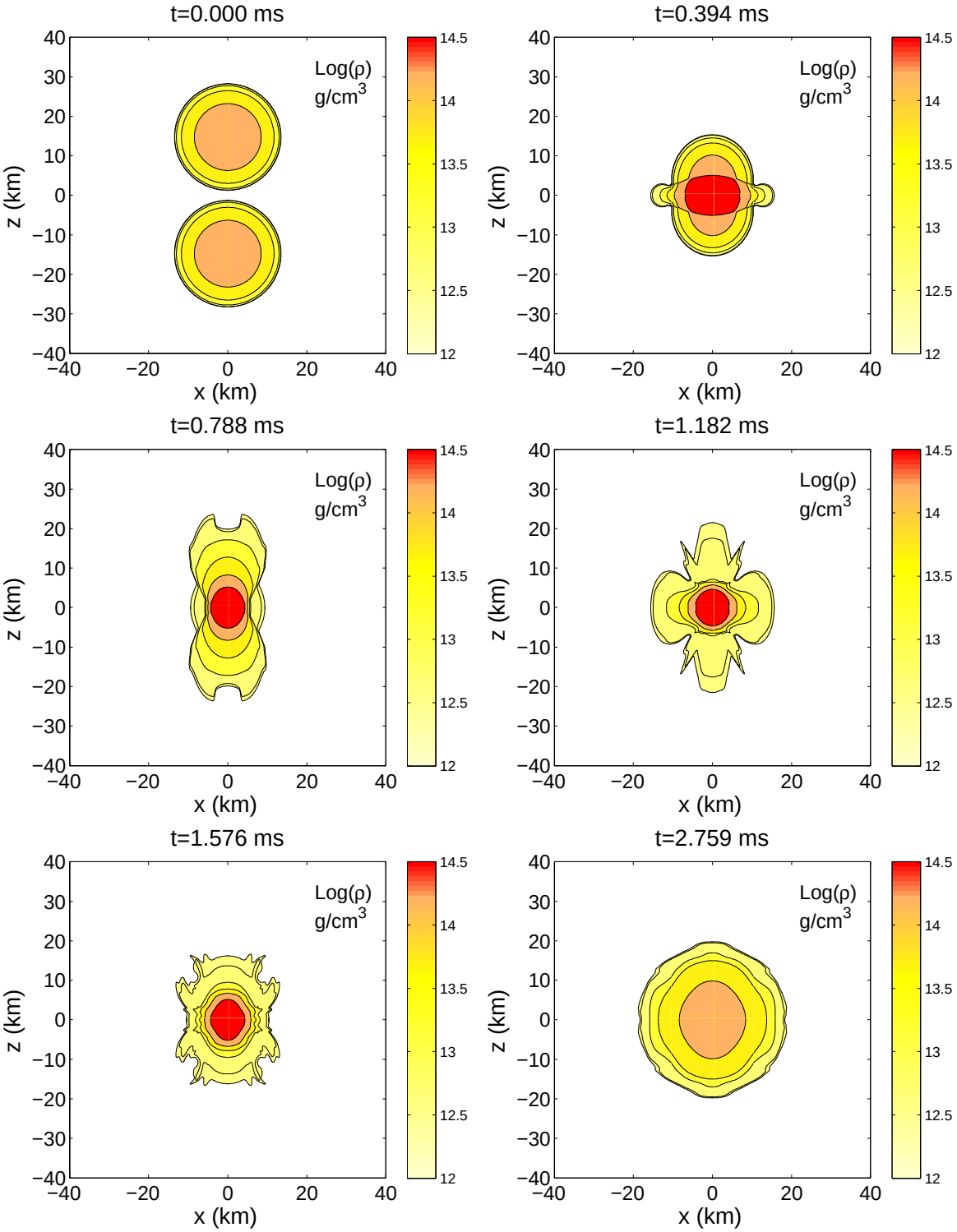

Figure 8.3: The same as figure 8.2, but for the most massive subcritical model ($\rho_c = 0.000579099896670$). The first five frames are similar (although not identical) to the corresponding ones in figure 8.2 since they refer to the metastable evolution when the two solution are essentially indistinguishable. The last frame ($t = 2.759$ ms) shows a new NS produced from the migration of the metastable object to the stable branch of the equilibrium solutions.

The second phase (marked with "B") starts from $t \sim 0.4$ ms and is characterized by strong oscillations around the metastable equilibrium. During these first two phases the subcritical solution and the supercritical one are essentially indistinguishable, but at the end of the second phase, *i.e.* at $t \sim 1.2$ ms, the different nature of the two solutions emerges and the evolutions of the rest-mass density differ. More specifically, during the third phase (marked with "C" and "D"), the supercritical solution shows an exponential increase of the central rest-mass density as a result of the collapse to a black hole. The subcritical solution, on the other hand, shows a violent expansion and the central density settles to a value which is about one tenth of the maximum one attained during the second phase. Clearly, the most interesting part is obviously the one corresponding to the second phase, during which the merged object is a metastable solution in which the central density has strong, non-harmonic oscillations (see inset of figure 8.1).

In order to better describe the dynamics of the system, we show in figures 8.2 and 8.3 the evolution of color-coded contours of the rest-mass density of the supercritical and subcritical solutions, respectively, when shown at representative times in the (x, z) plane. The first row of panels in figure 8.2 shows the initial configuration of the system at time $t = 0$ and a subsequent stage, at time $t = 0.394$ ms, corresponding to when the first maximum in the rest-mass density is reached (*cf.* figure 8.1). This time also represents the one at which the two stellar cores enter in contact and thus marks the beginning of the metastable equilibrium. During this stage, two strong shock waves propagate along the z-direction, ejecting part of the matter as shown in the third panel at time $t = 0.788$ ms. Most of this matter is still gravitationally bound and falls back onto the central object creating a new shock wave (*cf.* fourth panel at $t = 1.182$ ms). This process is then repeated multiple times and results in a sequence of bounces until the object finally collapses to a black hole, as shown in the last panel at time $t = 2.759$ ms and which marks the fate of the supercritical solution.

Similarly, figure 8.3, reports representative stages of the evolution of the subcritical solution. A rapid inspection of the first five panels of figure 8.2 indicates they are very similar to the corresponding ones in figure 8.2. Indeed, the supercritical and subcritical solutions are the same to the precision at which we measure the critical solution [*cf.* (8.1)] and we have reported the panels here exactly to remark the similarity during the first two stages of the evolution. However, being it a subcritical solution, the metastable evolution does not end with a black hole formation but, rather, with a new stable stellar solution. This is shown in the sixth panel of figure 8.3 and refers to a time $t = 2.759$ ms, after the metastable star has expanded violently and when it has reached a new quasi-spherical configuration.

With the exception that we are able to get closer to the critical solution, much of what reported here confirms what found by Jin and Suen in [20]. In the following section, however, we discuss how and why our conclusions about the properties of the critical solutions differ from those discussed in [20] and subsequently in [21].

8.3.2 Nearly-critical solutions

The scope of this section is to show that, contrary to what suggested in [20, 21], the metastable object can be interpreted rather simply as the perturbation of a new equilibrium configurations of linearly unstable spherical stars. To provide evidence that this is the case, we have computed the evolution of the average entropy of the system for a subcritical solution as computed via the volume-averaged polytropic constant (6.14). This is shown in figure 8.4, where we report both $\langle K \rangle$ and the central density ρ_c during the metastable equilibrium or stage "B" (left panel) and when the metastable solution has expanded to recover a stable solution or stage "3" (right panel).

Clearly, the two panels show that two quantities are correlated and indeed in phase opposition – entropy increases when the density decreases and viceversa – as one would expect from the first law

of thermodynamics

$$TdS = pdV + dQ = pdV\,, \tag{8.2}$$

where the second equality comes from assuming adiabatic transformations.

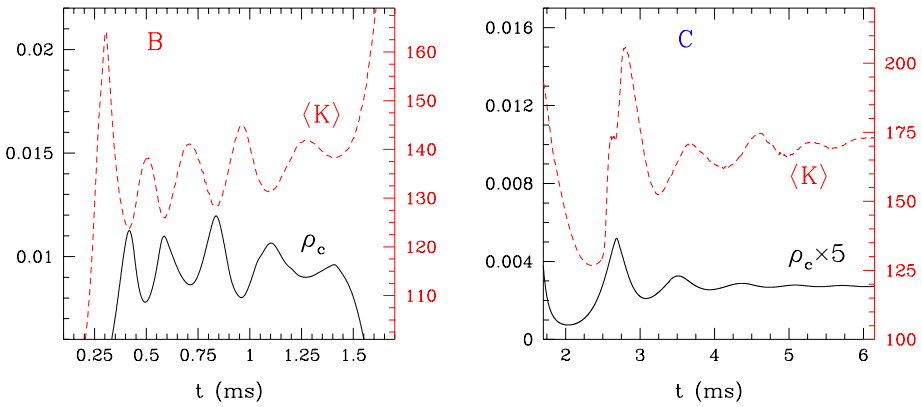

Figure 8.4: *Left panel:* Evolution of the central rest-mass density and of the effective polytropic constant $\langle K \rangle$ for the most massive subcritical model during the metastable equilibrium phase of the dynamics. *Right panel:* The same as in the left panel but during the relaxation to a stable configuration.

Using the results shown in figure 8.4, it is then possible to compute a time-averaged value of $\langle K \rangle$ and of the central density, *i.e.* $\overline{\langle K \rangle}$, $\overline{\rho_c}$, and thus equilibrium polytropic models with such polytropic constant and central density. These equilibrium models can be constructed either relative to the metastable stage or relative to the final stable stage of the subcritical solutions.

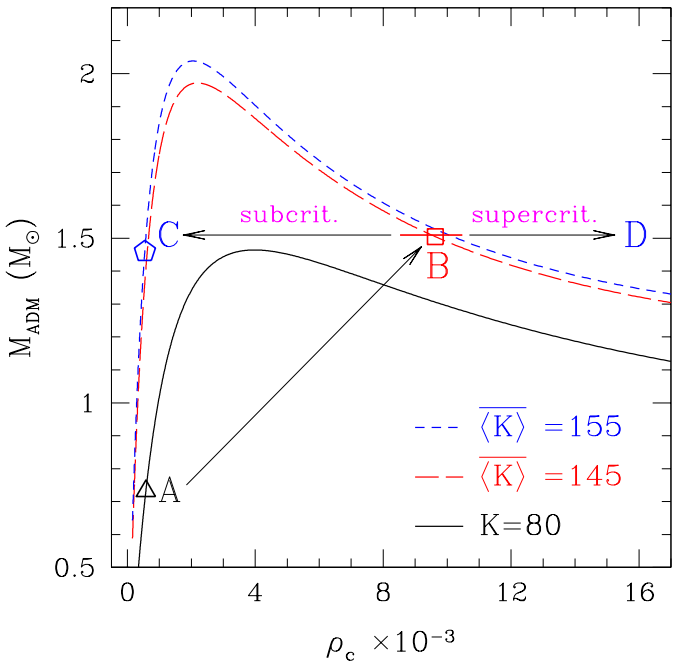

Figure 8.5: Equilibrium sequences of TOV stars with fixed polytropic constant in a standard $(\rho_c, M_{\rm ADM})$ plane. The black solid line refers to a sequence with $K = 80$ and the black triangle marks the initial critical solution (*i.e.* model "A" in table 8.1). The red long-dashed line to a sequence with $\overline{\langle K \rangle} = 145$ and the red square shows the equilibrium model having as central density the time-averaged central density of the metastable solution (*i.e.* model "B" in table 8.1). Finally, the blue dashed line refers to a sequence with $\overline{\langle K \rangle} = 155$ and the blue pentagon shows the equilibrium model having as central density the time-averaged central density of the stable solution (*i.e.* model "C" in table 8.1). All models "A, B, C" have the same rest-mass to a precision of 0.4% and the arrows show how the collision corresponds to a number of transition in the space of configurations.

The results of this procedure are summarized in figure 8.5, which reports the equilibrium sequences of TOV stars with fixed polytropic constant in a standard $(\rho_c, M_{\rm ADM})$ plane. In particular, the black solid line refers to a sequence with $K = 80$ and the black triangle therefore makes the initial critical solution (*i.e.* model "A" in table 8.1). Similarly, the red long-dashed line refers to a sequence with a polytropic constant $\overline{\langle K \rangle} = 145$, which therefore coincides with the time averaged value of K during the metastable state and as deduced from figure 8.4. The red square shows therefore the equilibrium model having as central density the time-averaged central density of the metastable solution (*i.e.* model "B" in table 8.1). Finally, the blue dashed line refers to a sequence with a polytropic constant $\overline{\langle K \rangle} = 155$, which therefore coincides with the time averaged value of K during the stable stage of the subcritical solutions. (*cf.*figure 8.4). The blue pentagon shows therefore the equilibrium model having as central density the time-averaged central density of the stable solution (*i.e.* model "C" in table 8.1). It is important to remark that because models "A, B, C" are determined after fixing the polytropic constant and the central rest-mass density, they are not guaranteed to have the same total baryon mass. In practice, however, they do have the same rest-mass with a precision of 0.4% (of course $2M_{b,A} \simeq M_{b,B} \simeq M_{b,C}$). This is not a coincidence but a clear evidence of the common link among the three models. What is eloquently shown in figure 8.5 can also be stated summarized

Table 8.2: Eigenfrequencies of the modes of the critical solution during the metastable phase of the dynamics as computed from the evolution of the the central rest-mass density. Also indicated are the first overtones of the fundamental mode for a TOV star constructed with K and ρ_c equal to the time-averages of $\langle K \rangle$ and $\langle \rho_c \rangle$ during the metastable phase. Despite the large uncertainty due to the very short integration time, the match between the two set of eigenfrequencies is very good.

Mode	Observed freq. (kHz)	TOV freq. (kHz)
H1	4.8 ± 1.2	3.95
H2	7.2 ± 1.2	6.86
H3	9.6 ± 1.2	9.42
H4	12.0 ± 1.2	11.85

as follows. The head-on collision of two NSs near the critical threshold can be seen as series of transitions in the space of configurations from an initial stable model "A" over to a metastable model "B" which has the same rest-mass but larger gravitational mass as a result of the conversion of the kinetic energy into internal energy via large shocks. Because model "B" is on the linearly unstable branch of the equilibrium configurations, it can exhibit a critical behaviour (this was shown in great detail in paper I) and thus subcritical solutions will expand and move the stable branch of equilibrium solutions (model "C"), while supercritical solutions will collapse to a black hole (solution "D"). In the light of this interpretation, the conclusion drawn by Jin and Suen [20] that the merged object is far from being a TOV because it promptly collapses even though its total rest-mass is smaller than the corresponding maximum mass, does not appear to be the correct one. Indeed, the transition highlighted in figure 8.5 clearly shows that even a sub-massive TOV can be brought over the stability threshold to collapse to black hole by simply increasing its gravitational mass, namely by increasing its internal energy. Additional evidence that the merged object is indeed a perturbed TOV comes from analyzing the oscillation frequencies measured over the metastable stage. Despite the latter is rather short and the eigenfrequencies are consequently not very accurate, they agree well with the ones obtained from the linear perturbation theory for the corresponding TOV model. This is reported in table 8.2, which collects the oscillation frequencies as computed from a Fourier analysis of the central rest-mass density of the largest subcritical solution. Because these frequencies with their error-bars are within the expected ones, we cannot confirm the claim made in [21] that the frequencies of the critical solution are 1 or 2 orders of magnitude smaller than the corresponding equilibrium ones. Rather, we conclude that the metastable critical solution is indeed only a perturbed TOV star.

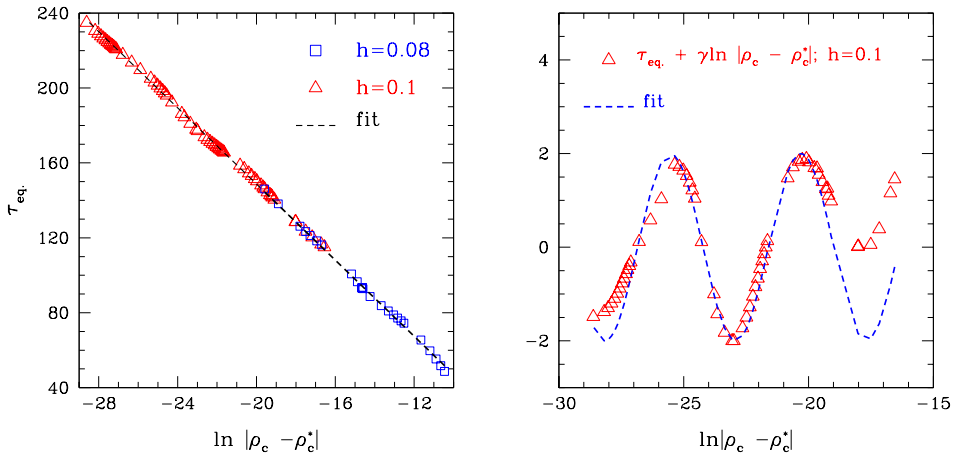

Figure 8.6: *Left panel:* Survival time of the metastable solution plotted against the logarithm of the difference between the initial central density of the stars and the critical one. The red triangles represent the data points obtained with a grid resolution of $h = 0.1$ and the blue squares represent the ones obtained with $h = 0.08$. The black dashed line represents the expected power-law scaling. *Right panel:* Harmonic fluctuations in the critical exponent γ as obtained after subtracting the power-law scaling from the data points computed with $h = 0.1$ (red triangles). Indicated with a blue dashed line is the fitting sine function.

8.3.3 On the critical exponent and its fluctuations

The theory of critical phenomena predicts a precise scaling relation between the survival time of the nearly-critical solutions, namely the time over which a metastable equilibrium exists, and the distance from the critical solution. At lowest order this scaling relation is a simple power-law of the type

$$\tau_{\rm eq} \simeq -\gamma \ln |\rho_c - \rho_c^\star| + \text{const}\,, \tag{8.3}$$

which is derived from equation 6.8. Following [20], we measure the survival time by considering the function $\zeta(t) = (\alpha - \alpha^\star)/\alpha^\star$, where α is the lapse function at the coordinate origin of a given simulation and $\alpha^\star$ is the lapse of the best numerical approximation of the critical solution. We set $\tau_{\rm eq}$ to be the first (coordinate) time at which $\zeta(\tau_{\rm eq}) \geq 0.05$; as discussed in [20], the determination of the critical exponent does not depend sensitively on this cut-off time. Finally, we compute γ performing a linear least-square fit of (8.3) on the data points. The results of this process are shown in the left panel of figure 8.6, where we report with red triangles the values of $\tau_{\rm eq}$ as computed from about 60 simulations having different initial central density. As we will discuss below, such a large number of data points is necessary not only to measure accurately the exponent γ, but also to determine whether nonlinear corrections to expression (8.3) should be considered. In this way we have computed the critical exponent to be $\gamma = 10.004$, which agrees within 8.4%, with the value computed by [20]. As a further validation, we have computed the critical exponent also for a (smaller) set of simulations carried out at a higher resolution (*i.e.* $h = 0.08$ vs $h = 0.1$) and these are shown as blue squares. These higher-resolution simulations predict a critical exponent of 10.303, thus with a difference of 2.9% from the lower-resolution ones. A more careful analysis of the data for the survival time reveals that relation (8.3) is well reproduced by the data, but also that the latter show additional, fine-structure features which are are not accounted for in (8.3). In particular, it is apparent already at a visual inspection that the critical exponent also shows a periodic change as the solution approaches the

critical one. This is highlighted in the right panel of figure 8.6, where we show the deviations of the data from the relation (8.3), and where it is apparent that these deviations are essentially harmonic in the range in which data is available (to have a single fitting function the panel does not contain the higher-resolution data). As a result, we can correct the scaling relation (8.3) with a simple expression of the type

$$\tau_{\rm eq} \simeq -\gamma \ln|\rho_c - \rho_c^\star| + c_1 \sin\left(c_2 \ln|\rho_c - \rho_c^\star| + c_3\right) + \text{const}\,. \tag{8.4}$$

where $c_1 \simeq 2.0$, $c_2 \simeq 1.2$ and $c_3 \simeq 0.8$. Interestingly, this fine structure of the time-scaling relation has been observed also in in the critical collapse of scalar fields [22, 23], but has never been reported before for perfect fluids, although it may be present also in the data of [20] (*cf.* their figure 4). Because the scaling relation (8.3) is derived after performing a linear analysis near the critical solution [13], the additional oscillation captured in expression (8.4) is a purely nonlinear effect which has not been yet fully explained.

8.4 Metastable solutions and the hoop conjecture

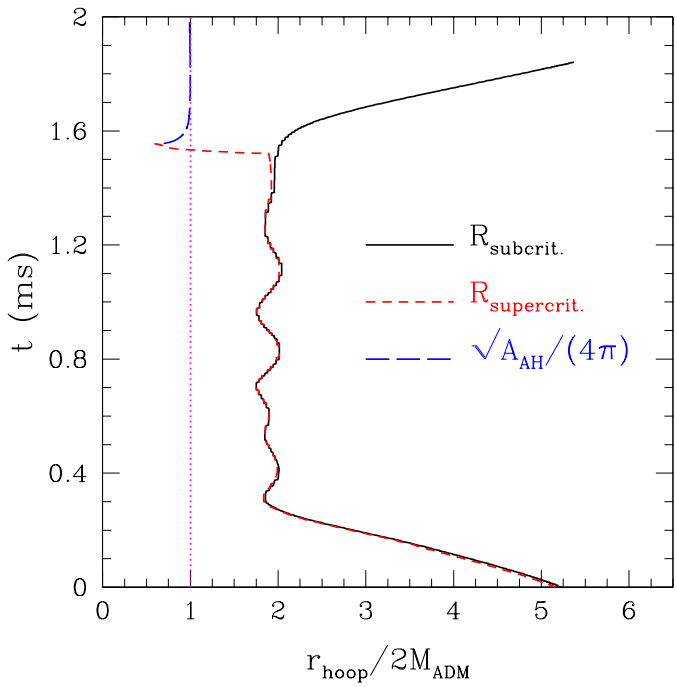

Figure 8.7: Spacetime diagram showing the world-lines of the proper stellar radius for either a subcritical solution $R_{\rm subcrit.}$ (black solid line) or for a supercritical solution $R_{\rm supercrit.}$ (red dashed line). Both quantities are expressed in units of twice the ADM mass, so that the vertical dotted line at 1 represents the threshold below which the hoop conjecture would be violated (the time coordinate is the proper time of an observer comoving at R). Also indicated with a blue long-dashed line is the world-line of the apparent horizon which is relevant in the case of the supercritical solution. Note that the metastable solution is always outside its "hoop".

As discussed in the main text, near the critical solution and during the metastable stage, the evolution of all the hydrodynamical and field variables is essentially the same (to a precision which is

proportional to the distance from the critical solution) for both subcritical and supercritical solutions. It is therefore natural to ask whether the metastable solution, which can either produce a black hole or an expanded star, is ever compact enough to violate the hoop conjecture. We recall that the conjecture states that a black hole is formed if and only if a "mass" M of matter is confined in a hoop of radius which is in every direction is smaller or equal to the corresponding Schwarzschild radius. Stated differently, a black hole is expected to form if the matter is enclosed in a hoop of proper circumference $\mathcal{C} \leq 4\pi M$. The hoop conjecture, as it was originally formulated, is not meant to be a precise mathematical statement [115], even though it can be made precise under particular circumstances [116–118]. Most importantly, it is meant mostly as a qualitative description of the gravitational collapse due to the compression of matter. In particular the conjecture leaves much freedom in the definition of both $\mathcal{C}$ and M. In view of this freedom, we have taken $\mathcal{C}$ to be the proper circumference of a coordinate circle enclosing $95\ \%$ of the mass of the system (in order to exclude the extended low-density regions) and used the ADM mass within $\mathcal{C}$ as a local measure of the mass (This use of the ADM mass is strictly speaking incorrect as such a mass is well defined only at spatial infinity; however it provides an approximation which is adequate for the quality of the arguments made here). In figure 8.7 we show in a spacetime diagram the world-lines of the proper stellar radius for either a subcritical solution $R_{\rm subcrit.}$ (black solid line) or for a supercritical solution $R_{\rm supercrit.}$ (red dashed line). Both quantities are expressed in units of twice the ADM mass, so that the vertical dotted line at 1 represents the threshold below which the hoop conjecture would be violated (the time coordinate is the proper time of an observer comoving at R). Also indicated with a blue long-dashed line is the world-line of the apparent horizon which is relevant in the case of the supercritical solution. Quite clearly the metastable solution is always outside its "hoop" (indeed about twice as large) and when the supercritical solution crosses it is to produce a black hole as the conjecture predicts. It remains unclear how these world-lines would evolve if we had considered stars with larger boosts or that are are far from the critical solution. These questions will be addressed in our future work on the subject. As a final remark we note that if we had used the interpretation of the head-on collision as a transition between a stable and a metastable TOV solution (*i.e.* the one summarized in figure 8.5), then it would have been rather obvious that the hoop conjecture cannot be violated: a TOV star has a surface which is always outside of its Schwarzschild radius.

Chapter 9

Conclusion

A number of astrophysical scenarios can be very conveniently studied numerically by assuming they possess and preserve a rotation symmetry around an axis. Such an assumption reduces the number of spatial dimensions to be considered and thus the computational costs. This, in turn, allows for a more sophisticated treatment of the physical and astrophysical processes taking place and, as a result, for more realistic simulations.

During this thesis work we have developed `Whisky2D`, a new numerical code developed to solve in Cartesian coordinates the full set of general relativistic hydrodynamics equations in a dynamical space-time and in axisymmetry. `Whisky2D` has been built with the intent of of adding it to the *Whisky Astrophysical laboratory*, to investigate a number of astrophysical objects, which possess and preserve an overall cylindrical symmetry. More specifically, the new code solves the Einstein equations by using the *"cartoon"* method, while HRSC schemes are used to solve the hydrodynamic equations written in a conservative form. An important feature of the code is the use of a novel formulation of the equations of relativistic hydrodynamics in cylindrical coordinates. More specifically, by exploiting a suitable definition of the conserved variables, we removed from the source of the flux-conservative equations those terms that presented coordinate singularities at the axis and that are usually retained in the standard formulation of the equations. Despite their simplicity, the changes made to the standard formulation can produce significant improvements on the overall accuracy of the simulations with a truncation error which is often several orders of magnitude smaller. In order to assess the validity of the new formulation and compare its accuracy with that of the formulation which is most commonly used in Cartesian coordinates, we have performed several tests involving the evolution of oscillating spherical and rotating stars, as well as shock-tube tests. In all cases considered we have shown that the codes implementing the two formulations yield the expected convergence rate but also that the new formulation is always more accurate, often considerably more accurate, than the standard one.

This additional degree of accuracy has allowed us to study a number of aspects of critical phenomena. We recall that critical phenomena are ubiquitous in many different branches of physics and are of great interest in general relativity where they are associated with phase transition of families of solutions. Particularly interesting are critical phenomena in gravitational collapse and in the more specific context of the dynamics of NSs, type-I critical phenomena have seen a renewed interested when it was shown that a critical behaviour of this type is produced in the in head-on collision of NSs [20] or in the dynamics of rotating magnetized stars [18]. With the goal of studying in more detail the occurrence of type-I critical collapse in NSs, we have therefore employed the `Whisky2D`

code to study a large set of spherical stellar models having a constant baryon mass. Differently from what done before by other authors, *e.g.* [15, 17], we have considered stellar models that are on the "right" branch of the models of equilibrium and thus linearly *unstable*. Using a simple ideal-fluid EOS and very small perturbations which are entirely induced by the truncation error, we have found that our family of initial data exhibits a clear type-I critical behaviour at at a threshold central rests-mass density of $\rho_c^\star = 0.004593224802 \pm 2.1 \times 10^{-12}$ and with a critical exponent $\lambda = 0.02149665$. These results thus confirm the conclusions reached by Liebling et al. [18] but also provide a more quantitative determination of the threshold and of the nature of the critical scaling. Exploiting in fact the relative simplicity of our system, we were able carry out a more in-depth study providing solid evidences of the criticality of this phenomenon and also to give a simple interpretation of the putative critical solution as a spherical solution with the unstable mode being the fundamental F-mode. As a result, we have shown that for any choice of the polytropic constant, the critical solution distinguishes the set of subcritical models migrating to the stable branch of the models of equilibrium from the set of supercritical models collapsing to a black hole. Furthermore, we have studied how the dynamics changes when the numerically perturbation is replaced by a finite-size, resolution-independent velocity perturbation and show that in such cases a nearly-critical solution can be changed into either a sub or supercritical. Finally, the work presented here here is of direct help in understanding why the critical behaviour shown in the head-on collision of two neutron stars is indeed of type-I and why it can be explained simply in terms of the creation of a metastable stellar model on the unstable branch of equilibrium solutions [24].

As an additional scenario in which to use the `Whisky2D` code to study critical phenomena we have considered the head-on collision of equal mass, non-rotating NSs boosted towards each other. After fixing the initial velocity of the stars, we evolved numerically a great number of configurations with different initial central rest-mass density. Overall, the basic dynamics of the process is rather simple: As the two NSs are accelerate towards each other, they collide leading to a merged object which is wildly oscillating and with a gravitational mass which is above the maximum mass of the initial configuration. Depending on whether the initial central rest-mass density is larger or smaller than the critical one, the metastable solution either collapses to a black hole (supercritical solutions) or expands to a new stable stellar solution (subcritical solutions). Exploiting the accuracy of the code and the large set of initial configurations considered, we were able we are able to identify the critical value for the central density with an accuracy of 11 significant digits, a level of precision never achieved before in this type of study. Much of the results found coincide and confirm those found by Jin and Suen in [20, 21]. However, we do differ and significantly when it comes to the interpretation of the critical solutions. More specifically we have shown that the head-on collision of two NSs near the critical threshold can be seen as series of transitions in the space of configurations from an initial stable model over to a metastable one with the same rest-mass but larger gravitational mass as a result of the conversion of the kinetic energy into internal energy via large shocks. The metastable solution is on the linearly unstable branch of the equilibrium configurations and thus it can exhibit a critical behaviour (see [19]) and either move the stable branch of equilibria (subcritical solutions), or will collapse to a black hole (supercritical solutions). Hence, the critical solution is indeed a (perturbed) TOV solution, in contrast with the conclusions drawn in [20, 21]. With the calculation of $\langle K \rangle$ at any time step (see figure 8.4) have shown a way to follow a an important thermodynamical quantity, which is related to the entropy (6.13). The continuous growing of $\langle K \rangle$ coincides with second law of thermodynamics. Finally, we have also computed the critical exponent of the scaling relation of type-I critical phenomena and found it to agree well with the one computed by [20]. However, we have also found that, superimposed with the standard power-law, the scaling law shows a fine

structure in terms of a periodic fluctuation. These wiggles in the critical exponent have already been observed in the case of type-II critical collapse of massless scalar fields [22, 23], but were never reported before in the case of perfect fluids.

The work on the topics of this thesis gave many new insights in questions of numerical methods, as well as in a number of physical problems. We learned a little bit more about the rays of the light, which project the shadows of puppets of the puppeteer on the wall of our cave [119]. The universes still contains an endless number of unexplored miracles and we should never stop to watch in the eyes of the big magician [1] [120], to ask for an answer.

[1] It is like watching a magic trick. We cannot understand how it is done. So we ask: how can the magician change a couple of white silk scarves into a live rabbit?
A lot of people experience the world with the same incredulity as a when a magician suddenly pulls a rabbit out of a hat which ha just been shown to them empty. In the case of the rabbit, we know the magician hat tricked us. What we would like to know is just how he did it. But when it comes to the world it is somewhat different. We know that the world is not all sleight of hand and deception because here we are in it, we are in it, we are part of it. Actually, we are the white rabbit being pulled out of the hat. The only difference between us and the white rabbit is that the rabbit does not realise it is taking part in a magic trick. Unlike us. We feel we are part of something mysterious and we would like to know how it all works. As far as the white rabbit is concerned, it might be better to compare it with the whole universe. We who live here are microscopic insect existing deep down in the rabbit's fur. But philosopher are always trying to climb up the fine hairs of the fur in order to stare right into the magician's eyes.

Part VI

Appendix

Appendix A

Units and unit conversion

Table A.1: Fundamental physical constants

Constant	Symbol	Value
Speed of light	c	$2.99792458 \cdot 10^{8}$ cm $\quad$ s^{-1}
Gravitational constant	G	$6.67428 \cdot 10^{-11}$ m^3 $\quad$ kg^{-1} $\quad$ s^{-2}
Planck constant	$\hbar$	$1.054571628 \cdot 10^{-34}$ kg $\quad$ m^2 $\quad$ s^{-1}

Table A.2: Table shows the basic Planck units

Name	Dimension	Term	Value
Planck mass	M	$m_p = \sqrt{\hbar c/G}$	$2.17644 \cdot 10^{-8}$ kg
Planck length	L	$l_p = \sqrt{\hbar G/c^3}$	$1.61625 \cdot 10^{-35}$ m
Planck time	T	$t_p = l_p/c$	$5.39124 \cdot 10^{-44}$ s
Planck area	A	$a_p = l_p^2$	$2.61227 \cdot 10^{-70}$ m^2

Table A.3: Physical constants in units in cgs, geometric and $c = G = M_\odot = 1$ units

Dimension/ Quantity	cgs	Geometric	$c = G = M_\odot = 1$
Time	1 s	$3.33564095198 \cdot 10^{-11}$ cm	$2.0296 \cdot 10^{5}$
Length	1 cm	1 cm	$6.7706 \cdot 10^{-6}$
Mass	1 g	$7.4261 \cdot 10^{-29}$ cm	$5.0279 \cdot 10^{34}$
Density	1 g cm^{-3}	$7.4261 \cdot 10^{-29}$ cm^{-2}	$1.6199 \cdot 10^{-18}$
Energy	1 erg = 1 g cm^2 s^{-2}	$8.2627 \cdot 10^{-50}$ cm	$5.5953 \cdot 10^{-55}$
Specific internal energy	1 erg g^{-1}	$1.11265005605 \cdot 10^{21}$	$1.11265005605 \cdot 10^{21}$
Solar mass	$1.9891 \cdot 10^{33}$ g	$1.4772 \cdot 10^{5}$ cm	1.0
Speed of light	$2.99792458 \cdot 10^{10}$ cm s^{-1}	1.0	1.0
Pressure	1 dyn cm^{-2}	$6.6742 \cdot 10^{-8}$	$1.8063 \cdot 10^{-39}$

Appendix B

About the ”Cartoon“ method

In what follows we recall the essential features of the *“cartoon”* method for the solution of the field equations in Cartesian coordinates. Consider therefore the computational domain to have extents $0 \leq x, z \leq d_{max}$ and $-\Delta y \leq y \leq \Delta y$, where d_{max} refers to the location of the outer boundary. Reflection symmetry with respect to the $z = 0$-plane can additionally be assumed. The Einstein equations are then solved only on the $y = 0$-plane with the derivatives in the y-direction being computed with second-order centred stencils using the points at $-\Delta y,\ 0\ , \Delta y$.
Taking into account axisymmetry, the rotation in the (x, y) plane is defined as

$$R(\phi)^{i}_{j} = \begin{pmatrix} \cos(\phi) & -\sin(\phi) & 0 \\ \sin(\phi) & \cos(\phi) & 0 \\ 0 & 0 & 1 \end{pmatrix}, \tag{B.1}$$

where $R(\phi)^{-1} = R(-\phi)$ and the rotation angle is defined as $\phi = \tan^{-1}(\pm\Delta y/\sqrt{x^2 + (\Delta y)^2})$.
As commented in the main text, the values of all the quantities on the $\pm\Delta y$ planes are computed via rotations of the corresponding values on the $y = 0$-plane. More specifically, the components of an arbitrary vector field T_i on the $\pm\Delta y$ planes are computed via a ϕ-rotation as

$$T_x = T^{(0)}_x \cos(\phi) - T^{(0)}_y \sin(\phi)\,, \tag{B.2}$$

$$T_y = T^{(0)}_x \sin(\phi) + T^{(0)}_y \cos(\phi)\,, \tag{B.3}$$

$$T_z = T^{(0)}_z\,, \tag{B.4}$$

where $T^{(0)}_i$ denote the corresponding components at $(\sqrt{x^2 + (\Delta y)^2}, 0, z)$, which are computed via a Lagrangian interpolation from the neighboring points on the x-axis. Similarly, the components of an arbitrary tensor field T_{ij} tensor will be computed as

$$T_{xx} = T^{(0)}_{xx} \cos^2(\phi) - T^{(0)}_{xy} \sin(2\phi) + T^{(0)}_{yy} \sin^2(\phi)\,, \tag{B.5}$$

$$T_{xy} = \frac{1}{2} T^{(0)}_{xx} \sin(2\phi) - T^{(0)}_{xy} \cos(2\phi) + \frac{1}{2} T^{(0)}_{yy} \sin(2\phi)\,, \tag{B.6}$$

$$T_{yy} = T^{(0)}_{xx} \sin^2(\phi) - T^{(0)}_{xy} \sin(2\phi) + T^{(0)}_{yy} \cos^2(\phi)\,, \tag{B.7}$$

$$T_{xz} = T^{(0)}_{xz} \cos(\phi) - T^{(0)}_{yz} \sin(\phi)\,, \tag{B.8}$$

$$T_{yz} = T^{(0)}_{xz} \sin(\phi) + T^{(0)}_{yz} \cos(\phi)\,, \tag{B.9}$$

$$T_{zz} = T^{(0)}_{zz}\,. \tag{B.10}$$

Appendix C

Eigenstructure of the relativistic hydrodynamic equations

The knowledge about the eigenstructure is required by the approximate Riemann solvers (HLLE and Marquina) implemented in `Whisky2D`. The Eigenvalues are calculated by the 5×5 Jacobian Matrices of the system hydrodynamic equations

$$\hat{A}^{(i)} = \frac{\partial(\sqrt{\gamma}\mathbf{F}^i)}{\partial(\sqrt{\gamma}\mathbf{F}^0)} = \frac{\partial\mathbf{F}^i}{\partial\mathbf{F}^0} \tag{C.1}$$

The eigenvalues of the Jacobian $\mathbf{A^i}$ are, for example along th x direction,

$$\lambda_0 = \alpha v^x - \beta^x \qquad (\text{triple eigenvalue}), \tag{C.2}$$

$$\lambda_\pm = \frac{\alpha}{1-v^2c_s^2}\left\{v^x(1-c_s^2) \pm c_s\sqrt{(1-v^2)[\gamma^{xx}(1-v^2c_s^2)-v^xv^x(1-c_s^2)]}\right\} - \beta^i \tag{C.3}$$

and a complete set of its right eigenvectors is

$$\mathbf{R}^{(01)} = \begin{bmatrix} \frac{\mathcal{K}}{hW} \\ v_x \\ v_y \\ v_z \\ 1-\frac{\mathcal{K}}{hw} \end{bmatrix}, \qquad \mathbf{R}^{(02)} = \begin{bmatrix} Wv_y \\ h(\gamma_{xy}+2W^2v_xv_y) \\ h(\gamma_{yy}+2W^2v_yv_y) \\ h(\gamma_{zy}+2W^2v_xv_y) \\ Wv_y(2hW-1) \end{bmatrix},$$

$$\mathbf{R}^{(03)} = \begin{bmatrix} Wv_z \\ h(\gamma_{xz}+2W^2v_xv_z) \\ h(\gamma_{yz}+2W^2v_yv_z) \\ h(\gamma_{zz}+2W^2v_zv_z) \\ Wv_z(2hW-1) \end{bmatrix}, \qquad \mathbf{R}^{(\pm)} = \begin{bmatrix} 1 \\ hW(v_x-\mathcal{V}^x_\pm) \\ hWv_y \\ hWv_z \\ hW\mathcal{A}^x_\pm - 1 \end{bmatrix} \tag{C.4}$$

where c_s is the local sound speed (which can be obtained from $hc_s = \varkappa + \kappa p/\rho^2$ with $\varkappa \equiv \partial p/\partial\rho$ and $\kappa \equiv \partial p/\partial\epsilon$), $\mathcal{K} \equiv \tilde{\kappa}/(\tilde{\kappa}-c_s^2), \tilde{\kappa} \equiv \kappa/\rho$ and

$$\mathcal{V}^x_\pm \equiv \frac{v^x-\Lambda^x_\pm}{\gamma^{xx}-v^x\Lambda^x_\pm}, \qquad \mathcal{A}^x_\pm \equiv \frac{\gamma^{xx}-v^xv^x}{\gamma^{xx}-v^x\Lambda^x_\pm}, \qquad \Lambda^i_\pm \equiv \frac{\lambda_\pm+\beta^i}{\alpha}. \tag{C.5}$$

Similarly, the eigenvalues of $\mathbf{A}^{(z)}$ are the same as in expression (C.2) with z in place of x and the corresponding right eigenvectors ant the same as in (C.4) with the second row exchanged with the fourth and with the interchange $x \leftrightarrow y$ or $x \leftrightarrow z$ respectively. Since the left eigenvectors are effectively used in the code in the Marquina solver in order to compute the characteristic variables, we give the explicit expression for them too [121]:

$$\mathbf{L}^{(01)} = \frac{W}{\mathcal{K}-1}\begin{bmatrix} h-W \\ Wv^x \\ Wv^y \\ Wv^z \\ -W \end{bmatrix}, \qquad \mathbf{L}^{(02)} = \frac{1}{h\xi}\begin{bmatrix} -\gamma_{zz}y_y + \gamma_{yz}v_z \\ v^x(\gamma_{zz}v_y - \gamma_{yz}v_z) \\ \gamma_{zz}(1-v_xv^x) + \gamma_{xz}v_zv^x \\ \gamma_{yz}(1-v_xv^x) + \gamma_{xz}v_yv^x \\ -\gamma_{zz}v_y + \gamma_{yz}v_z \end{bmatrix},$$

$$\mathbf{L}^{(03)} = \frac{1}{}h\xi\begin{bmatrix} -\gamma_{yy}v_z + \gamma_{yz}v_y \\ v^x(\gamma_{yy}y_z - \gamma_{yz}v_y) \\ -\gamma_{yz}(1-v_xv^x) + \gamma_{xy}v_zv^x \\ \gamma_{yy}(1-v_xv^x) + \gamma_{xy}v_yv^x \\ -\gamma_{yy}v_z + \gamma_{yz}v_y \end{bmatrix},$$

$$\mathbf{L}^{(\mp)} = \pm\frac{h^2v^x}{\Delta}\begin{bmatrix} hW\mathcal{V}^x_\pm\xi + l^{(5)}_\mp \\ \Gamma_{xx}(1-\mathcal{K}A^x_\pm) + (2\mathcal{K}-1)\mathcal{V}^x_\pm(W^2v^x\xi - \Gamma_{xx}v^x) \\ \Gamma_{xy}(1-\mathcal{K}A^x_\pm) + (2\mathcal{K}-1)\mathcal{V}^x_\pm(W^2v^y\xi - \Gamma_{xy}v^x) \\ \Gamma_{xz}(1-\mathcal{K}A^x_\pm) + (2\mathcal{K}-1)\mathcal{V}^x_\pm(W^2v^z\xi - \Gamma_{xz}v^x) \\ (\mathcal{K}-1)[-\gamma v^x + \mathcal{V}^x_\pm(W^2\xi - \Gamma_{xx})] - \mathcal{K}W\mathcal{V}^x_\pm\xi \end{bmatrix}, \quad \text{(C.6)}$$

where $\Gamma_{xx} \equiv \gamma_{yy}\gamma_{zz} - \gamma^2_{yz}, \xi \equiv \Gamma_{xx} - \gamma^x_v v^x$ and $\Delta \equiv h^3W(\mathcal{K}-1)\xi(\mathcal{A}^x_+ - \mathcal{A}^x_-)$.

Appendix D

Shock test

Already in chapter (5) we discussed a shock problem. The shock was result of a fast inward going matter, which is reflected at the symmetry axis. To complete the list of important shock tests, we show the results of the standard test of shock tube evolution (see table D.1).

We calculate the evolution of the shock initial data with PPM reconstruction and the Marquina Riemann Solver.

Figures (D.1) and (D.1) show a comparison of the shock problem after 0.13 ms to the exact solution [78, 79, 122].

In detail figure (D.1) shows the evolution of shock front in the z-direction of the cylindrical grid. Because of the properties of this cylindrical coordinates the shock behaves like in a Cartesian grid.

The shock front in figure (D.1) shows indeed a difference form the exact solution. This is due to the geometrical properties of the cylindrical grid in r-direction. In a Cartesian coordinates grid lines are parallel. In cylindrical coordinates two grid lines along r-direction are not parallel, the distance between them grows. The area which is covered by a shock front grows with the distance from the origin, if the shock runs along the r-direction and the shape of the shock changes.

Table D.1: Initial properties of shock tube evolution. The different columns refer to the direction h of the evolution of the shock, the size of the grid, the maximum and minimum initial density, the maximum and minimum initial pressure and the initial velocity. All models have been computed with a ideal fluid EOS with $\Gamma = 2.0$.

direction	h ($M_\odot$)	ρ_{max}	ρ_{min}	p_{max}	p_{min}	v_{init}
z	0.00125	10	1	13.3	10^{-6}	0.0
r	0.00125	10	1	13.3	10^{-6}	0.0

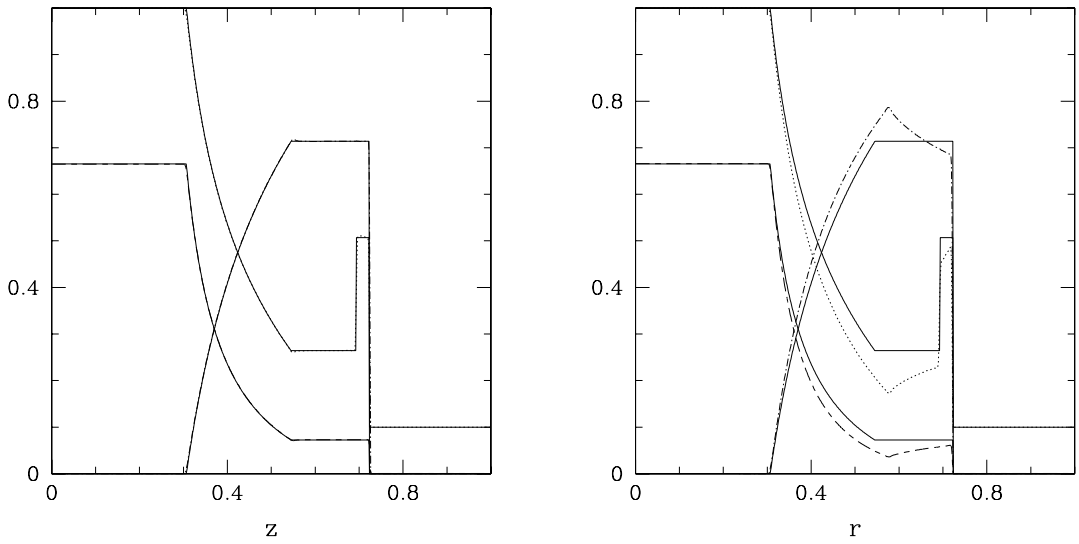

Figure D.1: The left picture shows the evolution of a shock-tube after 0.13 ms. The dotted line shows the evolution of the density profile. The long-short dashed line shows the evolution of the pressure and the dotted-dashed line the velocity. The shock evolves along the z-direction of cylindrical grid. The right picture shows the evolution of a shock-tube after 0.13 ms. The dotted line shows the evolution of the density profile. The long-short dashed line shows the evolution of the pressure and the dotted-dashed line the velocity. The shock evolves along the r-direction of cylindrical grid.

Bibliography

[1] Kant I 1788 *Critique of Practical Reason* (Longmans, Green, and Co.)

[2] Alcubierre M, Brandt S R, Brügmann B, Holz D, Seidel E, Takahashi R and Thornburg J 2001 *Int. J. Mod. Phys. D* **10** 273–289

[3] Shibata M 2000 *Prog. Theor. Phys.* **104** 325–358

[4] Shibata M 2003 *Phys. Rev. D* **67** 024033

[5] Montero P J 2004 *Accretion Tori arround Black Holes* Ph.D. thesis SISSA, International School for advanced studies

[6] Duez M D, Liu Y T, Shapiro S L and Stephens B C 2005 *Phys. Rev. D* **72** 024028

[7] Shibata M and Sekiguchi Y 2005 *Phys. Rev. D* **72** 044014

[8] Montero P J, Font J A and Shibata M 2008 *Phys. Rev. D* **78** 064037

[9] Kellerman T, Baiotti L, Giacomazzo B and Rezzolla L 2008 *Classical and Quantum Gravity* **25** 225007

[10] Choptuik M W 1993 *Phys. Rev. Lett.* **70** 9

[11] Gundlach C and Martín-García J 2007 *Living Reviews in Relativity* **10** 5

[12] Evans C R and Coleman J S 1994 *Phys. Rev. Lett.* **72** 1782–1785

[13] Hara T, Koike T and Adachi S 1996 *ArXiv General Relativity and Quantum Cosmology e-prints*

[14] Brady P, Choptuik M, Gundlach C and Neilsen D 2002 *Class. Quantum Grav.* **19** 6359–6375

[15] Novak J 2001 *Astron. Astrophys.* **376** 606 URL `http://www.citebase.org/abstract?id=oai:arXiv.org:gr-qc/0107045`

[16] Noble S C 2003 *A Numerical Study of Relativistic Fluid Collapse* Ph.D. thesis University of Texas at Austin (*Preprint* `gr-qc/0310116v1`) URL `http://www.citebase.org/abstract?id=oai:arXiv.org:gr-qc/0310116`

[17] Noble S C and Choptuik M W 2008 *Physical Review D* **78** 064059

[18] Liebling S L, Lehner L, Neilsen D and Palenzuela C 2010 Evolutions of magnetized and rotating neutron stars (*Preprint* `1001.0575v1`) URL `http://www.citebase.org/abstract?id=oai:arXiv.org:1001.0575`

[19] Radice D, Rezzolla L and Kellerman T 2010 *Classical and Quantum Gravity submitted*

[20] Jin K J, Suen W M and et al 2007 *Phys. Rev. Lett* **98** 131101

[21] Wan M B, Jin K J and Suen W M 2008 Dynamical analysis of the structure of neutron star critical collapses (*Preprint* `0807.1710v2`) URL `http://www.citebase.org/abstract?id=oai:arXiv.org:0807.1710`

[22] Gundlach C 1997 *Phys. Rev. D* **55** 695

[23] Hod S and Piran T 1997 *Physical Review D* **55** 440

[24] Kellermann T, Rezzolla L and Radice D 2010 *Classical and Quantum Gravity submitted*

[25] Arnowitt R, Deser S and Misner C W 1962 *Gravitation: An introduction to current research* ed Witten L (New York: John Wiley) pp 227–265 (*Preprint* `gr-qc/0405109`)

[26] Richtmyer R D and Morton K 1967 *Difference Methods for Initial Value Problems* (New York: Interscience Publishers)

[27] York J W 1979 *Sources of gravitational radiation* ed Smarr L L (Cambridge, UK: Cambridge University Press) pp 83–126

[28] Cook G B, Huq M F, Klasky S A, Scheel M A, Abrahams A M, Anderson A, Anninos P, Baumgarte T W, Bishop N, Brandt S R, Browne J C, Camarda K, Choptuik M W, Correll R R, Evans C R, Finn L S, Fox G C, Gómez R, Haupt T, Kidder L E, Laguna P, Landry W, Lehner L, Lenaghan J, Marsa R L, Masso J, Matzner R A, Mitra S, Papadopoulos P, Parashar M, Rezzolla L, Rupright M E, Saied F, Saylor P E, Seidel E, Shapiro S L, Shoemaker D, Smarr L, Suen W M, Szilágyi B, Teukolsky S A, van Putten M H P M, Walker P, Winicour J and York Jr J W 1998 *Phys. Rev. Lett.* **80** 2512–2516

[29] Abrahams A M, Rezzolla L, Rupright M E, Anderson A, Anninos P, Baumgarte T W, Bishop N T, Brandt S R, Browne J C, Camarda K, Choptuik M W, Cook G B, Correll R R, Evans C R, Finn L S, Fox G C, Gómez R, Haupt T, Huq M F, Kidder L E, Klasky S A, Laguna P, Landry W, Lehner L, Lenaghan J, Marsa R L, Massó J, Matzner R A, Mitra S, Papadopoulos P, Parashar M, Saied F, Saylor P E, Scheel M A, Seidel E, Shapiro S L, Shoemaker D, Smarr L, Szilágyi B, Teukolsky S A, van Putten M H P M, Walker P, Winicour J and J W York J 1998 *Phys. Rev. Lett.* **80** 1812–1815

[30] Gómez R, Lehner L, Marsa R, Winicour J, Abrahams A M, Anderson A, Anninos P, Baumgarte T W, Bishop N T, Brandt S R, Browne J C, Camarda K, Choptuik M W, Cook G B, Correll R, Evans C R, Finn L S, Fox G C, Haupt T, Huq M F, Kidder L E, Klasky S A, Laguna P, Landry W, Lenaghan J, Masso J, Matzner R A, Mitra S, Papadopoulos P, Parashar M, Rezzolla L, Rupright M E, Saied F, Saylor P E, Scheel M A, Seidel E, Shapiro S L, Shoemaker D, Smarr L, Szilágyi B, Teukolsky S A, van Putten M H P M, Walker P and York Jr J W 1998 *Phys. Rev. Lett.* **80** 3915–3918

[31] Schnetter E 2003 *Gauge fixing for the simulation of black hole spacetimes* Ph.D. thesis Universität Tübingen Tübingen, Germany URL `http://w210.ub.uni-tuebingen.de/dbt/volltexte/2003/819/`

[32] Bonazzola S, Gourgoulhon E, Grandclement P and Novak J 2004 *Phys. Rev. D* **70** 104007

[33] Nakamura T, Oohara K and Kojima Y 1987 *Prog. Theor. Phys. Suppl.* **90** 1–218

[34] Shibata M and Nakamura T 1995 *Phys. Rev. D* **52** 5428

[35] Baumgarte T W and Shapiro S L 1998 *Phys. Rev. D* **59** 024007

[36] Shibata M, Baumgarte T W and Shapiro S L 2000 *Phys. Rev. D* **61** 044012

[37] Alcubierre M, Allen G, Brügmann B, Seidel E and Suen W M 2000 *Phys. Rev. D* **62** 124011

[38] Font J A, Goodale T, Iyer S, Miller M, Rezzolla L, Seidel E, Stergioulas N, Suen W M and Tobias M 2002 *Phys. Rev. D* **65** 084024

[39] Yoneda G and Shinkai H 2002 *Phys. Rev. D* **66** 124003

[40] Kawamura M and Oohara K 2004 *Prog. Theor. Phys.* **111** 589–594

[41] Pollney D, Reisswig C, Rezzolla L, Szilágyi B, Ansorg M, Deris B, Diener P, Dorband E N, Koppitz M, Nagar A and Schnetter E 2007 *Phys. Rev. D* **76** 124002

[42] Alcubierre M, Brügmann B, Dramlitsch T, Font J A, Papadopoulos P, Seidel E, Stergioulas N and Takahashi R 2000 *Phys. Rev. D* **62** 044034

[43] Sarbach O, Calabrese G, Pullin J and Tiglio M 2002 *Phys. Rev. D* **66** 064002

[44] Bona C, Ledvinka T, Palenzuela C and Zacek M 2004 *Phys. Rev. D* **69** 064036

[45] Nagy G, Ortiz O E and Reula O A 2004 *Phys. Rev. D* **70** 044012

[46] Yo H J, Baumgarte T W and Shapiro S L 2002 *Phys. Rev. D* **66** 084026

[47] Alcubierre M, Brügmann B, Pollney D, Seidel E and Takahashi R 2001 *Phys. Rev. D* **64** 061501(R)

[48] Ansorg M, Fischer T, Kleinwächter A, Meinel R, Petroff D and Schöbel K 2004 *MNRAS*

[49] Meinel R Ansorg M K A N G and D P 2008 (Cambridge University Press)

[50] Bona C and Massó J 1992 *Phys. Rev. Lett.* **68** 1097

[51] Bona C, Massó J, Seidel E and Stela J 1995 *Phys. Rev. Lett.* **75** 600–603

[52] Alcubierre M 1997 *Phys. Rev. D* **55** 5981–5991

[53] Alcubierre M and Massó J 1998 *Phys. Rev. D* **57** R4511–R4515

[54] Anninos P, Camarda K, Massó J, Seidel E, Suen W M, Tobias M and Towns J 1996 *The Seventh Marcel Grossmann Meeting: On Recent Developments in Theoretical and Experimental General Relativity, Gravitation, and Relativistic Field Theories* ed Jantzen R T, Keiser G M and Ruffini R (Singapore: World Scientific) pp 644–647

[55] Misner C W, Thorne K S and Wheeler J A 1973 *Gravitation* (San Francisco: W. H. Freeman)

[56] Alcubierre M, Brügmann B, Diener P, Koppitz M, Pollney D, Seidel E and Takahashi R 2003 *Phys. Rev. D* **67** 084023

[57] Smarr L and York J W 1978 *Phys. Rev. D* **17** 2529–2552

[58] Löffler F, Rezzolla L and Ansorg M 2006 *Phys. Rev. D* **74** 104018

[59] Zenginoğlu A 2008 *Classical and Quantum Gravity* **25** 145002

[60] Gustafsson B and Kreiss H O 1979 *J. Comput. Phys.* **30** 333–351

[61] Rinne O 2005 *Axisymmetric Numerical Relativity* Ph.D. thesis University of Cambridge Cambridge, England

[62] Pretorius F 2005 *Class. Quantum Grav.* **22** 425–452

[63] Landau L D and Lifshitz E M 2004 *Fluid Mechanics, Course of Theoretical Physics, Volume 6* (Oxford: Elsevier Butterworth-Heinemann)

[64] Lax P D and Wendroff B 1960 *Commun. Pure Appl. Math.* **13** 217–237

[65] Hou T Y and LeFloch P G 1994 *Math. Comp.* **62** 497–530

[66] Martí J M, Ibáñez J M and Miralles J A 1991 *Phys. Rev. D* **43** 3794

[67] Banyuls F, Font J A, Ibáñez J M, Martí J M and Miralles J A 1997 *Astrophys. J.* **476** 221

[68] Leveque R J 1992 *Numerical Methods for Conservation Laws* (Basel: Birkhauser Verlag)

[69] Font J A 2003 *Living Rev. Relativ.* **6** 4

[70] Duez M D, Shapiro S L and Yo H J 2004 *Phys. Rev. D* **69** 104016

[71] Zink B, Stergioulas N, Hawke I, Ott C D, Schnetter E and Müller E 2006 *Phys. Rev. Lett.* **96** 161101

[72] Dumbser M, Enaux C and Toro E F 2008 *Journal of Computational Physics* **227** 3971–4001

[73] Gustafsson B, Kreiss H O and Oliger J 1995 *Time dependent problems and difference methods* (New York: Wiley)

[74] Toro E F 1999 *Riemann Solvers and Numerical Methods for Fluid Dynamics* (Springer-Verlag)

[75] Godunov S K 1959 *Mat. Sb.* **47** 271

[76] Laney C B 1998 *Computational Gasdynamics* (Cambridge University Press)

[77] Leveque R J 1998 *Computational Methods for Astrophysical Fluid Flow* ed O S and A G (Springer-Verlag)

[78] Martí J M and Müller E 1994 *J. Fluid Mech.* **258** 317–333

[79] Pons J A, Martí J M and Müller E 2000 *J. Fluid Mech.* **422** 125–139

[80] Martí J M and Müller E 1999 *Living Rev. Relativ.* **2** 3 URL `http://www.livingreviews.org/lrr-1999-3`

[81] Rezzolla L, Zanotti O and Pons J A 2003 *Journ. of Fluid Mech.* **479** 199

[82] Eulderink F and Mellema G 1994 *Astron. Astrophys.* **284** 652

[83] Donat R and Marquina A 1996 *J. Comput. Phys.* **125** 42

[84] Donat R, Font J A, Ibáñez J M and Marquina A 1998 *J. Comput. Phys.* **146** 58–81

[85] Roe P L 1981 *J. Comput. Phys.* **43** 357

[86] Harten A, Engquist B, Osher S and Chakrabarty S R 1987 *J. Comput. Phys.* **71** 231

[87] van Leer B J 1977 *J. Comput. Phys.* **23** 276

[88] van Leer B J 1979 *J. Comput. Phys.* **32** 101

[89] Colella P and Woodward P R 1984 *J. Comput. Phys.* **54** 174

[90] Font J A, Stergioulas N and Kokkotas K D 2000 *MNRAS* **313** 678

[91] Baiotti L, Hawke I, Montero P and Rezzolla L 2003 *Computational Astrophysics in Italy: Methods and Tools* vol 1 ed Capuzzo-Dolcetta R (Trieste: MSAIt) p 210

[92] Gottlieb S and Shu C 1998 *Math. Comp.* **67** 73–85

[93] Shu C W and Osher S J 1988 *J. Comput. Phys.* **77** 439

[94] Shibata M and Ury$\bar{\text{u}}$ K 2002 *Prog. Theor. Phys.* **107** 265

[95] Shibata M and Sekiguchi Y I 2003 *Phys. Rev. D* **68** 104020

[96] Shibata M, Sekiguchi Y and Takahashi R 2007 *Progress of Theoretical Physics* **118** 257–302

[97] Stergioulas N and Friedman J L 1995 *Astrophys. J.* **444** 306

[98] Harten A, Lax P D and van Leer B 1983 *SIAM Rev.* **25** 35

[99] Frauendiener J 2002 *Phys. Rev. D* **66** 104027

[100] Baiotti L, Hawke I, Montero P J, Löffler F, Rezzolla L, Stergioulas N, Font J A and Seidel E 2005 *Phys. Rev. D* **71** 024035

[101] Dimmelmeier H, Stergioulas N and Font J A 2006 *MNRAS* **368** 1609–1630

[102] Yoshida S and Eriguchi Y 2001 *MNRAS* **322** 389

[103] Martí J M, Müller E, Font J A, Ibáñez J M and Marquina A 1997 *Astrophys. J.* **479** 151

[104] Gundlach C 1999 *Living Reviews in Relativity* **2** 4 URL `www.livingreviews.org/Articles/Volume2/1999-4gundlach`

[105] Chandrasekhar S 1939 *An introduction to the study of stellar structure* (New Haven, USA: Dover Publications)

[106] Giacomazzo B and Rezzolla L 2007 *Class. Quantum Grav.* **24** S235

[107] Baiotti L, Giacomazzo B and Rezzolla L 2008 *Phys. Rev. D* **78** 084033

[108] Alcubierre M, Brandt S R, Brügmann B, Holz D, Seidel E, Takahashi R and Thornburg J 2001 *Int. J. Mod. Phys. D* **10** 273–289

[109] Chirenti C B M H and Rezzolla L 2007 *Classical and Quantum Gravity* **24** 4191–4206

[110] Anderson M, Hirschmann E W, Lehner L, Liebling S L, Motl P M, Neilsen D, Palenzuela C and Tohline J E 2008 *Phys. Rev. D* **77** 024006

[111] Gabler M, Sperhake U and Andersson N 2009 *Phys. Rev. D* **80** 064012

[112] Baiotti L, Giacomazzo B and Rezzolla L 2009 *Class. Quantum Grav.* **26** 114005

[113] Baiotti L and Rezzolla L 2006 *Phys. Rev. Lett.* **97** 141101

[114] Hawke I, Löffler F and Nerozzi A 2005 *Phys. Rev. D* **71** 104006

[115] Wald R M 1997 Gravitational collapse and cosmic censorship (*Preprint* `gr-qc/9710068v3`) URL `http://www.citebase.org/abstract?id=oai:arXiv.org:gr-qc/9710068`

[116] Flanagan E 1991 *Phys. Rev. D* **44** 2409–2420

[117] Senovilla J M M 2008 *Europhysics Letters* **81** 20004

[118] Schoen R and Yau S T 1983 *Communications in Mathematical Physics* **90** 575–579

[119] Plato 427-347 BC; *Book VII of The Republic*

[120] Gaarder J 1994 *Sophie's World* (Berkley Novel)

[121] Ibáñez J, Aloy M, Font J, Martí J, Miralles J and Pons J 2001 *Godunov methods: theory and applications* ed Toro E (New York: Kluwer Academic/Plenum Publishers)

[122] Thompson K W 1986 *Journal of Fluid Mechanics* **171** 365–375

Acknowledgment

First and foremost, I thank my wife, my children and my parents for their continuous love and support for carrying out this work.

I am grateful to Thomas Radke for his help and friendship. Much to my regret Thomas died in summer 2009.

I am deeply indebted to Luciano Rezzolla for giving me the chance to join the Numerical Relativity group of the Albert Einstein Institute (AEI) and enabling me to carry out my thesis. He is an excellent advisor and one of the most strict and systematic teachers I ever had.

Just as much, I thank Denis Pollney, who take me to the AEI, just as well to Christian David Ott, Luca Baiotti, Bruno Giacomazzo, Jonathon Thornburg, Anil Zenginoglu for the introduction to numerical relativity. They have been my collaborators, teachers and have been always open for scientific discussions.

Furthermore I express my one's gratitude for helpful and controversial discussion to all the other members and collaborators of the NumRel group: Daniela Alic, Marcus Ansorg, Alexander Beck-Ratzka, Nico Budewitz, Cecilia Chirenti, Harry Dimmeleier, Kyriaki Dionysopoulou, Nils Dorband, Filippo Galeazzi, Ian Hawk, Jörg Henning, Sascha Husa, Michael Jasiulek, Michael Koppitz, David Link, Frank Löffler, Philipp Mösta, Carlos Palenzuela, David Radice, Bernd Reimann, Oliver Rinne, Lucia Santamaria, Carsten Schneemann, Erik Schnetter, Bernhard Schutz, Jennifer Seiler, Béla Szilgyi, Kentaro Takami, Aaryn Tonita, Tilman Vogel, Steve White, Shin'ichirou Yoshida, Burkhard Zink.

It is a pleasure to thank Shin'ichirou Yoshida for providing us with the perturbative eigenfrequencies and Pedro Montero, Olindo Zanotti and Toni Font for useful discussions. The computations were performed on the clusters Peyote, Belladonna and Damiana of the AEI. This work was supported in part by the DFG grant SFB/Transregio 7 and by the JSPS Postdoctoral Fellowship For Foreign Researchers, Grant-in-Aid for Scientific Research (19-07803) an in part by the IMPRS on "Gravitational-Wave Astronomy".